EXPLORING NOVEL ELECTRONIC AND OPTOELECTRONIC DEVICES BASED ON LAYERED MATERIALS

A Dissertation
Presented to the Faculty of the Graduate School
of Cornell University
In Partial Fulfillment of the Requirements for the Degree of
Doctor of Philosophy

by
Rusen Yan
Jan 2017

EXPLORING NOVEL ELECTRONIC AND OPTOELECTRONIC DEVICES BASED ON LAYERED MATERIALS

Rusen Yan, Ph. D.
Cornell University 2017

The past decade has witnessed an enormous rise of two-dimensional layered materials (2DLMs) in the scientific community, including graphene, transition metal dichalcogenides (TMDs), hexagonal boron nitride (hBN), and black phosphorous (bP) etc. The nature of weak van der Waals (vdW) interactions between the atomically thin layers makes it possible to isolation them into few-layer or monolayer form without surface dangling bonds. Remarkable and unique properties appear at the atomically thin limit, and thus opening new opportunities to explore ultra-thin electronic and optoelectronic applications, such as quantum tunneling based devices, ultrafast photodetectors, broadband modulators, solar cells etc. The focuses of this work are developed along two streams: property characterizations of 2DLMs and their novel device explorations. On the characterization front, spectroscopic techniques are utilized for the first time to determine the band offsets of graphene on oxide structures and simultaneously extracting the work function of graphene; using Raman spectroscopy coupled with comprehensive thermal transport modeling, in-plane thermal conductivity in atomically thin TMD monolayers is characterized for the first time. On the device aspect, graphene based terahertz (THz) modulators are invented, promising superior

performance; various types of vdW heterojunctions (HJs) are built and tested. For example, vdW Esaki tunneling diodes are demonstrated for the first time, which are subsequently used to build a proof-of-concept radio frequency (RF) oscillator.

BIOGRAPHICAL SKETCH

Rusen Yan

Education

Ph. D., Electrical Engineering, Cornell University, Ithaca, NY	12/2016
M. S., Electrical Engineering, University of Notre Dame, Notre Dame, IN	12/2011
B. S., Electrical Engineering, Shandong University, Jinan, China	06/2010

Publications

[JX] **R. Yan**, Y. Yue, H. G. Xing, F. Ejeckam, B. Bolliger, "Superior thermal dissipation in GaN-on-Diamond transistors characterized by Raman spectroscopy," to be submitted.

[JX] **R. Yan**, S. Bertolazzi, J. Brivio, T. Fang, A. Konar, A. G. Birdwell, N. V Nguyen, A. Kis, D. Jena, and H. G. Xing, "Raman and photoluminescence study of dielectric and thermal effects on atomically thin MoS2," arXiv1211.4136, (2012).

[J22] **R. Yan**, S. Arezoomandan, B, Sensale-Rodriguez, and H. G. Xing, "Exceptional terahertz wave modulation in graphene enhanced by frequency selective surfaces," ACS Photonics 3 (3), 315 (2016).

[J21] **<u>R. Yan</u>**, S. Fathipour, Y. Han, B. Song, S. Xiao, M. Li, N. Ma, V. Protasenko, D. A. Muller, D. Jena, and H. G. Xing, "Esaki diodes in van der Waals heterojunctions with broken-gap energy band alignment," Nano Lett. 15 (9), 5791 (2015).

[J20] **<u>R. Yan</u>**, S. Bertolazzi, J. Brivio, M. Watson, X. Wu, A. Kis, T. Luo, A. R. Hight Walker, and H. G. Xing, "Thermal conductivity of monolayer molybdenum disulfide obtained from temperature-dependent Raman spectroscopy," ACS Nano, 8, 986 (2014).

(As of Sep/Oct 2016, this highly cited paper received enough citations to place it in the top 1% of its academic field based on a highly cited threshold for the field and publication year. - Data from Essential Science Indicators)

(Featured by physics.org)

[J19] **<u>R. Yan</u>**, L. Cai and X. Meng, "Correction of wave-front retrieval errors caused by the imperfect collimation of reference beam in phase-shifting interferometry," Opt. Int. J. Light Electron Opt., 125, 601 (2013).

[J18] **<u>R. Yan</u>**, Q. Zhang, O. A. Kirillov, W. Li, J. Basham, A. Boosalis, X. Liang, D. Jena, C. A. Richter, and A. C. Seabaugh, "Graphene as transparent electrode for direct observation of hole photoemission from silicon to oxide," Appl. Phys. Lett., 102 (12), 123106 (2013).

(Featured by Advances in Engineering)

[J17] **R. Yan**, B. Sensale-Rodriguez, L. Liu, D. Jena, and H. G. Xing, "A new class of electrically tunable metamaterial terahertz modulators.," Opt. Express, 20 (27), 28664 (2012).

[J16] **R. Yan**, Q. Zhang, W. Li, I. Calizo, T. Shen, C. A. Richter, A. R. Hight-Walker, X. Liang, A. Seabaugh, D. Jena, H. G. Xing, D. J. Gundlach, and N. V. Nguyen, "Determination of graphene work function and graphene-insulator-semiconductor band alignment by internal photoemission spectroscopy," Appl. Phys. Lett., 101 (2), 022105 (2012).

(Featured by IEEE Spectrum)

[J15] H. G. Xing, **R. Yan**, B. Song, J. Encomendero, and D. Jena, "THz devices based on 2D electron systems," SPIE Defense+ Security,, p. 94760 (2015).

[J14] S. Fathipour, M. Remskar, A. Varlec, A. Ajoy, **R. Yan**, S. Vishwanath, S. Rouvimov, W. S. Hwang, H. G. Xing, D. Jena, and A. Seabaugh "Synthesized multiwall MoS2 nanotube and nanoribbon field-effect transistors," Appl. Phys. Lett., 106, 022114 (2015).

[J13] H. Shi, **R. Yan**, S. Bertolazzi, J. Brivio, B. Gao, A. Kis, and D. Jena, H. G. Xing and L. Huang, "Exciton Dynamics in Suspended Monolayer and Few-Layer MoS2 2D Crystals," ACS Nano, 7, 1072 (2013).

[J12] B. Sensale-Rodriguez, S. Rafique, **R. Yan**, M. Zhu, V. Protasenko, D. Jena, L. Liu, and H. G. Xing, "Terahertz imaging employing graphene modulator arrays," Opt. Express, 21 (2), 2324 (2013).

[J11] B. Sensale-Rodriguez, **R. Yan**, L. Liu, D. Jena, and H. G. Xing, "Graphene for Reconfigurable Terahertz Optoelectronics," Proc. IEEE, 101 (7), 1705 (2013).

[J10] W. S. Hwang, M. Remskar, **R. Yan**, T. Kosel, J. Kyung Park, B. Jin Cho, W. Haensch, H. G. Xing, A. Seabaugh, and D. Jena, "Comparative study of chemically synthesized and exfoliated multilayer MoS2 field-effect transistors," Appl. Phys. Lett., 102 (4) (2013).

[J9] K. Xu, Q. Zhang, **R. Yan**, P. Ye, K. Wang, A. C. Seabaugh, H. G. Xing, J. S. Suehle, C. A. Richter, D. J. Gundlach, and N. V Nguyen, "Direct measurement of Dirac point energy at the graphene/oxide interface," Nano Lett., 13 (1), 131 (2013).

[J8] Q. Zhang, R. Li, **R. Yan**, T. Kosel, H. G. Xing, A. C. Seabaugh, K. Xu, O. A. Kirillov, D. J. Gundlach, C. A. Richter and N. V. Nguyen "A unique photoemission method to measure semiconductor heterojunction band offsets," Appl. Phys. Lett., 102 (1), 12101 (2013).

[J7] B. Sensale-Rodriguez, **R. Yan**, M. M. Kelly, T. Fang, K. Tahy, W. S. Hwang, D. Jena, L. Liu, and H. G. Xing, "Broadband graphene terahertz modulators enabled by intraband transitions," Nat. Commun. 3, 780 (2012).

[J6] B. Sensale-Rodriguez, **R. Yan**, S. Rafique, M. Zhu, W. Li, X. Liang, D. Gundlach, V. Protasenko, M. M. Kelly, D. Jena, L. Liu, and H. G. Xing, "Extraordinary control of terahertz beam reflectance in graphene electro-absorption modulators," Nano Lett., 12 (9), 4518 (2012).

[J5] B. Sensale-Rodriguez, **R. Yan**, M. Zhu, D. Jena, L. Liu, and H. G. Xing, "Efficient terahertz electro-absorption modulation employing graphene plasmonic structures," Appl. Phys. Lett., 101 (26), 261115 (2012).

[J4] W. S. Hwang, M. Remskar, **R. Yan**, V. Protasenko, K. Tahy, S. Doo Chae, P. Zhao, A. Konar, H. G. Xing, A. Seabaugh, and D. Jena, "Transistors with chemically synthesized layered semiconductor WS_2 exhibiting 10^5 room temperature modulation and ambipolar behavior," Appl. Phys. Lett., 101 (1), 013107 (2012).

[J3] B. Sensale-Rodriguez, T. Fang, **R. Yan**, M. M. Kelly, D. Jena, L. Liu, and H. G. Xing, "Unique prospects for graphene-based terahertz modulators," Appl. Phys. Lett., 99 (11), 113104 (2011).

[J2] L. Cai and **R. Yan**, "Analysis and simulation study of the apparent images of underwater objects," College Physics, 30 (8), 1 (2011).

[J1] X. F. Xu, L. Z. Cai, Y. R. Wang, and **R. Yan**, "Direct phase shift extraction and wavefront reconstruction in two-step generalized phase-shifting interferometry," J. Opt., 12, 15301 (2010).

Dedications to my parents,

and Lin.

ACKNOWLEDGEMENT

I am delighted to express my thanks to everyone who helped me through the past six and half years along my PhD life.

First, I would like to thank my adviser, Grace, who gave me the opportunity to learn and grow in such a friendly, inspiring and creative group. I am greatly impressed by her intelligence, patience, and kindness. What Grace taught me is much more than doing research, also involves how to be a more mature person. She is always there to give me a hand whenever I encounter difficult moments both in and out of the labs. I am beyond my words in gratitude to her.

I want to thank DJ, whose wide spectrum of knowledge and deep understanding of fundamental problems often inspired me to think differently than I originally did. He always has plenty of novel and brave ideas in mind to share, which makes research experience so interesting and joyful.

I would like to thank Prof. Rana for his time spent with me on reviewing my thoughts and explanations to various experimental observations. His insightful suggestions on how to tackle problems often impress me and lead me to find the truth. I am fortunate to have him on my committee to make my studies more comprehensive and rigorous.

Many thanks also go to our senior group members at Notre Dame: Tian Fang, Berardi, Guowang, Ronghua, Guangle, Zongyang, Jia for their help on getting me started in an entirely new place and in the lab. Wan Sik and Kristof taught me how to make a transistor. Vlad helped me and taught me build optical set-up to measure a lot of the data shown in this thesis. Berardi proofread my manuscripts, and gave me lots of suggestions about life and career. Michelle provided me graphene to make devices.

I would like to mention many of our group members and lab-mates: Bo Song, Xiaodong Yan, Mingda Li, Shudong Xiao, Kazuki Nomoto, Wenshen Li, Brian Schutter, Alex Chaney, Amit Verma, Jimy Encomendero, Tongbo Wei, Suresh Vishwanath, Moududul Islam, Mingda Zhu, who helped me in all kinds of aspects.

I appreciate Prof. Alan Seabaugh, Dr. David Gundlach, Dr. Nhan Nguyen, Dr. Curt Richter, and Dr. Qin Zhang for providing me an opportunity to work at NIST for productive eight months. I would never forget the enjoyable times spent at Gaithersburg.

Finally, I hope to say thanks to my parents, my grandparents, and Lin for their unconditional trust and encouragement. None of the work would be possible without their support.

TABLE OF CONTENTS

LIST OF FIGURES

LIST OF TABLES

CHAPTER 1: INTRODUCTION

1.1 Two-dimensional layered materials

The awarding of Nobel Prize in 2010 acquaints the world with graphene. As a single sheet of carbon atoms arranged in hexagonal structure, graphene possesses unique physical properties that are hardly seen in traditional semiconductors, which arouses tremendous interests in both scientists and engineers [1-4]. Different from particles following non-relativistic Schrödinger equation, graphene exhibits transport characteristics of 2-dimensional (2D) Dirac fermions with zero effective mass and a Fermi speed of 10^6 m/s. With remarkably high carrier mobility, graphene has been shown potential for high-speed electronics and optoelectronics. The highest mobility reported to date is 200,000 cm^2/Vs for suspended graphene [5] and 150,000 for BN-supported one, both at carrier density of $\sim 2\times 10^{11} cm^{-2}$ [6]. Its pronounced response to the external electric field effect and facile integration process make graphene suitable to form the voltage-tunable resistors. Compared to 3D materials-based devices with dangling bond at surfaces, the in-plane sp^2 bond of graphene with out-of-plane van der Waals (vdW) interaction helps to reduce interface trap states, which further improves the device performance [1]. Beyond these, graphene also shows excellent optical properties. The linear dispersion of the Dirac electrons in graphene renders broadband absorption by graphene, which can be expressed by the fine-structure constant. In spite of being only one-atom layer thin, it can be optically visualized on substrates thanks to its 2.3% absorption of the visible light [7, 8]. Consequently, graphene is believed to hold promises for both electronic and optoelectronic applications in the future.

The successful exfoliation of graphene is just the beginning. Explorations on other two-dimensional layered materials (2DLMs) beyond graphene, such as metal chalcogenides [9], hexagonal boron nitride (hBN) [10], black phosphorus (bP) [11] etc. are emerging fast as new stars. One of their most distinguishing and fascinating properties is layer-dependent physical behavior. For example, 2DLMs often exhibit an indirect to direct band gap transition when they are thinned down from bulk to monolayer form. Much more favorable than graphene, the sizable band gap offers new possibilities for applications in both electronics and optoelectronics. Among them, MoS_2 is one most heavily investigated example 2DLM. Field effect transistors with monolayer MoS_2 as channel material showing a high on/off ratio of ~$1x10^8$ have been demonstrated by Kis group [12]. The direct band gap at monolayer form results in prominent photoluminescence (PL) in MoS_2 [13, 14], WS_2 [15] etc., which paves way for various optoelectronic applications. The quantum yield (QL) observed on few-layer MoS_2 so far is 10^{-5} to 10^{-6} and up to $4x10^{-3}$ for monolayer one [16]. However, QL observed on suspended samples is significantly larger than the ones supported on SiO_2, which indicates strong substrate effects on the properties of 2DLMs. The optical absorption spectrum of MoS_2 shows two main features, respectively corresponding to A and B exciton related band transitions at K point of the Brillouin zone [13, 17]. Due to the large effective mass and low dielectric screening, an exciton binding energy as large as few hundred meV are predicted and measured in some layered chalcogenides [18].

1.2 Van der Waals heterojunctions

The out-of-plane vdW bonding of layered materials make it possible to stack them together into a new type of vdW heterojunctions (HJs), which do not suffer from lattice mismatch as in conventional HJs, thus creating a huge design freedom of junctions and superlattices [19-21]. Previous studies over the past few years on this subject have demonstrated and predicted numerous intriguing physics phenomena and device applications with carefully designed material sequences. For example, the graphene/hBN HJ enables observation of Moiré superlattices, Hofstadter butterfly spectrum, and tunable phonon polaritons, thanks to the periodic potential modulation between graphene and hBN [22-24]. As mentioned above, excitons play an essential role in optical properties of vdW materials because of their large binding energy. Interestingly, not only can these strongly bound electron-hole pairs live in single material, but also can exist while bound electrons and holes spatially separated from each other in different layers [25]. Additionally, ultrafast (<50 fs) charge carrier transfer process was observed across vdW interface (MoS_2/WS_2) [26], indicating their potential of making energy- efficient tunneling electronic and fast optoelectronic devices. This phenomenon is not surprising in that charge carriers in each layer only need to move a few angstroms vertically from one to another to find lower energy states, which would be difficult in conventional bonded heterojunctions where a relatively large depletion region is typically present. Owing to such unique interface features, vdW HJs are believed to be advantageous in a variety of device platforms. Efficient, ultrathin photodetectors with external quantum efficiency of more than 30% are realized using a graphene/WS_2/graphene stack [27]. Multi-stacked graphene/hBN/WSe_2/hBN/graphene quantum wells emits light in an efficiency of 8% [28].

1.3 This work

In this work, I primarily focused on investigation of the electronic, optoelectronic and thermal properties of some typical 2DLMs, and how to utilize them for novel device applications.

In Chapter 1, internal photoemission spectroscopy (IPE) technique is employed to determine the band alignment of two graphene-oxide-silicon (GOS) structures with SiO_2 and Al_2O_3 as the oxide layer, respectively. Such studies are demanded for design of electronic and optoelectronic devices operating on an oxide-silicon substrate. Along with band alignment, we can also accurately extract the work function of graphene to be 4.6 eV. With unique combination of high optical transparency and exceptional electrical conductivity, we found that graphene, replacing conventional metal electrode, can improve the IPE technique. With small absorption and low density of states (DOS) of graphene, much less photo-carriers are generated in graphene compared to that in Si. By applying an electric filed over the oxide, excited photo-carriers, either holes of electrons in Si (or another material) dependent on the direction of the electric field, can transport to the graphene electrode forming detectable photocurrents. In this way, both conduction and valence band offsets could be determined simultaneously, which is a breakthrough in IPE studies.

In Chapter 3, a graphene-based near-field enhanced THz modulator is theoretically proposed and a proto-type design is experimentally demonstrated. Limited by the small conductivity swing of state-of-art CVD-grown graphene and relatively weak light-interaction between graphene and THz electromagnetic waves, performance of previously demonstrated graphene THz modulators with a structure of graphene/SiO_2/Si structure cannot meet the requirements for practical applications [29]. To tackle this issue, we proposed the idea of placing metamaterial (MM), specifically frequency selective surface (FSS) in front of graphene to enhance its interaction with THz waves [30, 31]. With this strategy, high modulation depth (MD), low insertion loss (IL) and high speed operation of graphene-based THz modulators can be simultaneously achieved. Both simulation and experimental results will be shown.

In Chapter 4, dielectric and thermal effects on Raman spectroscopy of MoS_2 are discussed. High-K dielectric can boost the electrical mobility of MoS_2 [26] but also affect the phonon vibrations in thin layer of TMDs drastically [32]. Such findings also suggest that the properties of thin films can be monitored using non-contact Raman spectroscopy, as has been heavily investigated in graphene. We found strong thermal effects on Raman spectrum of MoS_2, which means the frequencies of phonon vibration peaks are sensitive to the incident laser power. Beyond that, we further determine the thermal conductivity of monolayer MoS_2 for the first time by combining the laser power and temperature dependent Raman spectra. Thus in this aspect, our study provides critical inputs to the thermal management of future MoS_2-based electronic and optoelectronic applications.

In Chapter 5, we turn to developing vdW heterojunctions utilizing the unique vdW bonding nature in these layered materials. The interlayer charge transfer process is probed by photocurrent spectroscopy for the first time and specific features of spectra under various bias and doping conditions unravel how such atomically thin vdW junctions are different from conventional ones. Beyond that, we built a broken-gap alignment structure composed of layered $SnSe_2$/bP and observed robust negative differential resistance (NDR) or conductance (NDC) behavior over a vdW tunneling barrier [33]. The appearance of NDR/NDC is a conclusive evidence of interlayer and interband tunneling, which sets valuable foundation for constructing vdW interlayer tunneling transistors: Thin-TFET, a device our group has proposed in 2013 and is actively pursuing.

CHAPTER 2: GRAPHENE AS TRANSPARENT ELECTRODE IN INTERNAL PHOTOEMISSION SPECTROSCOPY STUDY

2.1 Principle of internal photoemission spectroscopy

As a straightforward yet robust technique to characterize the properties of insulator/semiconductor and metal/insulator interfaces, internal photoemission spectroscopy has been developed and widely used for decades [34]. In this part, we will briefly introduce the principles of IPE technique and its applications in high-K based metal-oxide-semiconductor (MOS) structures in the past few years.

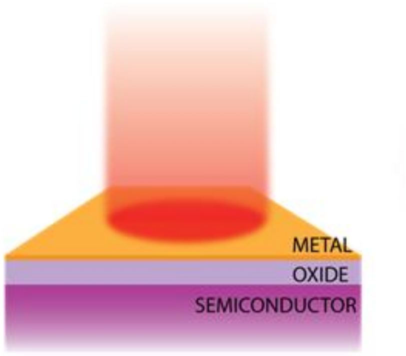

Figure 2.1 Conventional MOS structure used in IPE measurement.

The typical MOS IPE test structure is shown in Figure 2.1, where a gate voltage is applied between metal collector (usually, a thickness of 15 nm Au or Al is typically used) and the substrate semiconductor. Photons with different energies incident from the top can penetrate through the metal layer into the semiconductor below. Therefore, photo-carriers are simultaneously generated in both the metal electrode and the semiconductor.

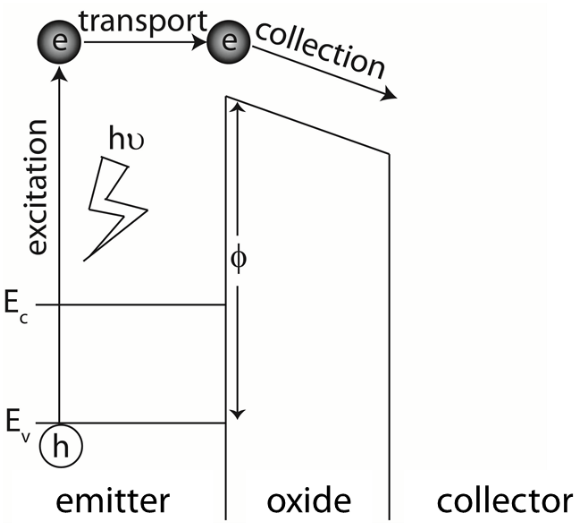

Figure 2.2 Schematic description of IPE process.

Figure 2.2 schematically depicts the IPE process, which could be generally divided into three steps: 1) excitation of photo-carriers in emitter; 2) transport (diffusion) of photo-carriers to the interface of oxide/emitter; 3) collection of carriers over the oxide to form detectable photocurrents. When the incident photon energies are large enough to excite electrons (holes) to the conduction (valence) band of oxide, these photo-excited carriers can transit over the oxide layer from one side (emitter) to the other side (collector). Consequently, photocurrents can be measured over the oxide as a function of incident photon energies. By normalizing measured photocurrents by the incident light flux, quantum yield (Y) is obtained, which could be written as [35]

$$Y(h\nu) = \begin{cases} A(h\nu - \phi)^p & h\nu \geq \phi \\ 0 & h\nu < \phi \end{cases} \qquad 2.1$$

where p depends on the energy distribution characteristics of the carriers, $h\nu$ is incident photon energy A is a constant and ϕ is the energy barrier height at the emitter/oxide interface (Figure 2.2) which is the minimum energy that carriers must acquire for photons to transport over oxide. It is found that $p = 2$ for metal/oxide and $p = 3$ for semiconductor/oxide interface [36]. Therefore, the threshold energy ϕ can be experimentally determined by linear extrapolation of the measured $Y^{1/2}$ or $Y^{1/3}$ to zero yield. This approach is widely employed in the present IPE technique and works well for most MOS structures.

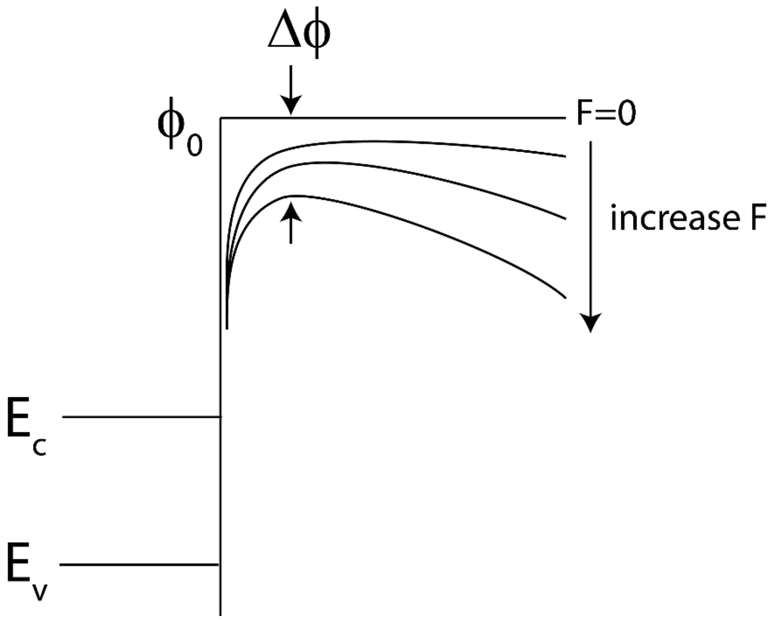

Figure 2.3 Schematic of image force effect lowering the barrier height by Δ.

The electric field (F) applied over the oxide can also influence the barrier height at the interface. The carriers injected into oxide experience a Coulomb interaction with the charge of polarized emitter, which leads to a lowering of the barrier height by $q(qF/4\pi\epsilon_0\epsilon_r)^{1/2}$ where q is electron charge, ϵ_0 is vacuum permittivity, and ϵ_r is oxide relative permittivity [37]. Therefore, the resulting barrier height as a function electric field is described as

$$\phi(F) = \phi_0 - \left(\frac{qF}{4\pi\epsilon_0\epsilon_r}\right)^{\frac{1}{2}} \qquad 2.2$$

This lowering effect is illustrated in Figure 2.3 where it could be seen that, as electric field increases, the barrier heights photo-carriers encounter are lower. By linear extrapolating $\phi(F)\ vs\ F^{1/2}$ to zero field, ϕ_0, barrier height at zero electric field can be extracted. This is the main mechanism and model used in our study to determine the barrier height at the material interface.

2.2 Band alignment of graphene-oxide-silicon structures

Accurate band offsets are critical for the design of device. In the community of graphene research, one of most widely used device structure is graphene on oxide covered Si substrate (degenerately doped). In this part, we will present band alignment analysis of graphene-oxide-silicon (GOS) structure respectively with SiO_2 and Al_2O_3 as oxide layer.

2.2.1 IPE setup

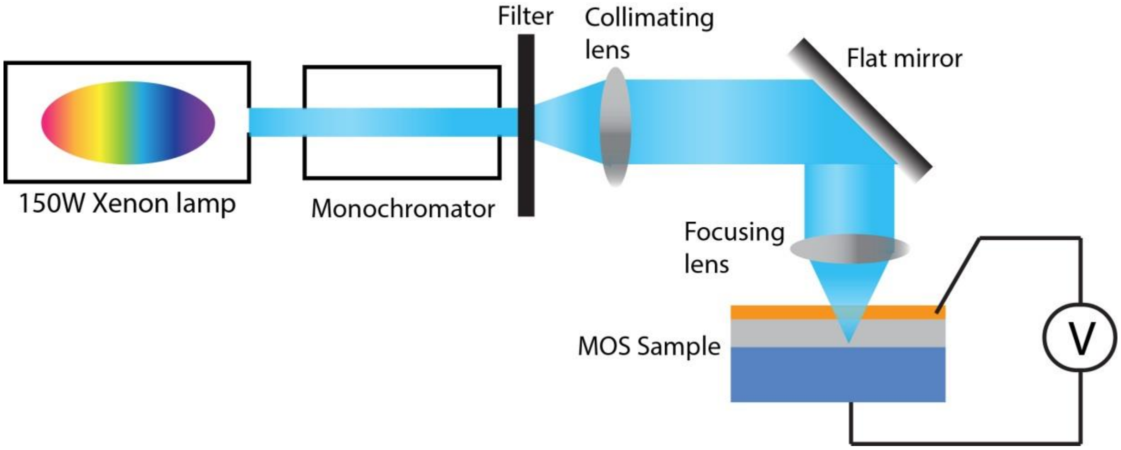

Figure 2.4 Illustration of IPE measurement system

The IPE measurement system used in this study, as shown in Figure 2.4, mainly consists of a 150 W broadband xenon light source and a quarter-meter Czerny Turner, f/4, 1200 line/mm ruled monochromator to provide a spectral range from 1.5 to 5.5 eV. Light out from the monochromator is collimated and then focused down to a beam spot in millimeter size by UV enhanced lenses. A voltage (V_{gs}) is applied between the top contact and the substrate with top metal contact grounded, and the photocurrent (I_{ph}) flowing across the MOS structure is recorded by an electrometer as light is scanned at different photon energies ($h\nu$). The light flux (P) is recorded by a Si diode at the focal point of second lens.

2.2.2 Band alignment of graphene-SiO_2-Si structure

Researchers have proposed a variety of promising applications using graphene. The performances of these device architectures are critically dependent on how the graphene-oxide-graphene (or semiconductor) (GOG or GOS) electronic bands align with each other. Specifically, under various gate voltages, their proper operations are a strong function of the relative position of Fermi levels on top and bottom conductive layers. Here we investigate the interfacial electronic properties of a graphene-SiO_2-Si stack using IPE.

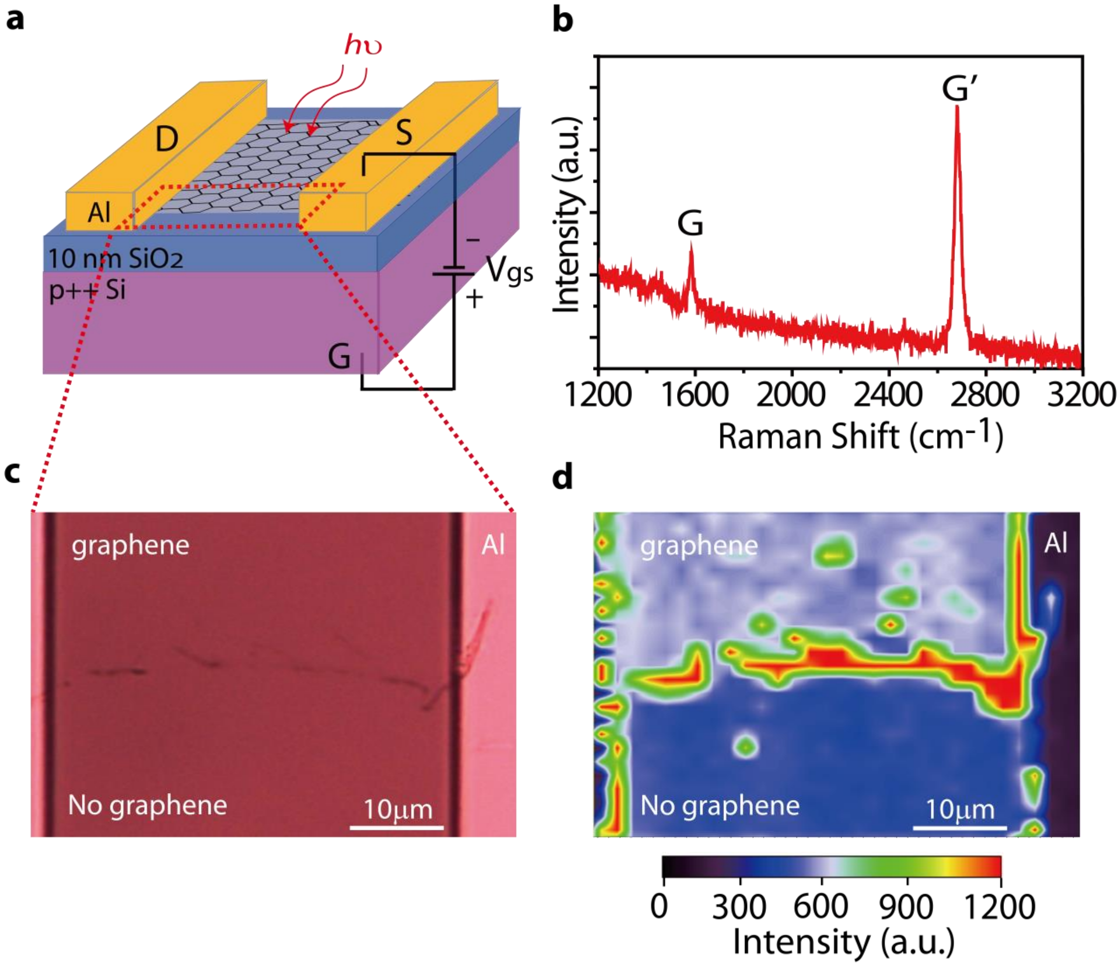

Figure 2.5 (a) Device structure. A gate voltage V_{gs} is applied between graphene and a p++ Si substrate with the Al top contact grounded. (b) Representative Raman spectrum collected on our device. The ratio of the G and G' peaks confirm that it is monolayer graphene. (c) and (d) Optical and corresponding Raman mapping image of the G peak intensity near the edge of the device. The contrast in (d) identifies the region with and without graphene which is invisible in the optical image.

The sample structure and the measurement configuration are schematically shown in Figure 2.5 (a). A large-area monolayer graphene film grown by CVD was transferred to a degenerately doped p-type Si substrate with a 10 nm-thick thermal SiO_2 layer [38]. To circumvent photoemission from the metal into graphene, a thick layer of 180 nm evaporated Al is used. The graphene channel is patterned using oxygen plasma etching. A representative Raman spectra (λ=514 nm) of the graphene in our device is shown in Figure 2.5 (b), which confirms it is monolayer graphene [39]. Considering the fact that 10 nm SiO_2 does not allow distinctive visibility of the graphene flake [40], we also show a spatial map of Raman G peak intensity at the edge of our device in Figure 2.5 (d) with its optical image shown in Figure 2.5 (c). I_{ph} flowing between graphene and Si is recorded as a function of incident photon energies.

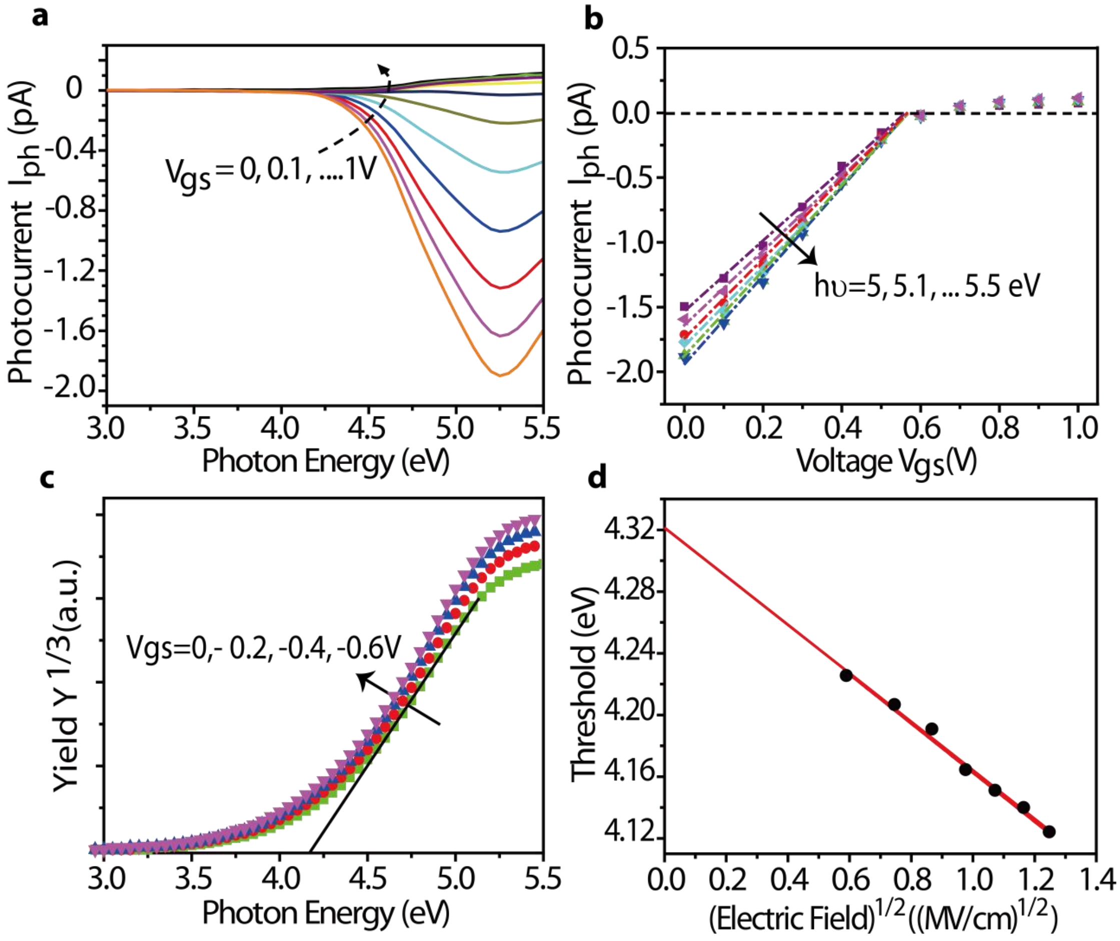

Figure 2.6 (a) Photocurrent as a function of incident photon energy and gate bias. (b) Photocurrent as a function of gate voltage. (c) Cubic root of yield $Y^{1/3}$ for negative current under gate voltages. (d) Schottky plot of negative current (electron injection). The barrier height linearly relates to $E^{1/2}$.

Figure 2.6 (a) shows I_{ph} vs photo energy ($h\nu$) as gate voltage V_{gs} varies from 0V to 1 V in step of 0.1 V with graphene grounded. It can be seen that the photocurrent switches from negative to positive at a certain gate voltage, defined as the flatband voltage (V_{fb}), at which the electric field in the thin oxide and thus current both reach zero. To determine V_{fb} accurately, in Figure 2.6 (b), we have plotted I_{ph} vs V_{gs} for photon energy larger than 5 eV and their linear fits yield V_{fb} = (0.56 ± 0.05) V at I_{ph} =0. As will be shown in Section 2.3, the negative and positive currents are in fact primarily the electron and hole injection from Si into graphene, respectively. Under illumination from the top of the device, electron-hole pairs are generated at the Si/SiO$_2$ interface. When $V_{gs} < V_{fb}$, electrons are photo-stimulated from the Si valence band to energy levels higher than the bottom of the oxide conduction band and driven by the electric field across the oxide into the graphene, thus producing the negative current. On the other hand, when $V_{gs} > V_{fb}$, the reversed electric field in the thin oxide drives photo-stimulated holes to the SiO$_2$ valence band into the graphene, which contributes to the positive current. Because the optical absorption in graphene is known to be relatively small (even it is already a large number for one-atomic thick graphene) [7], photo-excitation from the graphene Fermi level to the SiO$_2$ conduction band is assumed to be negligible, thus the positive current is attributed to hole emission from Si. In the following, both electron and hole barrier heights on Si side will be determined.

The quantum yield Y is then obtained by dividing photocurrents with incident light power calibrated by Si diode. According to Eq. 2.1, we can obtain the spectral threshold through the linear extrapolation to zero yield of the $Y^{1/3}$ vs $h\nu$ characteristics as shown in Figure 2.6 (c). Due to the image force effect, the barrier heights extracted show a linear relation to the square root of electric field in the oxide as exhibited in the Schottky plot in Figure 2.6 (d). The linear extrapolation to zero electric field gives a zero-field barrier height ϕ_0^e of 4.3 eV. Similar barrier height determination is performed for positive photocurrent as well, i.e., hole injection. As a result, the corresponding barrier height ϕ_0^h from the bottom of Si conduction band to the top of SiO$_2$ valence band is extracted to be 4.6 eV. With these values, we can estimate the bandgap of thin SiO$_2$

to be approximately 7.9 eV, following $E_g^{SiO_2} = \phi_0^e + \phi_0^h - E_g^{Si}$, where ϕ_0^e and ϕ_0^h are barrier heights encountered by electrons and holes, respectively. This result is in close agreement with the value extracted from ellipsometric data taken on the same sample, from which the Tauc plot [41] yields $E_g^{SiO_2}$=8.0 eV.

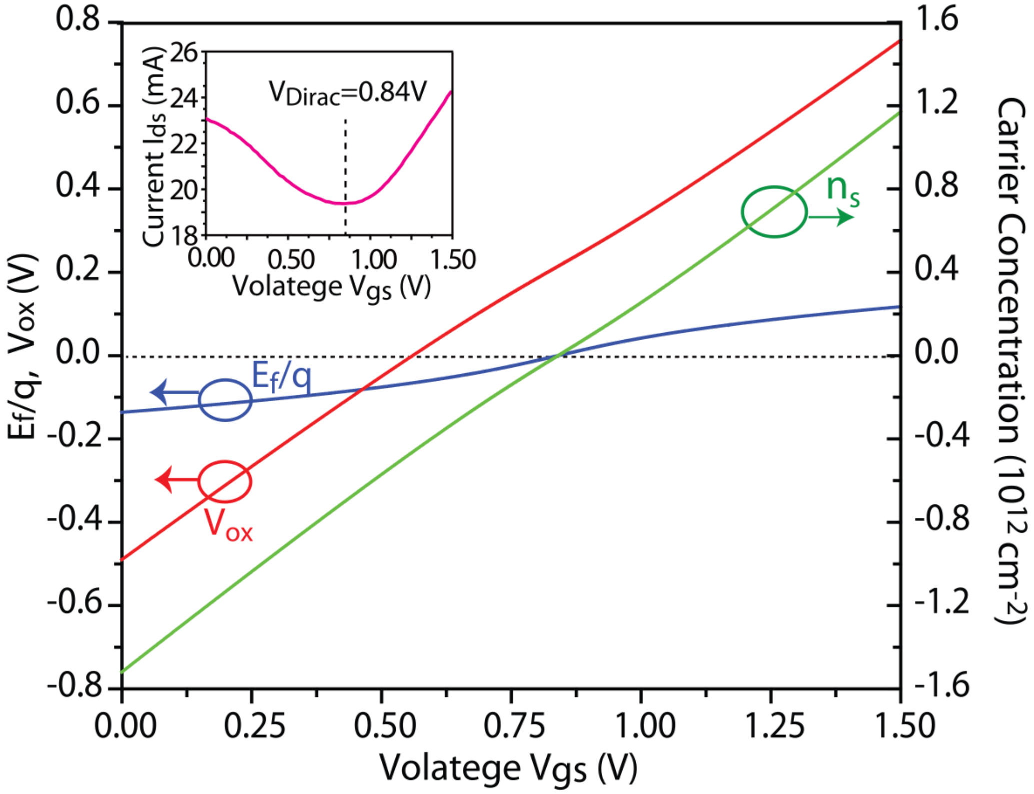

Figure 2.7 Calculated voltage drop across the oxide (red) and the difference between graphene Fermi level and its Dirac point (blue) as a function of gate voltage. The carrier concentration in graphene (green) where negative and positive values, respectively, relates to hole and electron as majority carriers. The inset shows the $I_d - V_{gs}$ characteristic of the device. Minimum conductivity is reached at V_{gs} =0.84 V.

To correlate the IPE results with electric charges on the graphene side, we also performed $I_d - V_{gs}$ measurements on the same device. The $I_d - V_{gs}$ characteristic shown in the inset of Figure 2.7 suggest a Dirac voltage (V_{Dirac}) of 0.84 V, which differs from V_{fb} measured by IPE by (0.28±0.05) V. This discrepancy provides direct evidence of the existence of extrinsic charges (n_{ex}, charge density per unit area) on the graphene side of the device. As being one-atom thick, graphene is sensitive to the external conditions. Under the flatband condition ($V_{gs} = V_{fb}$), there is no electric field inside the oxide, which means, n_t, the total charge density per unit area on the graphene side, and n_s, the total mobile charge concentration in graphene, have to satisfy the condition $n_t = n_s + n_{ex} = 0$, that is, $n_{ex} = - n_s$. Therefore, with the difference between V_{Dirac} from V_{fb}, we can estimate n_{ex} by examining n_s. It is assumed that n_{ex} is independent of the graphene Fermi level (E_f). The application of a gate voltage leads to the variation of carrier concentration and thus the shift of Fermi level in graphene, which can be characterized by the following relation [42]

$$V_{gs} - V_{Dirac} = \frac{E_f}{q} + \frac{n_s q}{C_{ox}} \qquad 2.3$$

where E_f is the Fermi level in graphene, $C_{ox} = \epsilon/d = 0.345\ \mu F/cm^2$, is the gate oxide capacitance per unit area. In Eq. 2.3, the carrier concentration is given by [38]

$$\begin{aligned} n_s &= n_0 - p_0 \\ &= \frac{2}{\pi}\left(\frac{k_B T}{\hbar|v_f|}\right)^2 \mathcal{F}_1(+\eta) - \frac{2}{\pi}\left(\frac{k_B T}{\hbar|v_f|}\right)^2 \mathcal{F}_1(-\eta) \end{aligned} \qquad 2.4$$

where $\mathcal{F}_j(\eta)$ is Fermi-Dirac integral with j=1 and $\eta = E_f/k_B T$, k_B is Boltzmann constant, T= 300 K is the absolute temperature, $\hbar$ is Planck's constant divided by 2π, and $v_f = 10^6$ m/s is the Fermi velocity. Note that $n_s > 0$ and $n_s < 0$ correspond to the cases of electron and hole as the majority carrier in graphene, respectively. Here, we choose to use the temperature dependent formula instead of the 0 K approximation that is widely adopted in the literature since 0 K approximation introduces an error of 25% at E_f = 0.08 eV in terms of n_s, only with an acceptable error less than 5% when E_f > 0.2 eV. Using Eqs. 2.3 and 2., in Figure 2.7, we plot E_f vs q (blue), n_s (green), and the net voltage over the oxide V_{ox} (red). It can be seen that at $V_{gs} = V_{fb} = (0.56 \pm 0.05)$ V, the Fermi level E_f in graphene is about (0.08 ± 0.01) eV below its Dirac point, which corresponds to the hole concentration $n_s = (4.6 \pm 0.8) \times 10^{11}$ cm^{-2}. To maintain the flatband condition, there must be the same amount of negative charges externally induced by the environment to compensate these holes. Therefore, we could obtain $n_{ex} = |n_s| = (4.6 \pm 0.8) \times 10^{11}$ cm^{-2}.

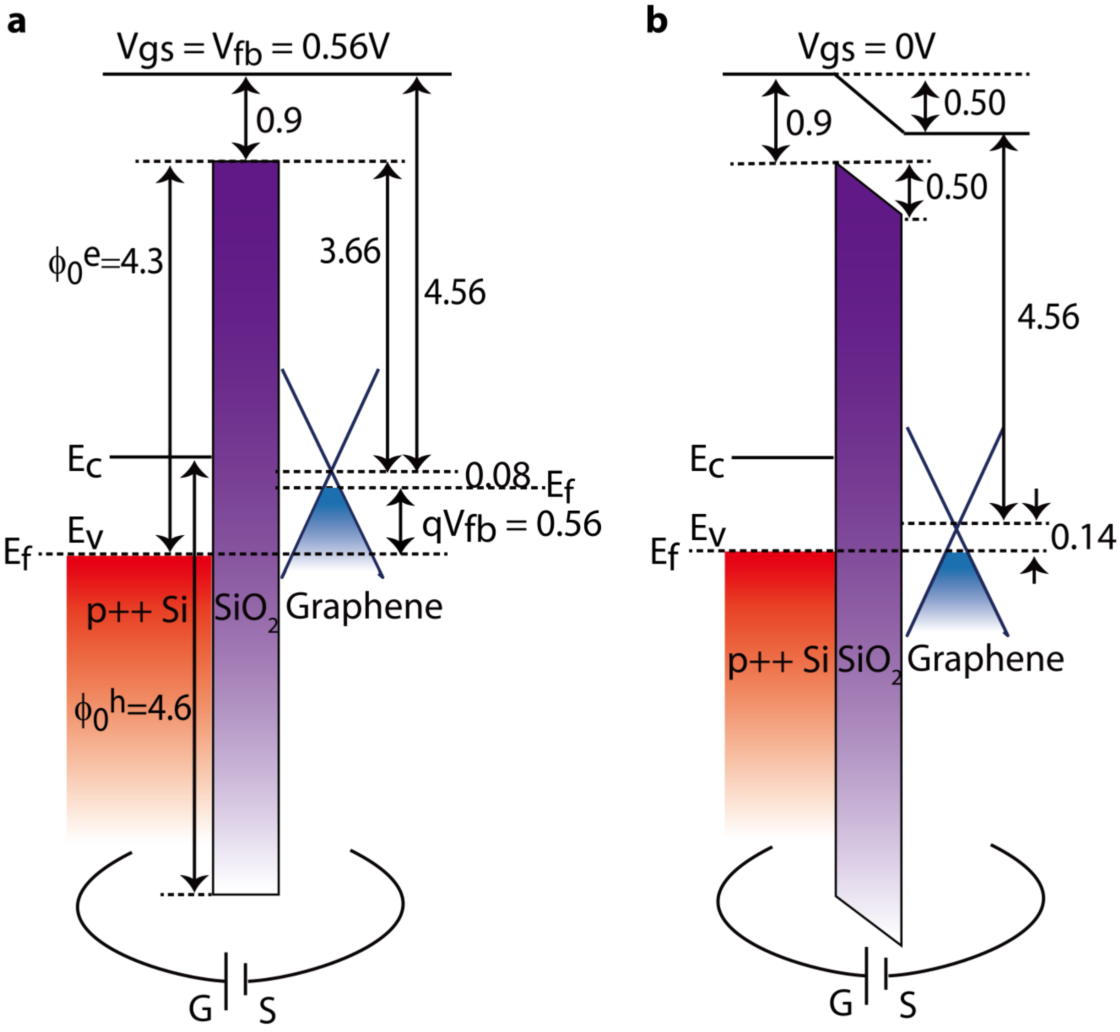

Figure 2.8 Band diagrams when (a) $V_{gs} = V_{fb}$ and (b) V_{gs}=0 V.
All the numbers labeled in the figure are in units of eV.

Most strikingly, the measurement of all these quantities, ϕ_0^e, V_{fb}, and V_{Dirac} allows us to accurately depict the band alignment in this graphene-SiO$_2$-Si structure. In Figure 2.8 (a) and (b), we show the band diagram when $V_{gs} = V_{fb}$ and V_{gs}=0 V, respectively, where ϕ_0^e = 4.3 eV is the barrier height from the top of Si valence band to the bottom of SiO$_2$ conduction band; $qV_{gs} = qV_f = (0.56 \pm 0.05)$ eV is the Fermi level difference between graphene and p^{++} Si under the flatband condition; $E_f = (0.08 \pm$

$0.01)$ eV is how far the Fermi level in graphene departs from its Dirac point. The height from the graphene Dirac point to the conduction band bottom of SiO_2 is calculated to be (3.66 ± 0.04) eV. By employing the well-known 0.9 eV electron affinity of SiO_2 [43], the work function of intrinsic graphene is extracted to be (4.56 ± 0.04) eV, in excellent agreement with values reported previously [44, 45].

2.2.3 Band alignment of graphene-Al_2O_3-Si structure

We also conduct the similar IPE measurements on a graphene-Al_2O_3-Si structure to demonstrate that graphene could be used as transparent electrode to enable the observation of hole transitions. In most of previous IPE experiments, a thin metal layer (10-15 nm) is used as an optically semitransparent contact to collect electrons or holes injected from the semiconductor emitter over the energy interfacial barrier formed between the emitter and the insulator. However, a long-standing issue with such a structure is that, the photocurrent due to hole injection is usually obscured by the unavoidably large electron current from the thin metal contact (collector) over the insulator [46]. Further complicating the experimental observation of hole injection from the semiconductor emitter is the rather limited range over which metal work function can be varied; for most semiconductor systems of interest, the barrier height for holes at the semiconductor-insulator interface is usually higher than the barrier height for electrons at the metal/insulator interface. Consequently, it is difficult to separate the contribution of hole emission and its barrier threshold from the total measured photocurrent [34, 36, 41, 46]. Additionally, semitransparent metals of a practical thickness used in IPE studies have substantial light absorption, particularly in the ultraviolet range that is important in IPE measurements, thus resulting in considerably less incident power absorbed by the semiconductor. The number of photo-excited carriers turns out to be much larger in metal than in the semiconductor, further hindering the detection of holes injected from the semiconductor. Transparent conducting oxides like ITO are not suitable due to their often process-dependent band gaps on the order of 4 eV, which will cut off nearly all the photons with energy larger than the gap [47]. Goodman et al. attempted to address this experimental challenge by replacing the metal electrode with water [48]. However, this approach is inconvenient since the use of a water electrode significantly complicates the fabrication of devices of interest and the measurement setup.

In this section, we propose and demonstrate an important application of graphene as an elegant solution to this metrology challenge by utilizing graphene as a transparent electrode to collect photo-generated carriers in IPE. Its high transparency over a wide spectral range (IR/Visible/UV) enables direct observation of the hole injection, and facilitates determination of *both* conduction and valence band offsets at the semiconductor-insulator junction or hetero-junction. In addition, hole transition detection will also allow one to characterize other electronic properties at the interface such as interfacial dipoles, carrier trapping effects, hole transport, etc [35]. Finally, with direct and precise measurements of both the electron and hole barrier heights one can accurately deduce the band gap of the insulator, therefore providing a complete energy band diagram alignment of the heterostructure [36, 46].

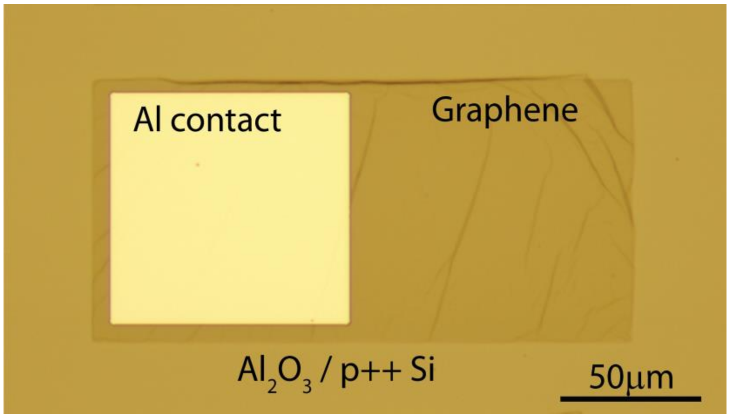

Figure 2.9 Optical image of the graphene-Al2O3-Si sample.

Different from SiO_2 with very wide band gap, application of Al_2O_3 as oxide layer enables us to observe the hole transition at lower photon energies. The optical image of the sample is shown in Figure 2.9. Figure 2.10 (a) shows the photocurrents, due to either electron or hole transitions between Si and graphene measured as a function of incident photon energy under various gate voltages. V_{fb} is found to be about 0.6 V with respect to the grounded graphene, which is in good agreement with a previous band alignment analysis in Section 2.2.2. When V_{gs} = -2.9, -2.8, -2.7, -2.6 V, much smaller than V_{fb}, the spectral photocurrent tends to go negative for the above threshold photons, which corresponds to the energy diagram depicted in Figure 2.10 (b). In this case, the electric field in the oxide drives the electrons (photo-excited above the Al_2O_3 conduction band bottom) from Si into graphene. On the other hand, when V_{gs} = 2.6, 2.7, 2.8, 2.9 V, the reversed electric field drives holes excited in Si into graphene as depicted in the energy diagram in Figure 2.10 (c). In the latter case, the photo-carriers excited in graphene and injected into Si are negligible since the photon absorption is low for graphene (< 5%) compared to that by Si (> 30%) over the entire spectral range in the measurement. Further evidence of the hole injection will be presented below in the data analysis. This demonstrates that by taking advantage of the uniquely transparent nature of graphene we have overcome the previous difficulty of detecting hole injection in IPE when metals are commonly used as an electrode.

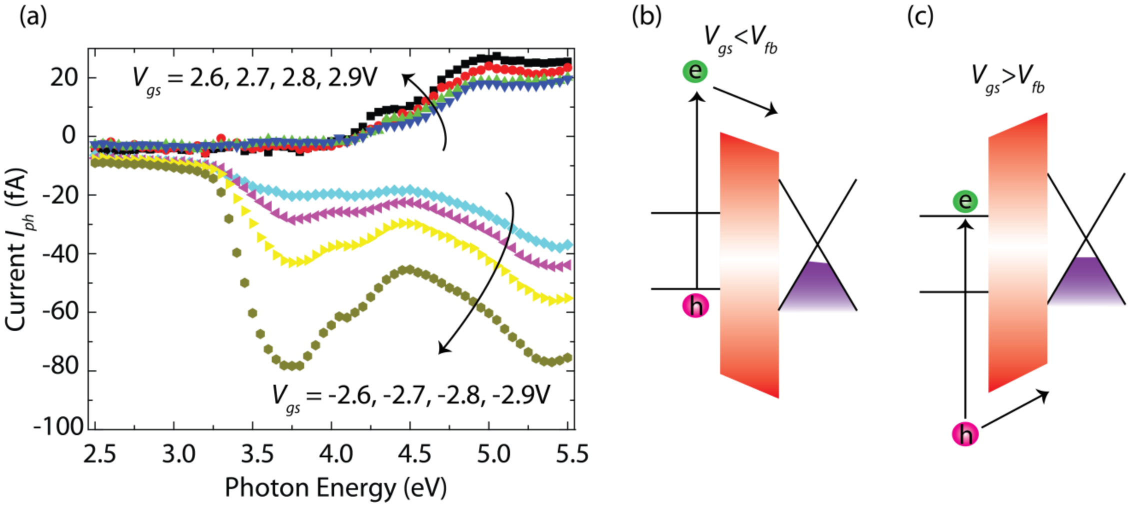

Figure 2.10 (a) Measured photocurrent as a function of incident photon energy. Gate voltage is applied to modulate the electric field in the oxide. (b) and (c) Schematic illustrations of electron and hole transitions determined by the direction of the oxide electric field.

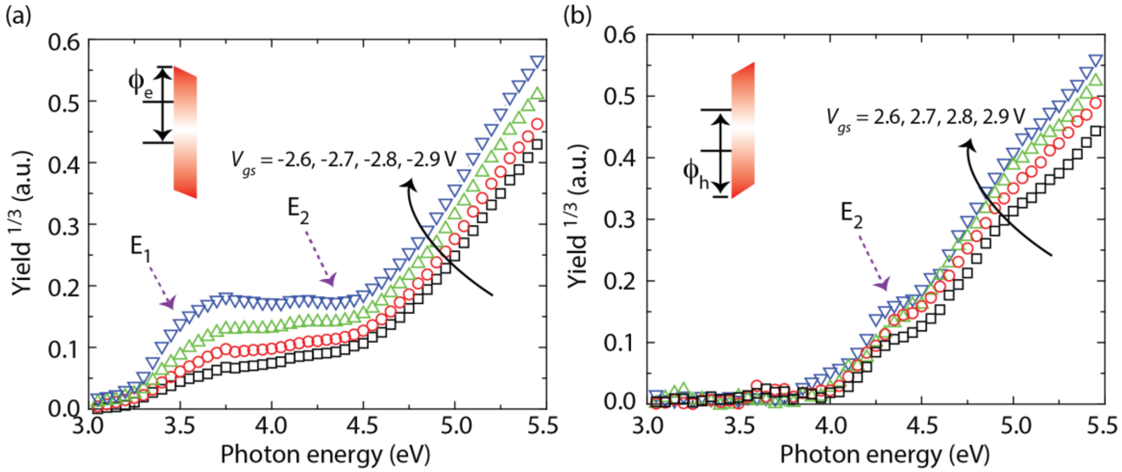

Figure 2.11 (a) and (b) Cubic root of the quantum yield obtained by normalizing photocurrent to the incident light flux. The threshold of the yield varies with the applied gate voltage.

The electron or hole barrier height is directly determined from the photoemission quantum yield as described by Eq 2.1 with $p = 3$. Shown in Figure 2.11 (a) and (b) are the $Y^{1/3}$ vs. $h\nu$ plots for the negative (electron) and positive (hole) photocurrents, respectively. The yield starts to increase sharply and linearly near the barrier height threshold. The noticeable features in both injection spectra are the kink at ~4.4 eV and the change of slope at ~3.5 eV, which is used to differentiate hole injection from electron one.

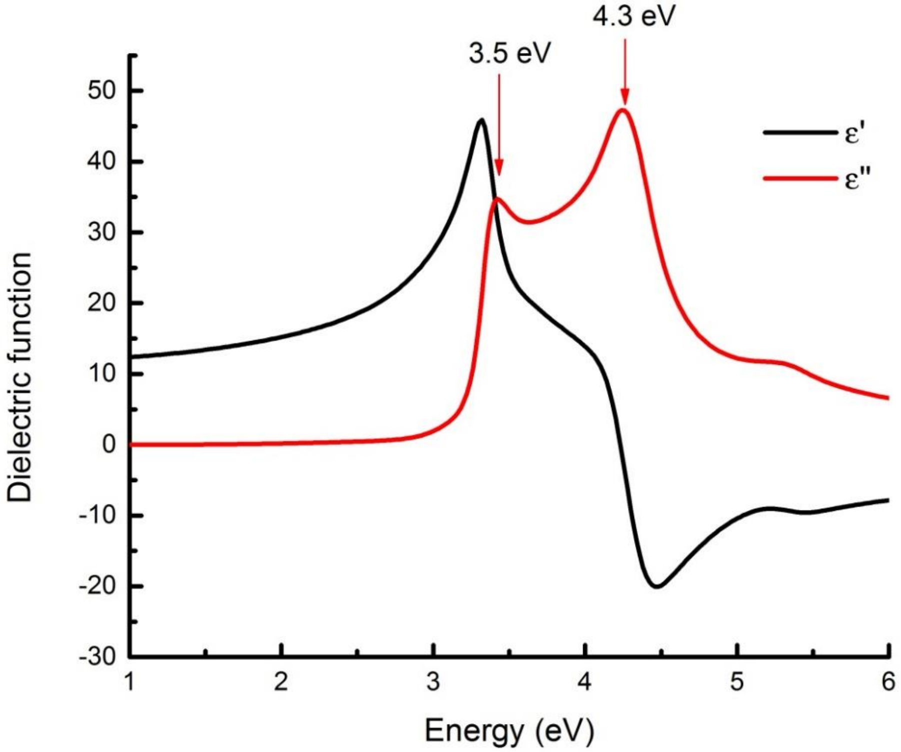

Figure 2.12 Real and imaginary part of dielectric function of crystalline Si.

The presence of these features offers critical correlations to assessing the origin of photocurrent. The positions of the 3.5 eV and 4.4 eV features in the yield plot align perfectly with the optical singularities (E_1 and E_2) of crystalline Si (see Figure 2.12, there are two prominent peaks at 3.5 eV and 4.3 eV in imaginary part of dielectric function of Si), thus indicating that both currents primarily stem from carrier injection (electron or hole) from the Si substrate but not from graphene. The negative bias branches in Figure 2.10 (a) due to electron injection from Si, contain both features, which indicates the effective barrier height for electrons (ϕ_e) is lower than E_1, the smaller of the two. The positive bias branches in Figure 2.10 (b) due to hole injection from Si show the E_2 transition only, and the vanishing of E_1 in the yield plot suggests that the barrier height for holes is larger than E_1.

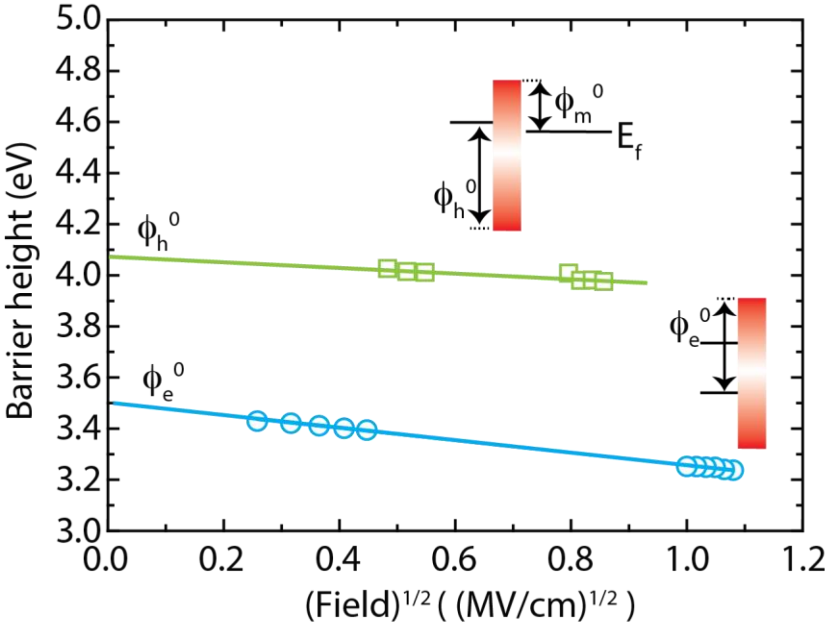

Figure 2.13 Schottky plots of electron and hole carrier injections as a function of the square root of the electric field. The linear extrapolation to zero field gives rise to the zero-field barrier height.

The zero-field barrier heights of electron (ϕ_e^0) and hole (ϕ_h^0) could be obtained by a linear fit of ϕ versus $F^{1/2}$ as shown in Figure 2.13, following Eq 2.2. The barrier height from the top of the Si valence band to the bottom of the Al_2O_3 conduction band, ϕ_e^0, is found to be 3.5 eV ± 0.1 eV; the barrier height from the bottom of the Si conduction band to the top of the Al_2O_3 valence band, ϕ_h^0, is found to be 4.1 eV ± 0.1 eV.

Unlike prior approaches, implemented for IPE measurements that suffer from inherent limitations, our approach enables direct observation of the hole transition and provides simultaneous and exclusive information about the conduction and valence band at critical material interfaces. One additional and beneficial outcome from our approach is that the band gap (E_g) of the insulator can be easily deduced from the electron and hole energy barrier heights by this simple relation: $E_g{}^{\text{oxide}} = \phi_e^0 + \phi_h^0 - E_g{}^{\text{semiconductor}}$, which can be compared with bandgap values derived from purely optical measurements and modeling. In this particular study using ALD Al_2O_3, we find $E_g{}^{\text{Al2O3}} = \phi_e^0$ (3.5 eV) + ϕ_h^0 (4.1 eV) - $E_g{}^{\text{Si}}$ (1.1 eV) = 6.5 ± 0.2 eV. This method of determining the band gap is preferred for some material systems because it is free from possible marring induced by excitonic effects [34]. To verify the bandgap value of our ALD Al_2O_3, we also performed vacuum ultraviolet spectroscopic ellipsometry (VUV-SE) measurement on the same Al_2O_3/Si structure, which revealed a band gap of 6.5 ± 0.05 eV, in an excellent agreement with the value determined by IPE. It is worth pointing out that the band gap of Al_2O_3 highly depends on growth conditions and the thickness. It is thus expected that the band gap of amorphous Al_2O_3 grown by ALD differs from that (9.5 eV) of bulk crystalline Al_2O_3.

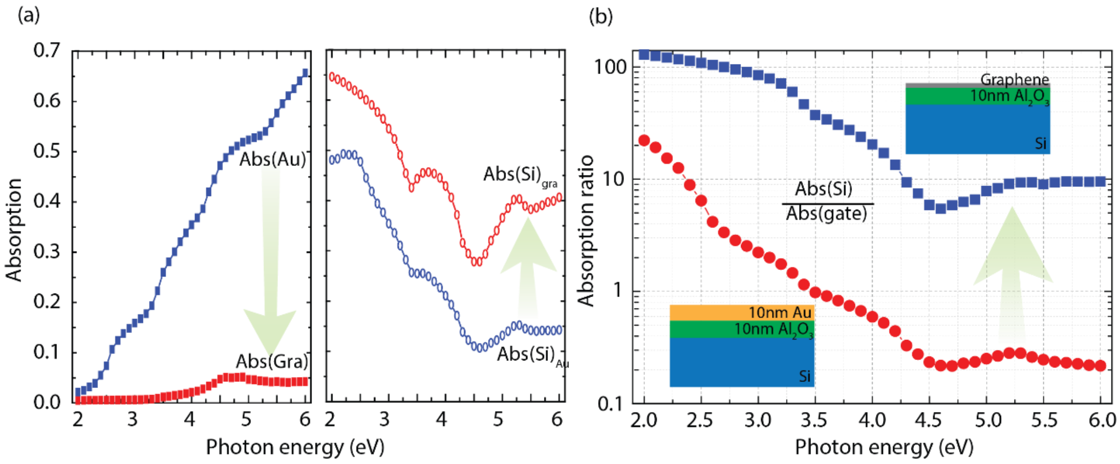

Figure 2.14 (a) Modeled optical absorption by graphene (Abs(Gra)), 10 nm Au (Abs(Au)), and Si (Abs(Si)$_{gra}$ and Abs(Si)$_{Au}$). (b) The ratio of graphene absorption over Si in a graphene-Al_2O_3-Si structure and that of Au absorption over Si in an Au-Al_2O_3-Si structure.

To further investigate the advantage of using graphene as the collector electrode over traditional metals, we have quantitatively evaluated absorption by each layer in the graphene-oxide-semiconductor (GOS) and metal-oxide-semiconductor (MOS) IPE test structures. Let us consider the case of normal optical incidence in air with a refractive index $n_0 = 1$ into a three-layer stack consisting of semitransparent electrode (metal or graphene), Al_2O_3 and Si with a complex and wavelength-dependent refractive index of n_1, n_2 and n_3, respectively. The thickness of the metal or graphene is d_1, and that of the oxide is d_2. Also it is assumed the Si substrate being semi-infinitely thick and Al_2O_3 being transparent with a zero imaginary refractive index in the entire optical range. For a single-layer graphene, n_1 measured by spectroscopic ellipsometry [49] and a thickness of 0.34 nm are used. With described geometry, it is straightforward to show the reflection by the entire stack is given by

$$R = |E_0^-/E_0^+|^2$$

$$= \left|\frac{r_1 + r_2\exp(2\delta_1) + r_3\exp 2(\delta_1+\delta_2) + r_1r_2r_3\exp(2\delta_2)}{1 + r_1r_2\exp(2\delta_1) + r_1r_3\exp 2(\delta_1+\delta_2) + r_2r_3\exp(2\delta_2)}\right|^2 \quad 2.5$$

where r_i's are the Fresnel reflection coefficients defined as:

$$r_1 = \frac{n_0 - n_1}{n_0 + n_1}\ , \qquad \mathrm{r}_2 = \frac{n_1 - n_2}{n_1 + n_2}\ ,$$

$$r_3 = \frac{n_2 - n_3}{n_2 + n_3} \quad 2.6$$

and the phase factor δ_i relates to the film thickness as:

$$\delta_1 = -i\left(\frac{2\pi}{\lambda}\right)n_1d_1\ ,\ \ \delta_2 = -i\left(\frac{2\pi}{\lambda}\right)n_2d_2 \quad 2.7$$

The power transmission into Si is given by:

$$T = Re(n_3)|E_3^+/E_0^+|^2$$

$$= Re(n_3)\left|\frac{(1+r_1)(1+r_2)(1+r_3)\exp(\delta_1+\delta_2)}{1 + r_1r_2\exp(2\delta_1) + r_1r_3\exp 2(\delta_1+\delta_2) + r_2r_3\exp(2\delta_2)}\right|^2 \quad 2.8$$

where E_0^+, E_3^+, and E_0^- are the amplitudes of the light waves incident, transmitted into the substrate, and reflected, respectively. Since we have assumed no absorption by Al_2O_3, the optical absorption (*A*) by the metal or graphene electrode becomes $A = 1 - T - R$. In Figure 2.14 (a), we compare the absorption by a 10-nm-Au or single-layer-graphene electrode and the corresponding absorption by Si. A striking difference is that the absorption by 10-nm Au is more than 50% for photons with an energy higher than 4.5 eV whereas that by graphene remains low (< 6%) over the entire spectral range. Consequently, higher optical power can reach and be absorbed by Si with an enhancement from 10% ($\mathrm{Abs(Si)_{gra}}$) to 40% ($\mathrm{Abs(Si)_{Au}}$) in the high photon energy region, which is particularly important for extracting large energy barrier heights such as the energy barrier of holes. It is also worth noting that absorption by graphene is dependent on the oxide thickness. The oxide thickness used in IPE measurements is typically on the order of 10 nm, thus its optical thickness is less than one tenth of the wavelength of a 6 eV photon. In test structures with thicker oxides, cavity enhanced absorption by graphene can be up to 4x higher [50]. Figure 2.14 (b) shows the improved absorption in Si by adopting the graphene transparent electrode: the ratio of absorption by Si to that by graphene is over one order of magnitude larger than the ratio of absorption by Si to that by Au for nearly the entire spectral range. This analysis supports our initial expectation that the graphene IPE electrode can substantially augment absorption by semiconductor while suppressing it by the collector electrode. Thus, the photocurrents are predominantly due to carrier injection from the semiconductor, which has led us to directly observe hole injection in an IPE measurement.

In summary, we have demonstrated a unique and experimentally facile approach to extract a complete energy band alignment using IPE measurements by employing graphene as the semitransparent collector electrode. Though the demonstration was performed on model structures using Al_2O_3/Si and SiO_2/Si, this technique can be broadly and readily extended to most structures studied by IPE measurements. The method presented here is largely free from experimental complexities and limitations commonly experienced by the prior methods, thus representing a milestone in the advancement of IPE metrology and the field of semiconductor interface studies.

CHAPTER 3: GRAPHENE-BASED TERAHERTZ MODULATORS

Recently the THz frequency regime (0.1-30 THz) has become the subject of much attention due to its wide range of applications in astronomy, imaging, spectroscopy, etc. [51, 52]. Significant efforts and progress of closing 'THz gap' has been made on sources and detectors. However, components of efficiently manipulating THz waves – THz modulators, are still lagging behind [53]. In this chapter, we will first review the development of various THz modulators, and then introduce graphene-based modulators including principles and device scheme. Finally, the most recent progress that combines metamaterial and graphene in THz modulators will be discussed in detail. Note that modulators could be divided into different types based on the modulation medium, active control mechanism, or the physical quantity they control, etc. Here in this work, we mainly focus on ones modulating THz wave *amplitude* by cataloging them in terms of modulation material used.

3.1 The development of reconfigurable THz modulators

Modulators simultaneously equipped with high modulation depth, low insertion loss and facile integration are in great demands to realize sophisticated THz communication and imaging system. A few types of modulators in THz regime have been demonstrated up to date, including ones based on two-dimensional electron gas (2DEG), metamaterial, phase-change materials such as VO_2, MEMS, and graphene.

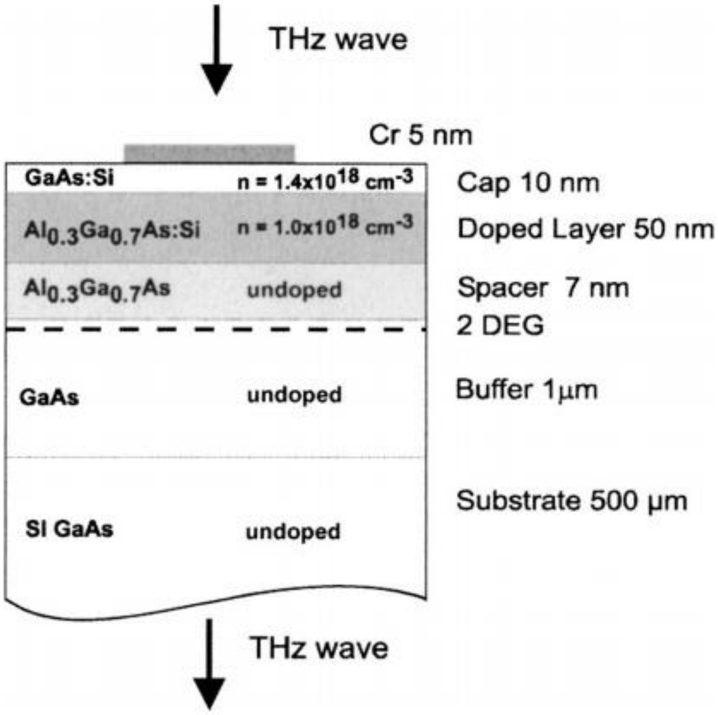

Figure 3.1 Structure of the THz modulator based on 2DEG [54].

In 2004, Kleine-Ostmann et al. demonstrated a room-temperature electrically-driven THz wave modulator based on electron density modulation in a gated 2DEG [54]. The HEMT-like device structure as shown in Figure 3.1 is used, where a few nanometers thick 2DEG layer exists between GaAs/AlGaAs interface. By tuning electron density through the application of a top gate voltage, THz waves transmission is tuned. However, the maximum modulation observed is only 3%, which is far from the requirements of practical applications. Further investigations found that the proposed 2DEG structure suffers inherent limitations from metal gates [7]. It is expected that replacing metal gate with graphene can notably improve the modulation and decrease the loss.

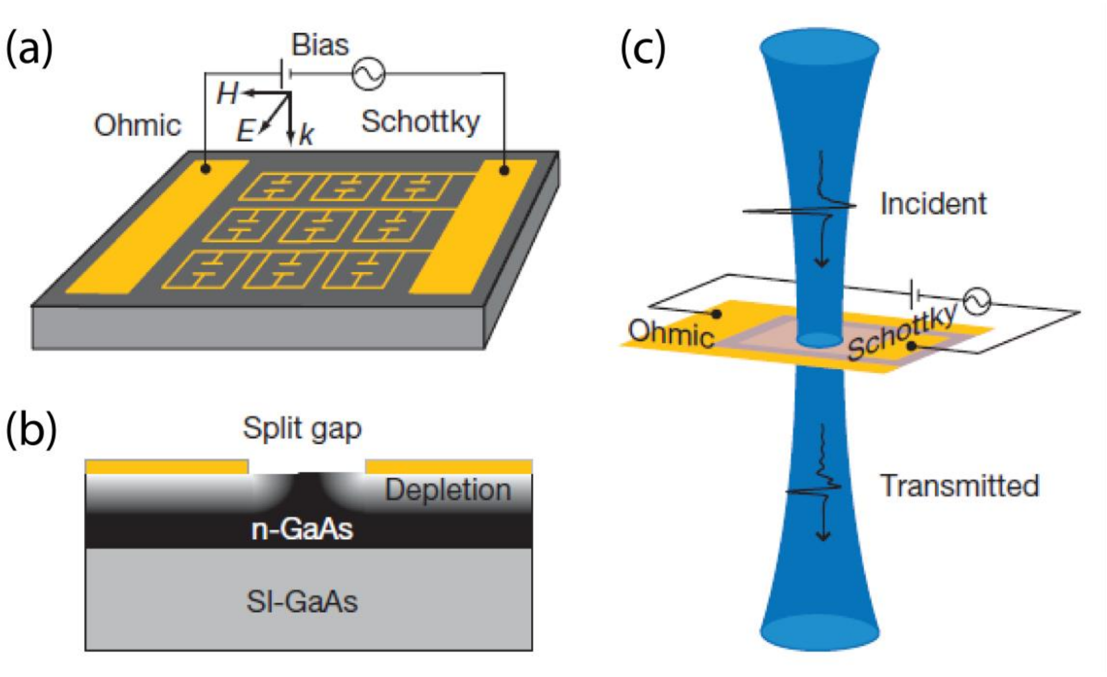

Figure 3.2 (a) The device structure with arrays of metamaterial elements in a period of 50μm. A voltage bias is applied between ohmic and Schottky contacts to tune the carrier density in the split gap. (b) Cross section of the substrate showing a layer of depletion region in the split gap [55].

Another intelligent way of realizing THz wave modulation is to fabricate metamaterial on a n-type GaAs layer covered semi-insulating (SI) GaAs substrate, which was first developed by Chen et al. in 2006 [55, 56]. The device structure is shown in Figure 3.2 (a) and (b), where a split ring resonator is used for two purposes: effectively manipulate THz waves and to create a Schottky diode to deplete carriers in the doped GaAs below the split gap. Due to the fact that the electric field is highly concentrated in the gap as shown in Figure 3.3, the THz transmission through the whole structure is only sensitive to the carrier concentration underneath the metamaterial gap, which is controlled by a voltage applied between the ohmic and Schottky contacts. While a zero bias is applied, the resonance response of the structure is damped due to the lossy n-type GaAs layer. While a negative voltage applied, the carriers are depleted thus the metamaterial resonation is re-built. A 50% intensity modulation is demonstrated in their work. Encouraged by this pioneering work, some other progress are made in the following years including eliminating polarization dependence [57], achieving higher modulation depth and speed [58], realizing phase modulation [56].

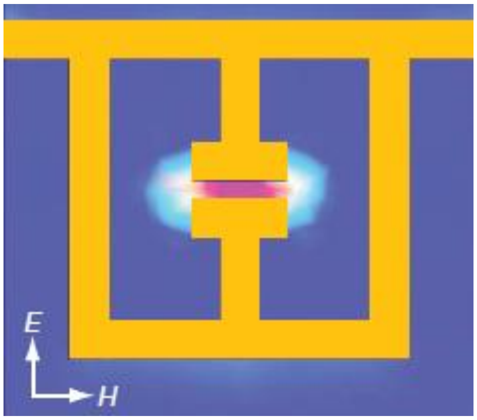

Figure 3.3 Simulated electric field intensity at resonant frequency [55].

Optical modulation is also a promising approach besides electric tuning shown above [59, 60]. By illuminating semiconductors like GaAs or Si with different light intensity, THz transmission through the structure could be drastically modulated due to the present of photo-carriers. Highest modulation achieved to date is about 80% in a metamaterial/GaAs hybrid structure by Padilla et al. in 2006 [59].

MEMS-based reconfigurable mesh filters are recently proposed and experimentally demonstrated by Jarrahi's group [61, 62]. Although the modulation depth of 90% is observed but the relatively complicated fabrication procedure and slow modulation speed (20 kHz) inherently limits its potential for practical applications.

The advent of graphene in recent years provides a premium solution to THz technology. Our group have demonstrated graphene could realize efficient THz wave modulation through the modification of conductivity, which controls the intraband transitions in monolayer graphene [29].

3.2 Graphene properties in the THz range

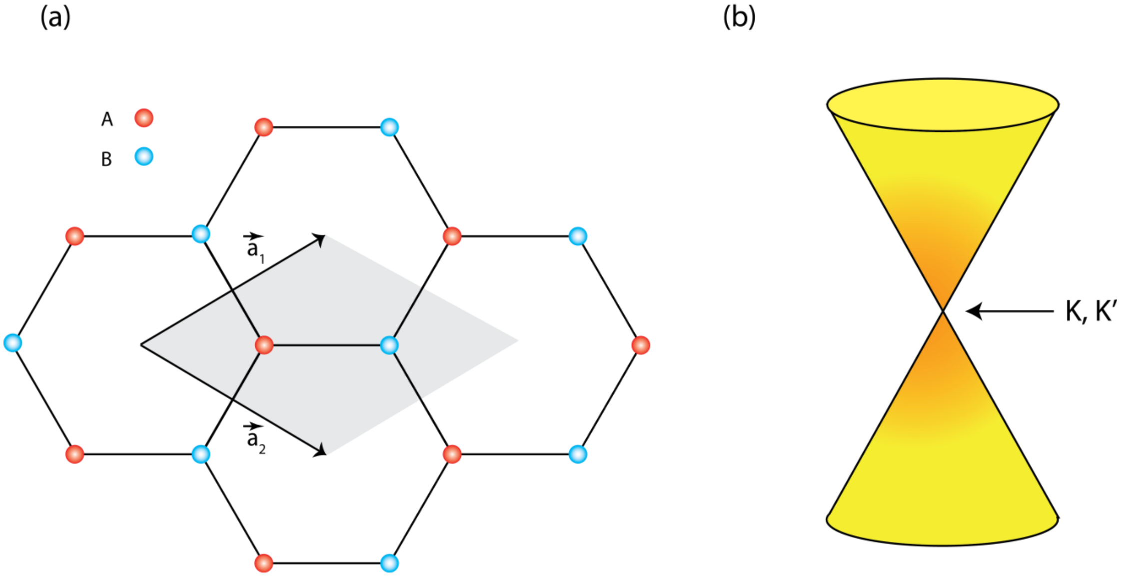

Figure 3.4 (a) Lattice structure of graphene in real space. Grey shaded area indicates one unit cell containing two carbon atoms A and B. (b) Linear band structure with conduction and valence band degenerate at K, K' point in reciprocal space.

The atomic structure of graphene is shown in Figure 3.4 (a), where one unit cell contains two carbon atoms (A, B). The lattice symmetry directly leads to a linear dispersion at the edge of Brillouin zone (K and K') as sketched in Fig. 3.4 (b). Consequently, electrons propagating through 2D graphene system possess a symmetric, linear energy dispersion relation as [63]

$$E = \pm\hbar v_f|k| \tag{3.1}$$

where $\hbar$ is planck constant over 2π, v_f is Fermi velocity of 10^6 m/s, and k is momentum in reciprocal space.

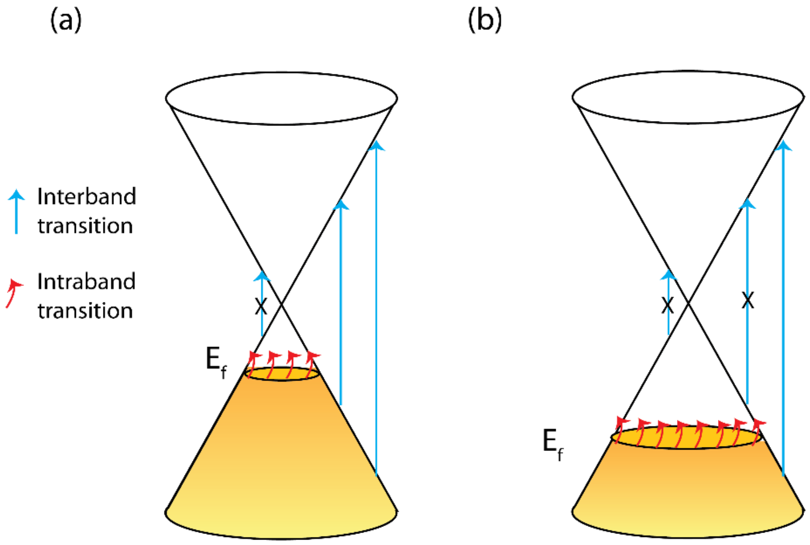

Figure 3.5 (a) and (b) Band diagrams of graphene with two different Fermi levels showing the interband (blue arrow) and intraband (red arraow) transitions. In THz range, intraband transition dominates due to the small photon energy required. As Fermi level goes further from Dirac point ((a) to (b)), states of free carriers available for intraband transition increases.

The optical properties of graphene could be explored by examining its optical conductivity [64]. The photons incident into a material could induce two types of transitions: intraband and interband, as depicted in Figure 3.5. Therefore, the optical conductivity of graphene as a function of light frequency could be written as the sum of intraband ($\sigma_{intra}(\omega)$) and interband ($\sigma_{inter}(\omega)$). Calculations staring from the tight-bonding Hamilton give the expressions of optical conductivity when $E_f \gg k_B T$ as [65-67]

$$\sigma_{intra}(\omega) = \frac{ie^2|E_f|}{\pi\hbar^2(\omega + i\tau^{-1})} \qquad 3.2$$

$$\sigma_{inter}(\omega) = \frac{ie^2\omega}{\pi}\int_0^\infty \frac{d\epsilon\left[f\left(\epsilon - E_f\right) - f(-\epsilon - E_f)\right]}{(2\epsilon)^2 - (\hbar\omega - i\Gamma)^2} \qquad 3.3$$

$$\sigma = \sigma_{intra}(\omega) + \sigma_{inter}(\omega) \qquad 3.4$$

where E_f is Fermi level relative to the Dirac point, f(ϵ) is Fermi function, τ is momentum relaxation time, Γ describes the broadening of interband transition and k_B is Boltzmann constant. Taking the relation $\hbar\omega \gg 2E_f$ in Eq. 3.4, $\sigma_{inter}(\omega)$ results in a constant value of $e^2/4\hbar$, thus a universal absorption of 2.3% per layer graphene in a wide spectrum range [7]. Thanks to this small and constant absorption, we utilized graphene as transparent electrode in IPE as discussed in Chapter 2. On the other hand, in the THz/FIR range where $\hbar\omega \ll E_f$, intraband transition depicted by red arrows in Figure 3.5 (b) determines the value of optical conductivity with negligible interband contribution. It could be understood that the interband transition, which needs photon energy larger than $2E_f$, is negligible because of the low incident photon energy. To satisfy the momentum conservation, the extra scattering with phonons or defects is required. Therefore, it is expected that $\sigma_{intra}(\omega)$ in Eq. 3.2 exhibits characteristics of Drude mode conductivity [1, 68-70]. Now we rewrite intraband conductivity as [71]

$$\sigma_{intra}(\omega) = \frac{iD}{\pi(\omega + i\tau^{-1})} \qquad 3.5$$

where the prefactor D, known as the Drude weight, should have the form of $D = e^2|E_f|/\hbar^2$ compared to Eq.3.2. This is distinctly different from the other materials which usually have $D = \pi ne^2/m^*$. The real part of $\sigma_{intra}(w)$ could be further written as

$$Re\left(\sigma_{intra}(\omega)\right) = \frac{\tau D}{\pi(1+\omega^2\tau^2)} = \frac{\sigma_{DC}}{1+\omega^2\tau^2} \qquad 3.6$$

where $\sigma_{DC} = D\tau/\pi$, is Drude-like DC conductivity of graphene. Bases on this, we could correlate electric and optical conductivity. First, the real part of the frequency dependent conductivity directly relates to the THz/FIR light absorption in graphene. Therefore, one could use Fourier transform infrared spectroscopy (FTIR) or time/frequency domain THz spectroscopy to measure the transmission of graphene and then extract the values of D and τ by fitting the measured spectra. In such a way, the DC and frequency dependent conductivity could be determined. Second, the DC conductivity could be easily deduced from IV measurements. Recent experiments by Horng et al [71] and Maeng et al [72] have confirmed that the conductivities deduced by two methods above match with each other within the error of set-ups. These are clear demonstrations of the nature of massless Dirac fermions for carriers in graphene.

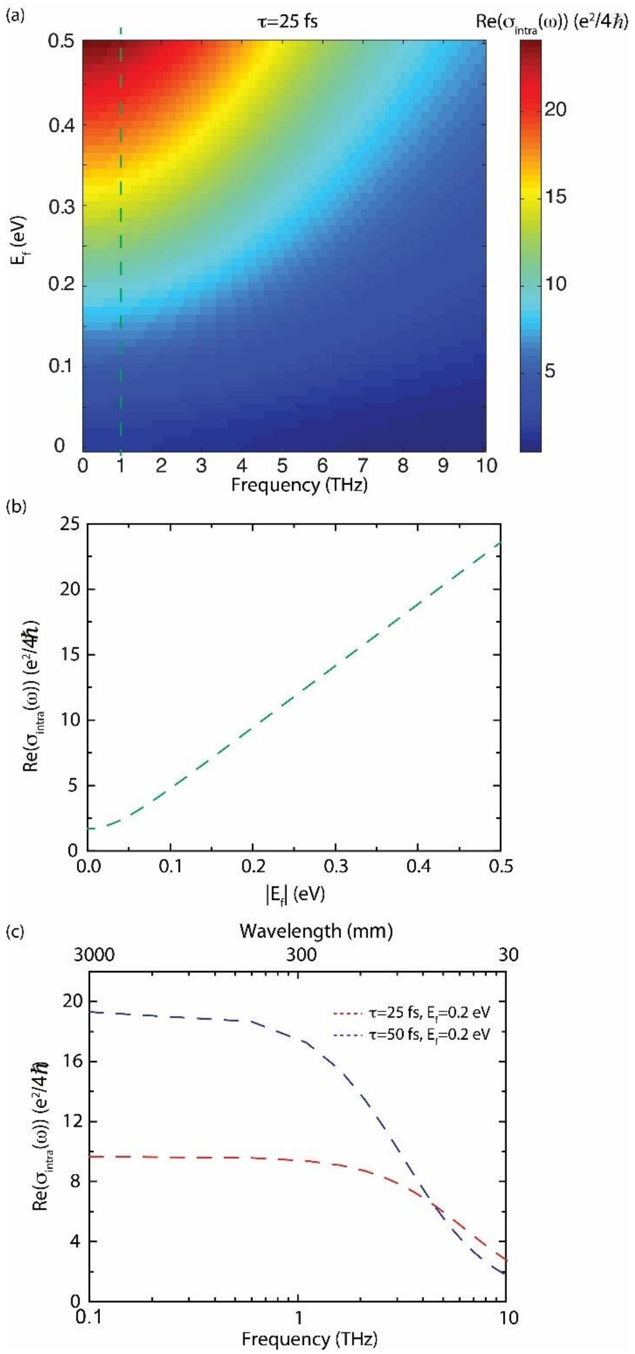

Figure 3.6 (a) $\sigma_{intra}(\omega, E_f)$ with carrier relaxation time $\tau =$25 fs. (b) The relation between Fermi level and σ_{intra} at frequency of 1THz. As $|E_f|$ increases, optical conductivity increases almost linearly, leading to the increasing absorption of THz light. (c) $\sigma_{intra}(\omega)$ with the different carrier relaxation times but same Fermi level $E_f = 0.2$ eV, showing the large effects of carrier lifetime at THz frequency below several THz.

In Figure 3.6, we plot the real part of optical conductivity which determines the absorption of light by graphene, as a function of frequency and Fermi level assuming τ = 25 fs. Different from constant absorption in visible region, THz conductivity is very sensitive to the Fermi level in graphene. As E_f moves away from the Dirac point, THz conductivity increases, which relates to higher absorption in graphene. This observation coincides with the sketch of Figure 3.5 where graphene with higher $|E_f|$ exhibits more density of states available for intraband transitions. Therefore, by tuning the graphene Fermi level by some way, the THz transmission through graphene could be varied. This is the fundamental mechanism we employed in our graphene-based THz modulators.

One most favorable way to dynamically tune Fermi level thus THz conductivity from the perspective of device application is electro-statistic modification. Through the field effect, carrier concentrations in graphene could be efficiently changed. The 0 K approximation of the relationship between E_f and n (or p) could be obtained as $E_f = \hbar v_f \sqrt{\pi |n|}$, which is widely adopted [3, 38]. Other means of tuning conductivity include optical [73], chemical [74, 75] etc..

3.3 Broadband active graphene THz modulators

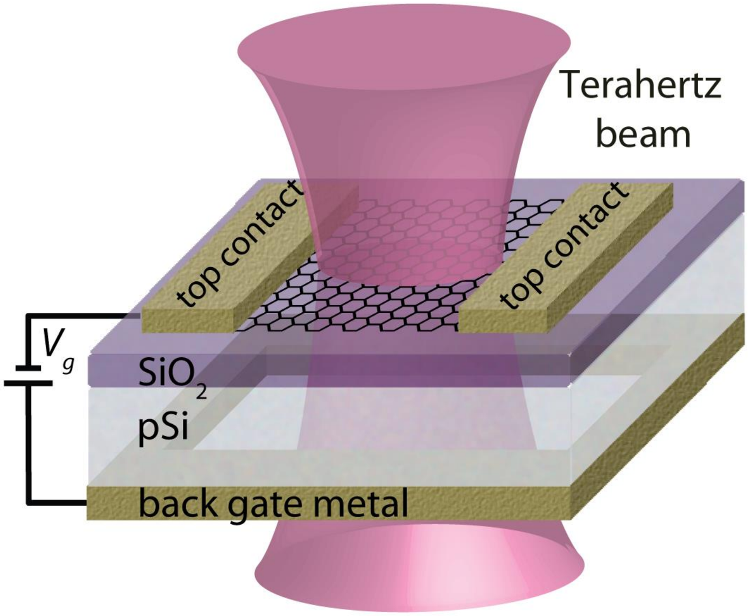

Figure 3.7 The structure of electro-absorption THz modulator which consists of a graphene on SiO_2 covered p-type Si substrate. The THz beam is normal incidence to the structure [29].

As the first experimentally demonstrated graphene-based THz modulator, our proof-of-concept device employs a graphene-SiO_2-Si structure as shown in Figure 3.7, to tune the THz wave transmission by applying a voltage between the top contact and the back gate metal [29, 76].

A 1.5 x 1.5 cm^2 monolayer graphene layer grown by CVD on Cu foil was transferred onto a 300 nm SiO_2 covered Si substrate. To avoid the free carrier loss induced by the substrate, a lightly doped p-type Si wafer is used. Then top and back side contacts were deposited by e-beam evaporation. The detailed graphene transfer process will be present in the Appendix A.

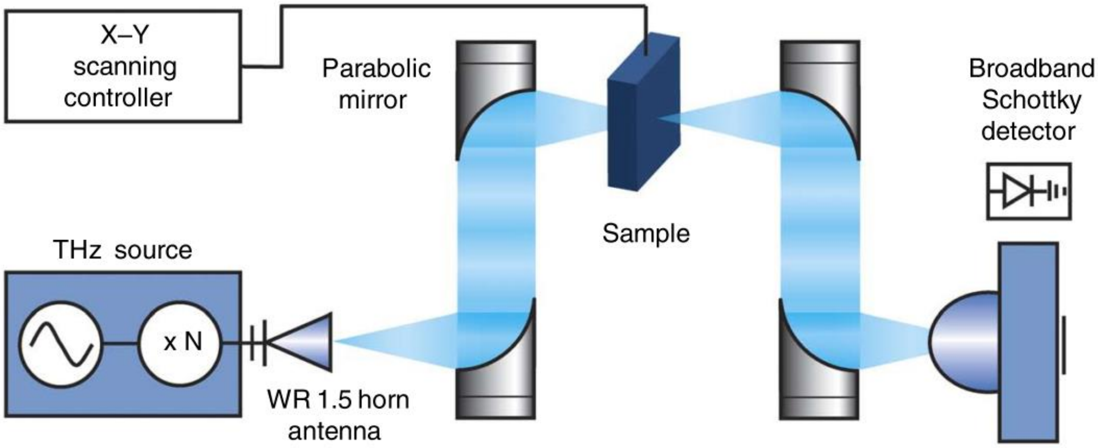

Figure 3.8 Schematic of the frequency domain terahertz imaging and spectroscopy system, using a broadband Schottky diode intensity detector to measure transmission of terahertz beam in the 570–630 GHz frequency band [29].

The THz transmittance was measured in the frequency domain employing a VDI (Virginia Diodes, Inc.) THz source that produces frequency-domain THz radiation in the region of 570-630 GHz [77]. The THz radiation from the source was focused onto the sample by two parabolic mirrors and then transmitted signal is coupled into a zero bias Schottky diode broadband THz detector. The schematic of the measurement set-up is shown in Figure 3.8. The spatial resolution of the system is given by the minimum beam width, which in these setups was estimated to be <1 mm at 600 GHz. Terahertz transmission spectroscopy was performed by sweeping the source frequency. Transmittance was estimated by normalizing the detector response with a sample to that without a sample.

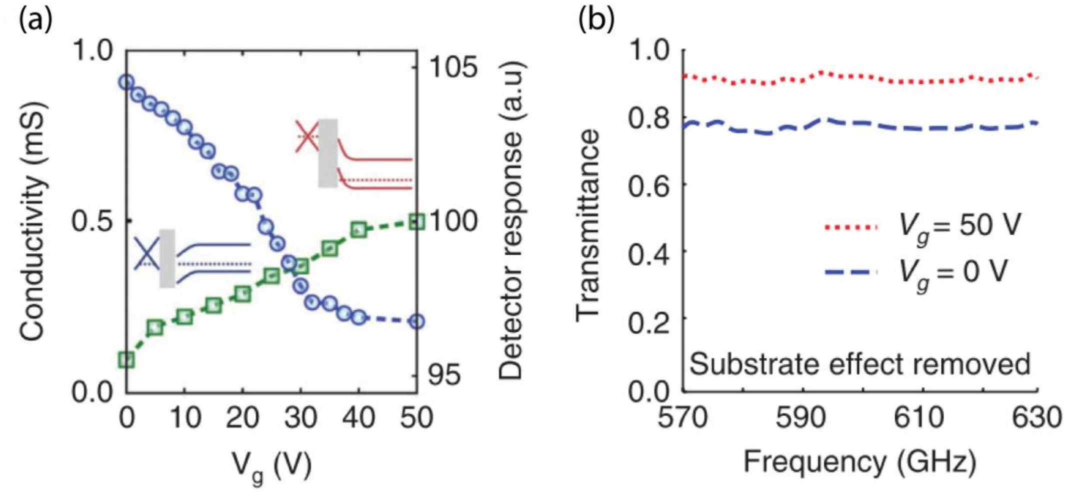

Figure 3.9 (a) Measured DC conductivity (blue circles) and detector response (green squares) at 600 GHz as a function of gate voltages. The insets respectively show the band diagrams of graphene-SiO_2-Si structure when the gate voltage is 0V and 50V. (b) Measured transmission intensity after removing the substrate and free carrier absorption in lightly doped Si substrate under two gate voltages [29].

Figure 3.9 (a) shows the DC conductivity (blue circles) and the detector response (green squares) at 600 GHz, where it could be clearly seen that transmission increases with decreasing DC electrical conductivity as expected. Because the Dirac voltage is ≥ 50, so it could be inferred that the graphene is p-type in all the range of scanned gate voltage from 0 to 50 V. The transmission spectrum at two gate voltage values after removing the substrate oscillation effects is shown in Figure 3.9 (b). The flat transmission characteristic of this modulator promises the intrinsically broadband operation. Modulation depth (MD) defined as $(T_{max} - T_{min})/T_{max}$ could be calculated to be 15±2% over the entire spectrum.

It is necessary to mention the effects of p-type Si substrate. As could be seen in the insets of Figure 3.9 (a) where the band diagrams of graphene-SiO_2-Si clearly indicates that at V_g =0 V, holes are accumulated in graphene but those in Si are depleted; at V_g= 50 V, holes concentration in graphene are heavily reduced but they are present at Si near the Si/SiO_2 interface. There is no doubt that these holes present near the Si/SiO_2 interface play a role of absorbing THz radiation as free carriers, which means, the measured transmission at V_g=50 V is lowered than that with graphene alone. We could simply estimate the conductivity difference of these holes in graphene and Si by comparing their mobility if assuming same amount of carrier concentration on both sides with $\sigma = ne\mu$. The carrier mobility $u = \Delta\sigma/C_{SiO_2}\Delta V_g$~600 cm^2/Vs is obtained in graphene however that of holes in Si is only about 80 cm^2/Vs. Consequently, the conductivity modulation in Si is 7.5 times smaller than the in graphene. Taking this into account, we could conclude that the intensity modulation depth of terahertz beams due to graphene alone is therefore 15±2%.

The promising performance of this prototype graphene modulator opened up a way for future THz devices. However, limited by the conductivity swing of typical quality of the state-of-the-art large-area graphene, such designs still cannot ensure practical applications. To overcome this obstacle, a few strategies are reported recently to improve the modulation depth and speed, and simultaneously keep low insertion loss. One good example is developed by Sensale-Rodriguez et al [78] where a specifically designed SiO_2/Si substrate is used as a cavity to enhance the strength of electric field in the graphene plane to efficiently tune the reflection of THz waves. However, it is more difficult to apply reflection mode modulators into other systems than those in transmission mode, which is still lagging behind. Therefore, it is quite necessary to improve the performance of transmission mode devices. Following this demand, we came up with a new class of electrically tunable THz modulators [30, 31].

3.4 Near-field enhanced THz modulations

3.4.1 Switchable THz modulators

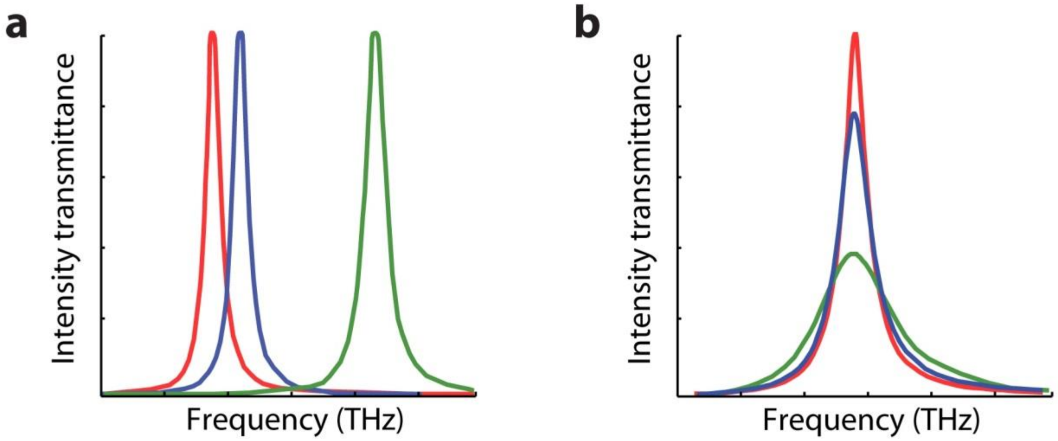

Figure 3.10 Schematics of the fundamental operation modes for switchable metamaterials. a) Resonant frequency shifting. b) Absorption/reflection tuning.

Here we proposed by taking advantage of enhanced electric field in the near field of metallic frequency selective surface (FSS), exceptional MD can potentially be achieved in graphene-based THz modulators. Besides graphene, our proposal could be extended to all possible electrically tunable elements including Si, MoS_2, oxides etc., thus opening up myriad opportunities for realizing high performance switchable metamaterials over an ultra-wide terahertz frequency range. Switchable metamaterials, touted as one of the frontiers of present metamaterial research, have two fundamental modes of operation, as shown in Figure 3.10. The first fundamental mode is to tune the resonant frequency of the entire structure (Figure 3.10 (a)) [79], generally realized by tuning the real part of the structure permittivity. Employing tunable magnetic materials is also possible, similar to the permittivity tuning. This mode of operation is particularly attractive for reconfigurable filter applications [80]. In terms of modulation at a fixed frequency, a good modulation can be obtained for a large shift in resonant frequency relative to the quality factor (Q) of the resonance itself (green curve relative to red curve). Previously reported FSS/semiconductor terahertz modulators primarily fall in this category [56, 57]. However, due to the finite frequency shift and the low Q of the metamaterial structure (blue curve relative to red curve), appreciable insertion losses were observed: > 55% intensity loss. The second fundamental mode is to tune the absorption/reflection at the resonant frequency (Figure 3.10 (b)), usually realized by tuning the imaginary part of the structure permittivity. The best modulation performance is typically achieved when the metallic FSS structure and the tunable element assume complementary patterns, which unfortunately becomes rather difficult to implement with side-gated tunable elements. The intrinsically broadband terahertz modulators demonstrated by Kleine-Ostmann et al. [54, 81] and Sensale-Rodriguez et al. [29] employ this tuning mechanism, which can be easily extended to switchable metamaterials. It is worth noting the recently reported plasmonic effects in graphene for tunable terahertz metamaterial is a result of tuning both the real and imaginary parts of the permittivity [82]; for a given graphene ribbon width, both plasmonic frequency (real part) and strength (imaginary part) increase with increasing carrier concentration.

3.4.2 Self-gated graphene pairs for THz wave tuning

In our design, we employ a new class of electrically tunable metamaterials consisting of capacitively-coupled layers of free carriers that are structurally complementary to, but, only electromagnetically connected with the metallic FSS structures. In the conventional devices, the metallic FSS serves both roles: frequency selection and electrical gating [55]. On the contrary, our proposed devices allow one to construct tunable metamaterials by placing the self-gated electron layers at optimal locations relative to the metallic FSS. This simple but elegant solution enables remarkably low insertion loss and high modulation depth simultaneously. Below, to illustrate this key design strategy, we use a pair of graphene as example self-gated electron layers and a square lattice of gold cross-slots as an example metallic FSS to construct a switchable metamaterial of the second kind (Figure 3.10 (b)). We also emphasize that the design methodology described here can be readily extended to other switchable metamaterials based on either operation mode as well as all other electrically tunable materials including conventional semiconductors, transition metal oxides and so on.

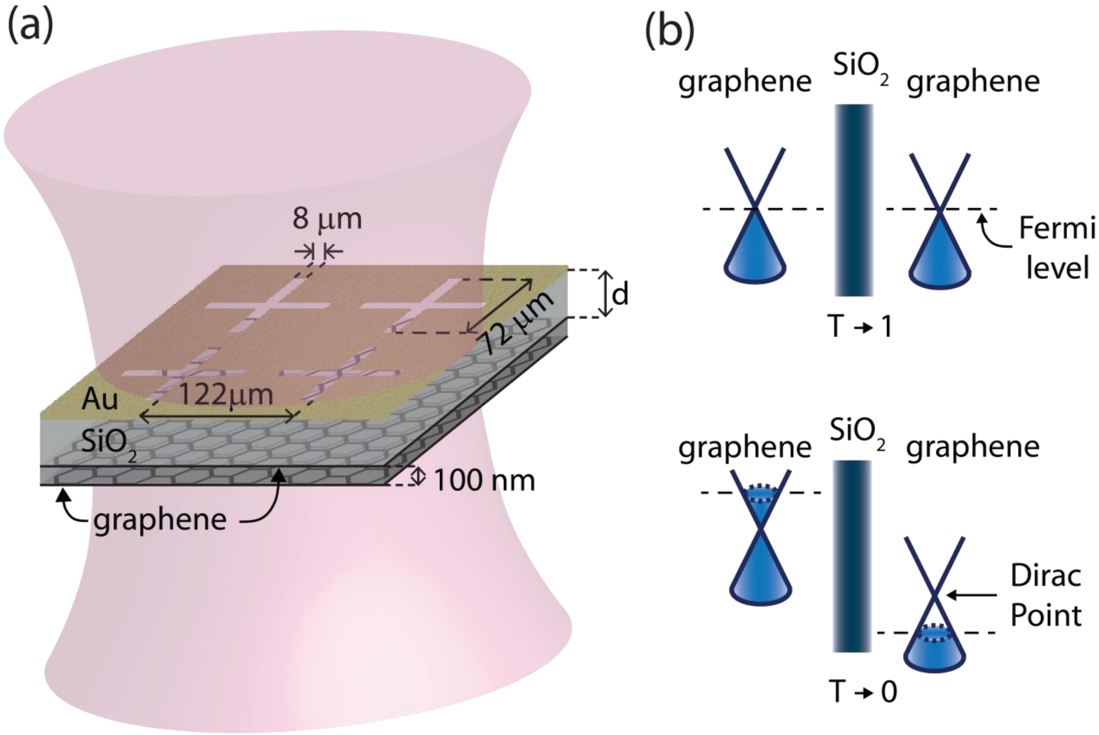

Figure 3.11 (a) The proposed THz modulator structure consists of a square lattice of gold cross-slot FSS and a pair of capacitively-coupled graphene layers situated at a distance d. The dielectric separating the FSS and graphene pair and between graphene layers is assumed to be SiO$_2$. The other dimensions used in simulation are shown in the graph. (b) Energy band diagrams of the graphene pair. At zero bias, the Fermi level is at the Dirac point of both graphene layers, leading to minimum conductivity and maximum terahertz transmission at the resonant frequency. When biased, the Fermi level moves into the conduction and valence band of the two graphene layers, respectively, resulting in an enhanced conductivity and minimized terahertz transmission.

The proposed THz modulator is shown in Figure 3.11 (a). In this tri-layer stack structure, the gold FSS plays the role of a band-pass filter with its center frequency (f_0) and bandwidth (Δf) determined by the mesh grid dimensions [83]. The graphene pair modulates the amplitude of the transmitted terahertz waves when their conductivities are tuned. The energy band diagrams of this graphene pair are shown in Figure 3.11 (b).

Considering the symmetric band structure of graphene around its Dirac point, we can assume the electrical thus optical conductivity of the two graphene layers to be the same. Therefore, the conductivity value assumed in all the figures in this section is that of a single graphene layer or half of the total conductivity of the 2DEG-pair.

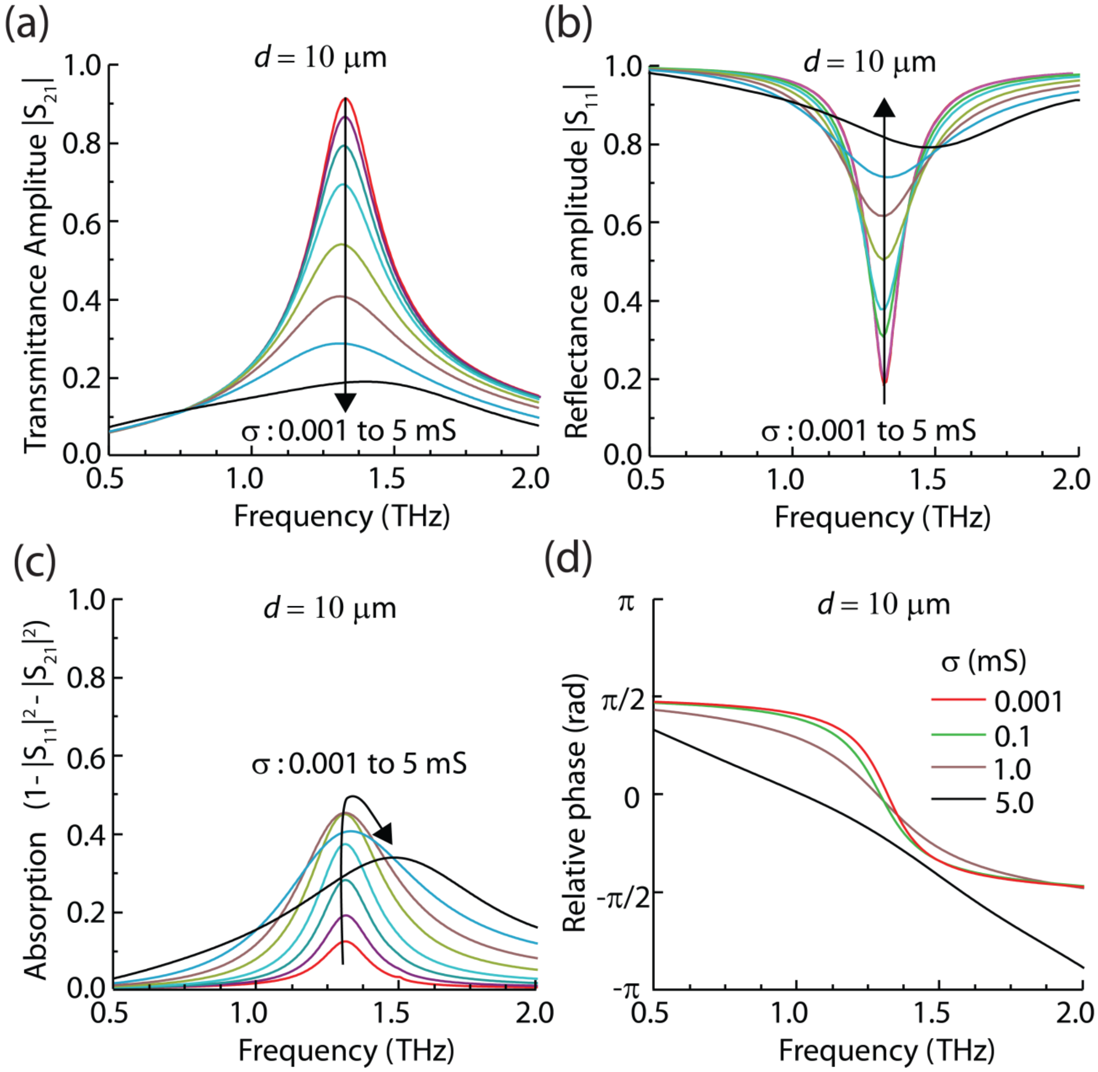

Figure 3.12 The simulated behavior of the example modulator as a function of half of the 2DEG-pair conductivity. (a) Transmittance (S_{21}) amplitude, (b) reflectance (S_{11}) amplitude, (c) associated absorption by the modulator, and (d) phase of transmittance. With increasing 2DEG-pair conductivity, both absorption in the 2DEG-pair and reflection by the modulator

increase. At very high conductivities (e.g. 5mS), a shift in
resonant frequency is observed, resulting in accompanied higher
reflection, reduced absorption and augmented phase shift.
There is negligible phase change at the resonant frequency
except at very high conductivities [30].

The two port S parameters of the modulator in Figure 3.12 (a) were simulated using a finite element based 3D electromagnetic solver: high frequency structure simulator (HFSS) by ANSYS, Inc. In Figure 3.12 (a) and (b) the amplitude of both S_{21} (transmittance) and S_{11} (reflectance) are plotted as a function of half of the 2DEG-pair conductivity, for d = 10 μm. The terahertz wave absorption by the metamaterial modulator can be extracted accordingly and is shown in Figure 3.12 (c). With increasing graphene conductivity, both reflection and absorption in the 2DEG-pair increase, leading to a decrease of transmission. For a moderate conductivity swing of 0.001 – 2 mS per 2DEG layer, the transmittance can be tuned in a large range while the resonant frequency does not shift. At very high conductivities, e.g. 5 mS per 2DEG layer, the absorption tends to decrease because of the increasing reflection. The maximum absorption by the 2DEG-pair is about 50%, consistent with what we discovered in broadband graphene terahertz modulators [29]. The phase of transmittance is plotted in Figure 3.12 (d), and it is observed that the phase change with the 2DEG conductivity is negligible at the resonant frequency except at very high conductivities. In fact, significant phase change occurs at lower conductivities when the 2DEG pair is placed very close to the metallic FSS (not shown). This effect was explored to realize broadband modulation using field-sensitive detection (e.g. time domain THz spectroscopy) in a metamaterial design where metallic FSS sits right on top of the semiconductor thus the phase change is most sensitive to the conductivity [56].

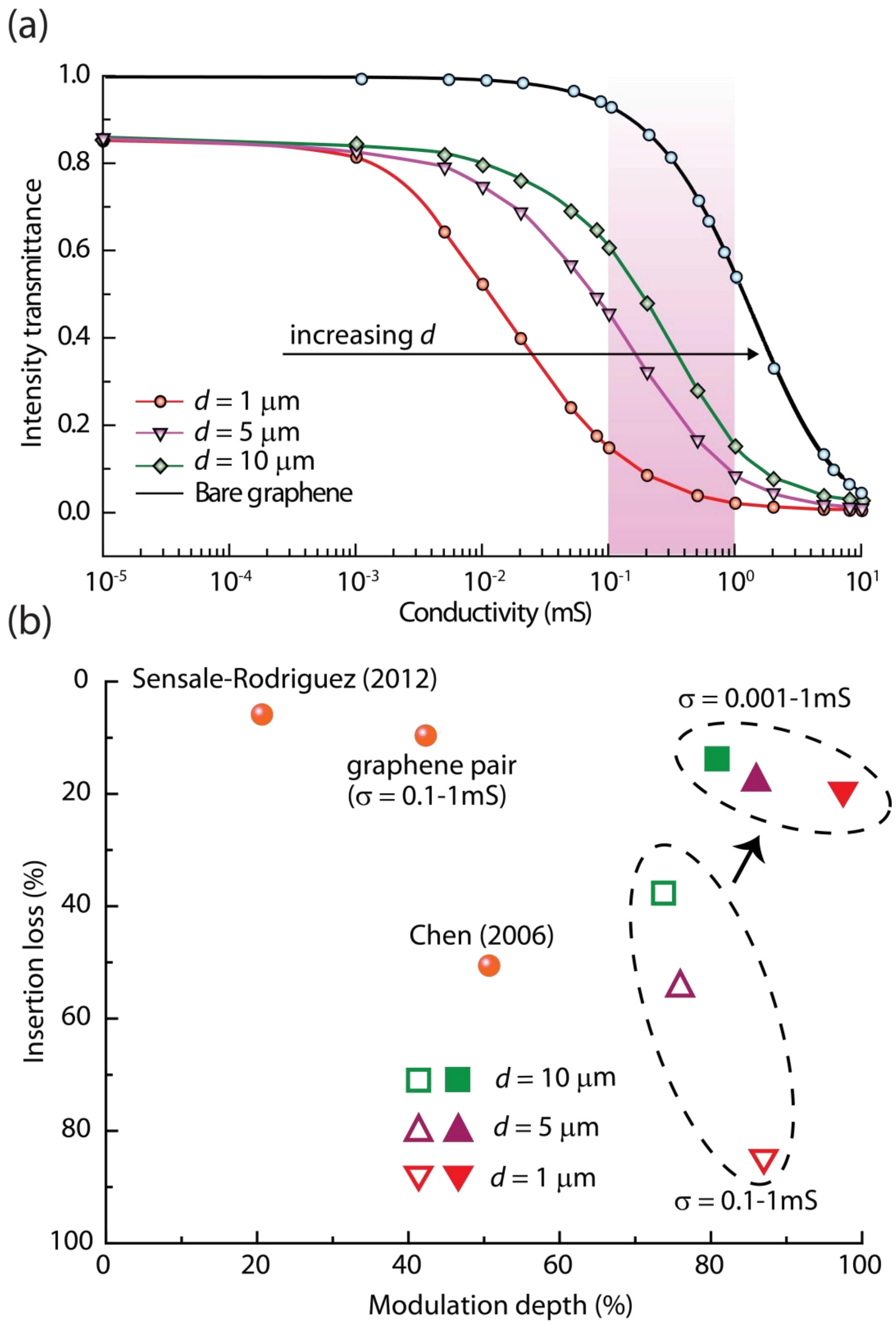

Figure 3.13 (a) Intensity transmittance at the resonant frequency versus the half conductivity of the 2DEG-pair at different separating distance between the pair and metamaterials. The red, pink and green curves correspond to d = 1, 5, 10 μm. The black curve and blue circles points are, respectively, analytical solutions[21] and HFSS simulation results corresponding to the

intensity transmittance through a pair of graphene suspended in air. The pink shaded region shows the typical range of single-layer graphene conductivity. (b) Tradeoffs between insertion loss and modulation depth extracted for two ranges: σ = 0.1-1 mS and 0.001-1mS [30].

In Figure 3.13 (a), the power transmission of the proposed modulator at the resonance frequency as a function of half of the 2DEG-pair conductivity are plotted with varied separating distance d between the FSS and 2DEG-pair. The red, pink and green curves correspond to different placements of the 2DEG-pair, d = 1, 5, 10 μm. The black curve (analytical results) and blue circle points (HFSS simulation results) in Figure 3.13 correspond to the intensity transmission through a pair of graphene suspended in air, which match with each other. This excellent agreement of analytical and HFSS solutions demonstrate the validity of our modeling approach.

For a given 2DEG-pair conductivity, the closer it is placed to the metallic FSS, the lower the intensity transmission due to stronger near-field effects or concentrated field in the 2DEG planes. For a 2DEG-pair conductivity of 2x0.001 mS, the amplitude transmittance reaches near 91%, i.e. an intensity insertion loss of 1 - 0.912 ~ 17%. More careful examination revealed that the finite conductivity of gold (2x10^{-6} Ohm-cm) and the 2DEG-pair results in absorption of 12% and 2%, respectively; and the rest of the intensity insertion loss (3%) is due to the reflection of the metamaterial stemming from the substrate refractive index and thickness. When the 2DEG-pair conductivity increases to 2x5 mS, the amplitude transmission is < 20%; this corresponds to a modulation depth of the amplitude transmission: (91-20)/91 ~78%, or of the intensity transmission: (912-202)/912 ~ 95%. The pink shaded region in Fig. 3(a) marks the typical tunable conductivity range of a single-layer graphene. For d = 10 μm and the typical conductivity tunable range of a single-layer graphene, the resultant intensity modulation depth is about (62-16)/62 ~ 74% with an insertion loss of ~ 38%. The improvement in modulation depth over that achievable by a suspended graphene pair without a field enhancing architecture is appreciable, which is ~ 42%, although the suspended pair offers broadband operation with a lower insertion loss of ~ 9%. When a graphene pair is placed at d = 1 μm, the resultant intensity modulation depth is about (14-2)/14 ~ 86% with an insertion loss of 86%.

A high modulation depth is attractive; however, too close placement is not desirable since it introduces an extremely high insertion loss. The tradeoff between modulation depth and insertion loss is shown in Figure 3.13 (b) for two tunable conductivity ranges: 0.1 – 1 mS and 0.001 – 1 mS. Also shown are two representative transmission-mode experimental results [29, 55], suggesting that superior performance can be achieved with proper choices of the tunable materials. A wide conductivity range with a lower minimum conductivity gives rise to the desired modulation performance: low insertion loss and high modulation depth. Although graphene is promising in constructing the proposed electrically tunable terahertz modulator due to its facile integration with other materials and low cost in large-scale production, its minimum conductivity due to the zero bandgap can introduce an appreciable insertion loss. To further improve the modulator performance, it is necessary to adopt other tunable elements with lower optical conductivities for the terahertz frequency range of interest. In this regard, Si becomes a strong contender among all possible candidates due to its maturity. One can potentially use a thin membrane of Si/SiO_2/Si as the self-gated electron layers. The major advantage of the Si-Si pair is that its conductivity can be tuned to be below 10-5 mS, where absorption by mobile electrons is practically zero. Considering a moderate conductivity range of 10^{-5} - 0.5 mS, one can see from Figure 3.13 (a) that a near unity modulation depth with an insertion loss of < 15% can be obtained. One can also stack multiple tunable elements to enhance modulation depth with a limited range of tunable conductivity as long as they do not introduce excessive insertion loss. It is also conceived that those structures can be readily fabricated employing 2D semiconductor crystals with non-zero bandgap, such as MoS_2 and WS_2, for their easy integration and low minimum conductivity.

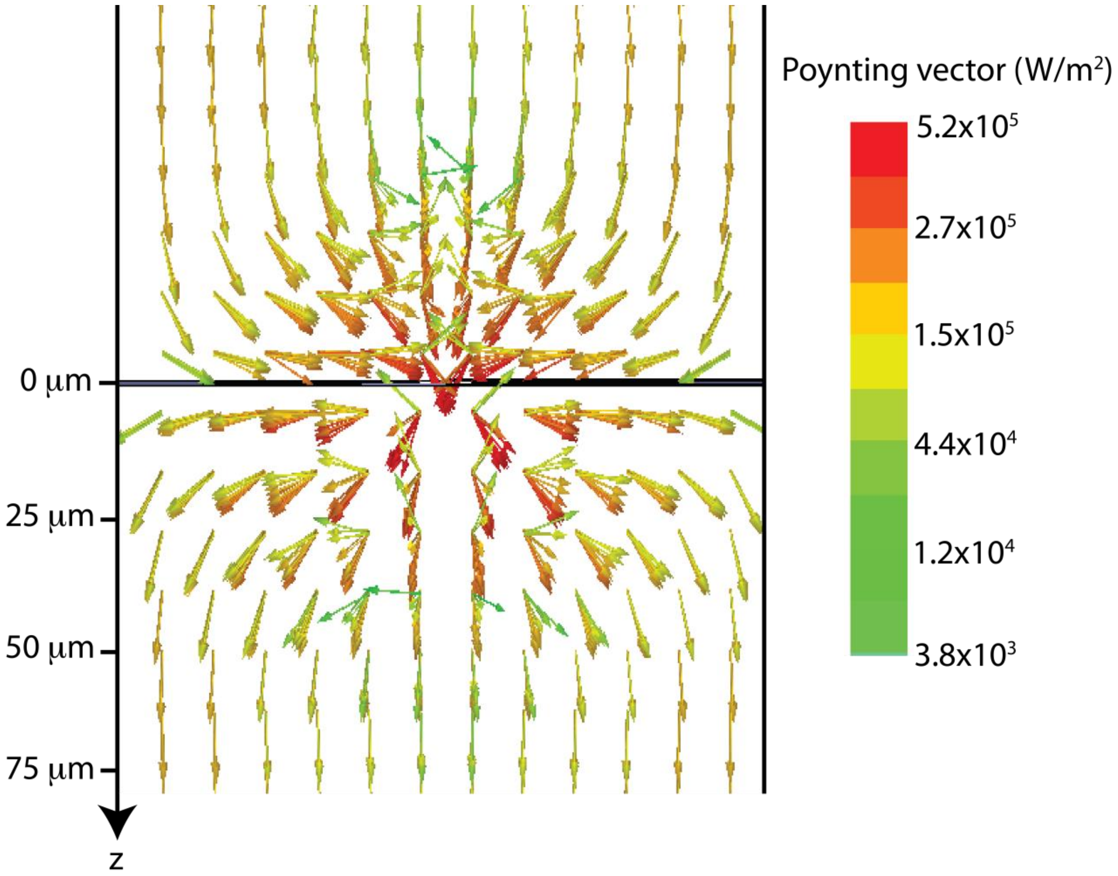

Figure 3.14 Cross sectional Poynting vector distribution near the metallic FSS alone cut along the centerline of the cross. The FSS lies at the z = 0 μm plane. The color and direction of the

arrows indicate the amplitude and propagation direction of the THz wave, respectively.

Indeed, by placing the free carrier layers in a cavity, their absorbance/reflectance at a given conductivity can be augmented. To better understand the physical picture for the enhanced modulation, we plot in Figure 3.14 the Poynting vector distribution in the cross sectional plane of the metallic FSS alone cut along the centerline of the cross. The FSS plane is denoted as z = 0 μm and the incident wave propagates along the +z direction. Near the center of the cross, the magnitude of the Poynting vector distribution is strongest given the electromagnetic wave cannot penetrate gold thus funnel through the cross opening. Far away from the FSS (z > 50 μm), it shows a plane wave propagating along +z direction with rather uniformly distributed intensity. Furthermore, near the metal FSS, the electromagnetic wave largely propagates in the x-y plane, which leads to a dramatically augmented propagation length in the 2DEG layers when it is placed close to the FSS. The combination of enhanced field strength and in-plane propagation length in the near field of the FSS results in enhanced absorption thus exceptional modulation by the 2DEG layers when placed close.

3.4.3 Experimental demonstration and discussions

To confirm the device idea proposed above, we move on conducting some experimental demonstrations [31]. The designed sample has a structure shown in Figure 3.15 (a) (non-patterned graphene) and (b) (patterned graphene), which employs polyimide (PI, PI2600 HDMicrosystem) as freestanding substrate and spacer to separate metamaterial FFS and graphene. The sample was prepared by stacking PI, Al-based FFS, PI spacer, and transferring large-area CVD graphene onto a bare Si substrate.

Finally, the whole structure is peeled off from the Si, forming a free-standing device. By carefully controlling the spin speed, baking time and repetition times of spinning, desirable thickness of PI spacer could be achieved [84]. After spinning, the PI is cured at 300℃ in air. The graphene transfer follows the process described in Appendix A. The FSS structure is patterned by optical lithography, e-beam evaporation and common lift-off process. As a proto-type device, here we passively tune the graphene conductivity by stacking graphene layers. In Figure 3.15 (c) and (d), the optical images of finally resulting sample rolled onto a glass pipette are shown.

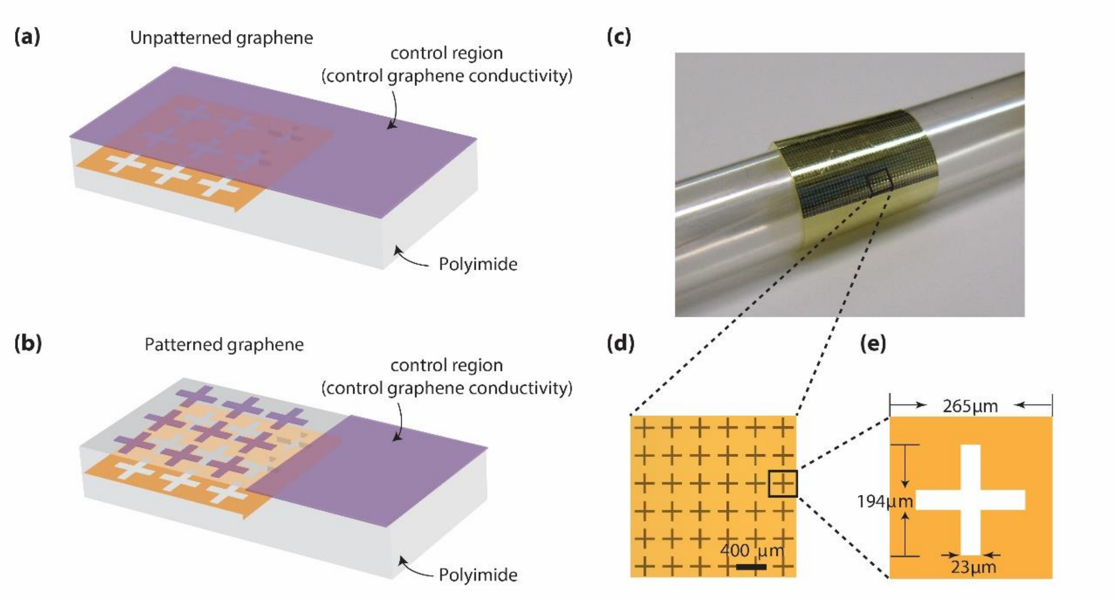

Figure 3.15 Analyzed metamaterial structures. (a) and (b), schematic of the analyzed device structures consisting of a metallic FSS embedded in a polyimide (PI) film with non-patterned and patterned graphene layers on top. The right half of the sample (control region), which contains un-patterned graphene in top of PI, is used to monitor the conductivity of graphene. (c) Optical image of a fabricated THz modulator on flexible PI substrate rolled on a glass pipette. (d) Optical image showing a detail of the FSS structure. (e) Sketch showing the dimensions of the FSS unit cell.

The THz transmission through the devices is measured by a Menlo TERA K-15 time-domain spectroscopy (TDS). To determine the electrical conductivity of graphene on each sample, we keep half of graphene film as reference area where there is no FSS beneath. In this way, we could extract the DC conductivity of graphene and scattering time by fitting measured THz transmission with Drude mode. This method of determining graphene conductivity is already discussed in 3.1. The transmission of graphene (T) normalized to the bare substrate without graphene (T_0) is [66]

$$\frac{T}{T_0} = \frac{1}{\left|1 + \frac{\sigma(\omega) Z_0}{1 + n_s}\right|^2} \qquad 3.6$$

where n_s is substrate refractive index and the conductivity $\sigma(\omega)$ follow Drude mode:

$$\sigma(\omega) = \frac{\sigma_{DC}}{1 + \omega^2 \tau^2} \qquad 3.7$$

where τ is carrier relaxation time. Note that we have only taken the real part of optical conductivity into consideration here because the amplitude reduction (absorption) only relates to that part. The measured and fitted normalized transmission are shown in Figure 3.16, where DC conductivities and carrier scattering time for 1-, 2-, 3-layer graphene are shown in Table 3.1. The extracted values are later used in HFSS simulations to compare with the experimental results.

Graphene layer	σ_{DC}(mS)	τ (fs)
1	0.73±0.05	75±5
2	1.32±0.06	98±3
3	1.98±0.08	121±3

Table 3.1 Extracted graphene DC conductivity and carrier scattering time

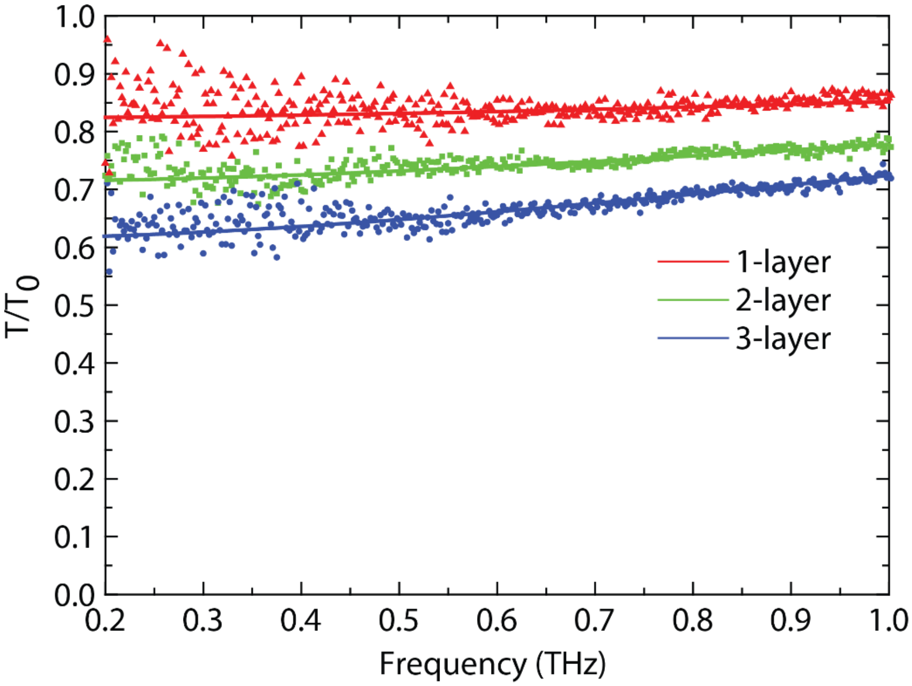

Figure 3.16 Normalized THz transmission (T/T_0) of 1-, 2-, 3-layer graphene as a function of frequency. Symbols are measured results and lines are fittings from Eqs 3.6 and 3.7.

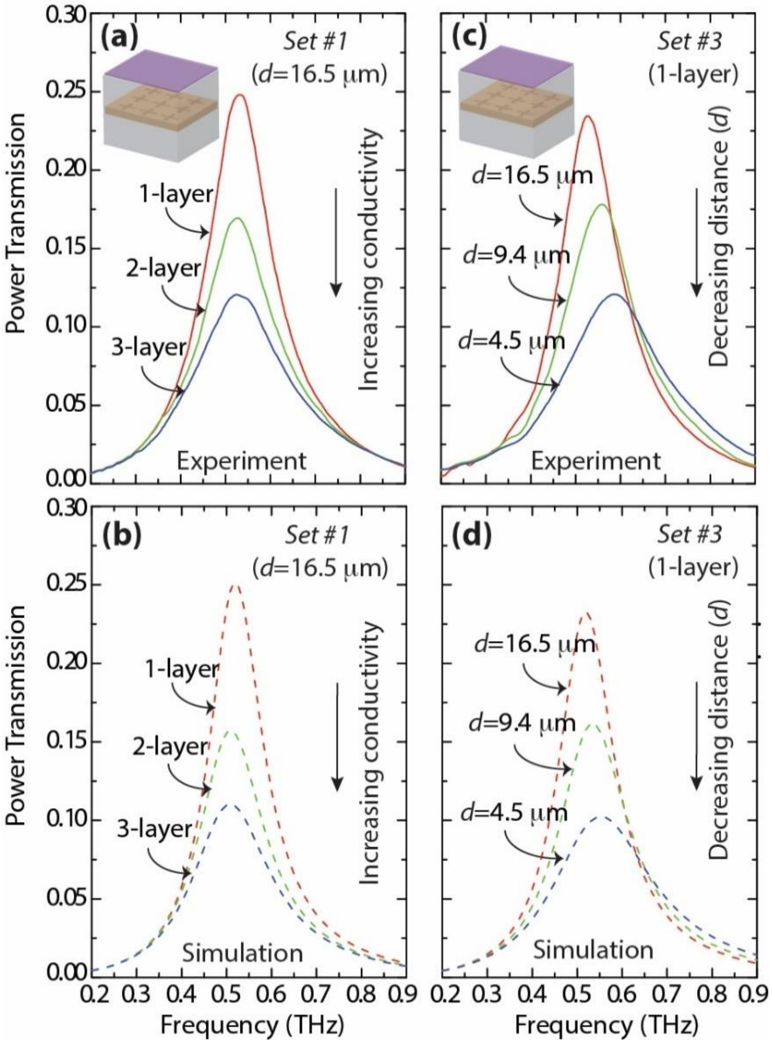

Figure 3.17 (a) and (b), experimentally measured (a) and simulated (b) intensity transmission spectra for devices containing 1-, 2-, and 3-layers of graphene (sample Set #1), and d=16.5 μm. (c) and (d), experimentally measured (c) and simulated (d) intensity transmission spectra for devices with 1-layer of graphene and various PI spacer thicknesses, d=16.5, 9.4, and 4.5 μm, respectively (sample Set #3).

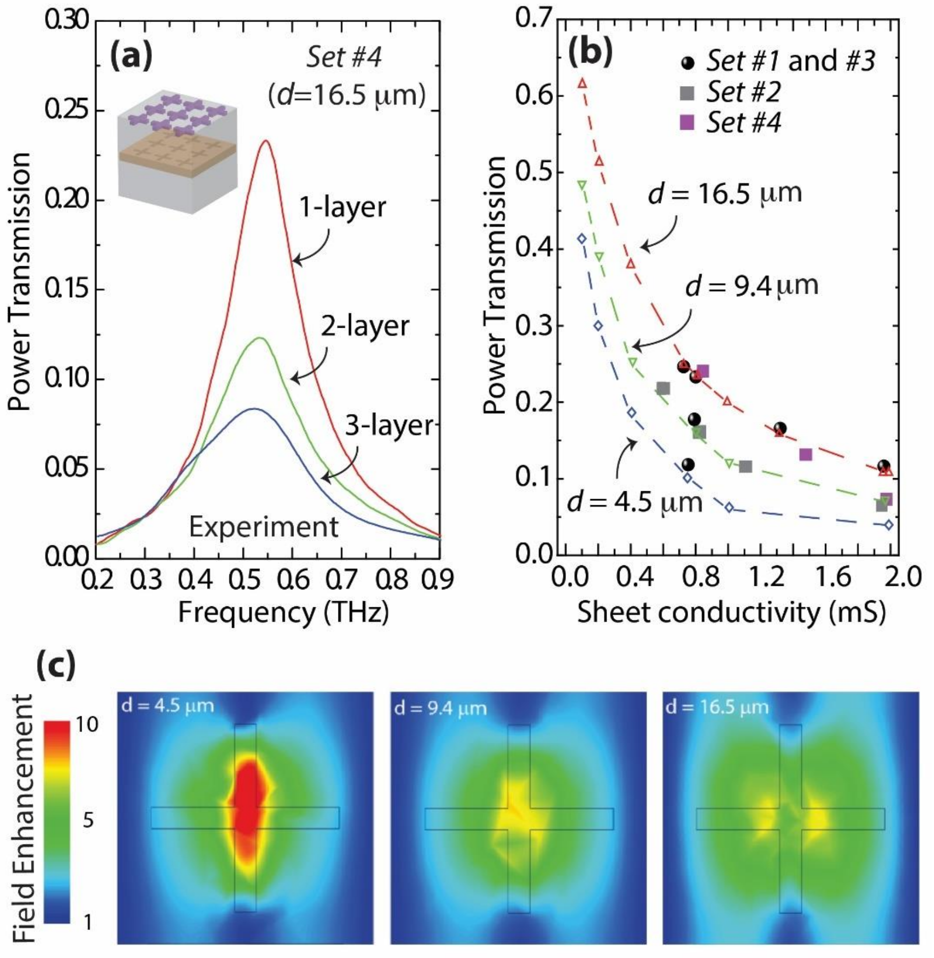

Figure 3.18 **(a)** Measured power transmission spectra for devices with 1, 2, and 3 layers of patterned graphene (*sample Set #4*). The graphene layers have been patterned to the complimentary structure of that of the metallic FSS underneath. **(b)** Summary of the measured and simulated THz transmission (at resonance) as a function of graphene sheet conductivity for all the analyzed sample sets. The measured (solid symbols defining dashed traces) and simulated (hollow symbols) THz power transmission values are plotted for three different thicknesses of the dielectric spacer (*d* = 16.5, 9.4, and 4.5 μm, respectively). The black solid circles represent experimental results obtained by stacking 1, 2, and 3 graphene layers (*sample Set #1* and *sample Set #3*), whereas the grey solid squares represent results for devices containing single layer graphene where the conductivity was tuned by means of chemical doping by HNO_3 (*sample Set #2*). The purple squares represent measurements on samples with patterned graphene (*Sample Set*

#4). **(c)** Simulated electric filed enhancement distribution inside the plane of the graphene for different values of d. It could be clearly seen that enhancement gets smaller when graphene gets farther away from the FSS plane, which is consistent with the decrease of fitting parameter α_1 as d is increased.

Throughout our work, the conductivity of graphene layers in each sample has been individually monitored by employing the above-mentioned method; these values are subsequently used in our modeling section. The measured and simulated THz power transmission spectra for the graphene/FSS hybrid structures with 1-, 2-, 3-layers of graphene (*sample Set #1*) are shown in Figure 3.17 (a) and (b), respectively. The thickness of the spacer between the graphene layers and the FSS is kept to d=16.5 μm, which ensures the same electric field strength with an identical enhancement factor at the graphene plane. The geometry and dimensions of the FSS determine the shape of center-band transmission, which in this case holds a resonance at around 0.5 THz and an intrinsic peak power transmission which can be as high as 85% (simulated) (~ 15% absorption by the metal) [83]. On the other hand, the total conductivity of the modulation medium (graphene) sets the transmission magnitude over the entire spectrum. In our experiments the intrinsic peak power transmission through FSS is measured to be ~80% (for d = 16.5 μm) to 85% (for d = 4.5 μm). For the case pictured in Figure 3.17 (a), which corresponds to d = 16.5 μm, it is remarkable that the presence of only one layer of graphene can reduce the maximum transmission from 80% to 25%, corresponding to a fractional variation of (80-25)/80 = 69%. With increasing graphene conductivity (by means of adding more graphene layers), the THz transmission is further reduced from 25% to 17% (2-layer graphene) and then to 12% (3-layer graphene). The reduction in transmission is attributed to boosted absorption by graphene, which can reach a maximum of 50% of the incoming power, as well as increasing reflection (~50% at the absorption maximum) from the sample [30]. In this case, when the graphene sheet conductivity is varied by three times, i.e. from that in 1-layer graphene to that in 3-layer graphene, the fractional decrease in the transmitted power is more than 50%, i.e. (25-12)/25 = 52%. The above observed high-conductivity induced low transmission phenomenon is consistent with what has been reported in previous work [85]. Again, note that the total conductivity is the sum of the conductivities of the individual graphene layers, which is not surprising considering the fact that the thickness of the overall graphene stacks (less than 2 nm) is negligible compared to the wavelength of the incident THz waves. Our numerical simulations of transmission, employing the sheet conductivity values measured in the control region for each sample, exhibit an excellent agreement with the experimental results.

We also studied samples where the graphene conductivity was varied through chemical doping (*sample Set #2*). Since HNO_3 is well known to be a *p-type* dopant for graphitic materials such as carbon nanotubes, graphene, etc. [75, 86], in this work the chemical doping was realized by immersing a single-layer graphene covered sample ($d = 9.4$ μm) in a HNO_3 solution (63 wt%) for 1-5 minutes, followed by a dry and baking step at 85℃. A series of THz transmission spectra (Fig. S4) through the test and control regions of the sample were measured before chemical immersion (σ_{dc}~0.65 mS), immediately after doping (σ_{dc}~1.96 mS), after 12 hours in air (σ_{dc}~1.10 mS), and after 24 hours (σ_{dc}~0.81 mS) in air. The decrease of sheet conductivity is a result of de-doping process in air, that is, the removal of physically adsorbed HNO_3 molecules on the graphene surface. The measured THz transmission through the test region of the samples at resonance is plotted in Figure 3.18 (b) (grey squares). Similar behavior is observed when the graphene conductivity is increased due to chemical doping; in both cases the THz transmission drops as the overall graphene conductivity increases. The dashed curves with hollow symbols in Figure 3.18 (b) represent the simulated peak THz transmission as a function of the graphene sheet conductivity and each of these curves is associated with structures having different values of *d*. The values of measured transmission at resonance for this chemically doped sample (grey squares) in Figure 3.18 (b) show good consistency with the simulations (dotted curves) as well as with our measurements on multilayer-graphene samples (black circles). This also helps confirm that stacking of multiple graphene layers behaves similarly to doping of a single layer of graphene in terms of electromagnetic wave transmission.

Beyond this, for the first time with experiments we systematically investigated the impact of the distance between the graphene layers and the FSS on the THz transmission through the structure. In Figure 3.17 (c) and (d), measured and simulated THz transmission through three samples (*sample Set #3*), all with single layer graphene, but with different spacer thickness *d* = 16.5, 9.4, and 4.5 μm, is shown. As the graphene layer is placed closer to the FSS, the THz transmission declines from 23% to 12% and the resonance frequency blue-shifts from 0.53 to 0.58 THz, even though the graphene conductivity was maintained constant, i.e. the extracted sheet conductivity from the control region was the same, in all three samples. This transmission reduction is clear evidence that the interaction between the FSS and graphene strongly depends on the separation distance between them. The light-matter interaction is enhanced when graphene is closer to the FSS, leading to lower transmission, as expected by our previous theory [30]. In Figure 3.18 (c) we show the electric field intensity distribution at the graphene plane when the metallic FSS is placed at different distances above it; it can be clearly noticed that the electric field is greatly augmented in a region within tens of microns away from the FSS. It is compelling to acquire this source of control for the interaction strength by changing the location of the modulation medium. This location can be strategically chosen to realize high MD with simultaneous low IL based on the conductivity swing ranges of specific materials, i.e. not only limited to graphene. The observed frequency blue-shift of the resonance peak is primarily due to the varied sample total thickness t ($t \sim d + t_{sub}$), therefore different effective dielectric environment, where t_{sub} is the thickness of the PI substrate, which is kept as 2.2 μm in all these three analyzed samples. Considering the fact that the electric field enhancement near the FSS can reach regions as far as tens of microns in z-direction, a change in PI thickness can indeed translate into a different effective dielectric environment. Thinner samples could be modeled with lower effective dielectric constant, thus higher resonant frequency (ω_r), which will be discussed in more details in the modeling section.

One critical challenge in reported voltage-actuated graphene-based THz wave modulators is their low operation speed, which is severely limited by the large area of the employed modulation medium as well as the large THz beam size [85]. Integration with a FSS, as in our proposed design, could potentially tackle this problem by reducing the active area of the device (area occupied by graphene). In the near field, the electric field is highly confined at the openings of the FSS while negligible elsewhere.

Consequently, we expect that the device active area (graphene) can be reduced to the FSS openings only, which effectively form a complimentary pattern to that of the FSS. To demonstrate this principle, we fabricated samples with patterned graphene structures, as shown in the inset of Figure 3.18 (a). The graphene layers were patterned using oxygen plasma to a geometry consisting of the complementary structure to the underlying FSS. Photolithography was employed to define the graphene pattern, which was aligned directly on top of the openings of the metallic FSS. The measured THz transmission for samples with 1-, 2-, and 3-layers of graphene and d=16.5 μm (*sample Set #4*) is shown in Figure 3.18 (a). Similar to what was previously discussed in samples containing un-patterned graphene, a peak THz transmission ranging from 24% to 8% is observed when the total graphene sheet conductivity is varied from 0.8 to 2 mS. However, the total graphene area in these samples is reduced by around 90%. It is noted that the fractional decrease of the transmitted power slightly increased from 52% to (24-8)/24 = 66% after the graphene layers were patterned, which is partially caused by a higher conductivity in our patterned samples. Compared to previous reports on graphene based THz modulators[29, 30, 73, 87-90], this work is the first experimental demonstration of the intrinsic geometrical designs tradeoffs in graphene/FSS hybrid modulator systems.

We could estimate the potential operation speed of an electrically actuated hybrid device structure enabled by self-gated graphene sheets separated by a 100 nm SiO_2 (or other dielectric like SiN_x, PMMA etc.) dielectric as proposed and discussed in the other work [30], which is primarily limited by the RC time constant ($R_{grapene}C_{ox}$) in this device structure. If the THz beam size is 1x1 mm^2, the number of FSS units that are need to control the light is N=$1^2/0.265^2$ with 0.265 mm being the FSS unit dimension. The capacitance associated with this geometry is $C_{ox} = \epsilon_r \epsilon_0 A/t_0$ where ϵ_r=3.9 and ϵ_0=8.85x10^{-12} F/m are the relative permittivity of SiO_2 and the vacuum permittivity, respectively, and $A = N * A_{FSS}$ is the total area occupied by active graphene. If the metal contacts are made to all the edges of graphene cross-slots, the resistance ($R_{graphene}$) could be estimated by $1/\sigma_{graphene} W/L$~60 Ω for $\sigma_{graphene} = 2$ mS. This resistance could be further reduced by doping, but this can degrade the tradeoffs with insertion loss as well as modulation depth. Therefore, the operation speed is given as $1/2\pi R_{graphene} C_{ox}$~0.3 GHz, which is boosted by a factor of $\frac{L}{W}\frac{A_{beam}}{A}$ ~ 70 times when compared to the case of devices consisting of un-patterned graphene. The contact resistance R_c between metal and graphene is estimated to be 4 Ω assuming a specific R_c = 100 Ω-μm and a graphene cross stripe width W=23 μm, which is small compared to resistance of graphene stripe itself (~60 Ω) thus negligible in the operation speed estimation. In Figure 3.18 (b), all the measured transmission values (solid symbols) at resonance as a function of sheet conductivity, together with simulation results (open symbols) are summarized. Instructively, both the graphene conductivity and the distance *d* between the FSS and the graphene layers determine the THz transmission. The graphene conductivity affects the transmission because of intraband absorption, but *d* also affects the transmission through modifying the strength of light-matter interaction in graphene. The first parameter, graphene conductivity, can provide active modulation, whereas the latter, *d*, could be chosen to achieve the best tradeoff between MD and IL for specific material systems based on their conductivity swing ranges.

CHAPTER 4: THERMAL DYNAMICS OF MOS$_2$ STUDIED BY RAMAN SPECTROSCOPY

Raman spectroscopy has been shown a powerful tool for studying properties of nanomaterials in recent years [39, 91-97]. It could not only be used to identify the layer number [91, 98], but also monitor a variety of external effects on the electrical properties and phonon dispersions of 2D crystals [39, 99]. Beyond that, Balandin et al [100, 101] and Cai et al [102, 103] have shown that Raman spectroscopy could be applied to investigate the thermal transport of graphene films. In this chapter, we will primarily focus on exploration of thermal properties of MoS$_2$ through Raman spectroscopy.

4.1 Thermal dynamics probed by Raman spectroscopy

Raman spectroscopy is a widely used spectroscopic technique to investigate the vibrational, rotational and other low-frequency modes in a system [104]. The incident photon interacts with molecular vibrations, phonons or other excitations in the material, leading to the energy shift of scattered photons (inelastic scattering). The amount of this energy discrepancy provides information about phonon vibration etc. Usually, the light scattered from an illuminated sample is collected using specifically designed optics and then sent into a monochromator to differentiate the components of photons by wavelength. The scattered light contains photons due to both elastics and inelastic scattering, where the inelastic scattering (Raman scattering) is usually much weaker than the other. After filtering out the elastic Rayleigh scattering components, the rest of the collected light is dispersed onto a detector. Thus, the resulting spectrum obtained exhibits the information of Raman scattering in the material.

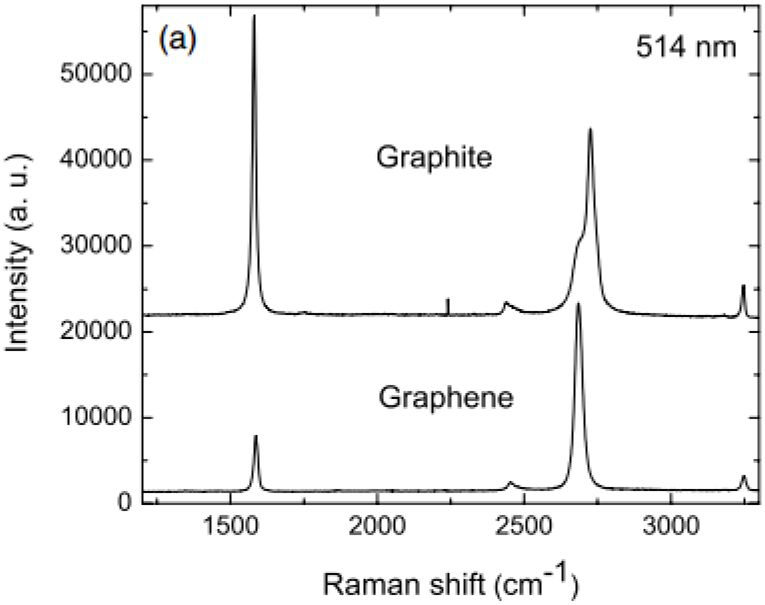

Figure 4.1 Representative Raman spectra of graphite and graphene layers

In the field of graphene research, people have regarded Raman spectra as critical references to characterize graphene layer number, quality and effects from external perturbations such as electric/magnetic field, strain, doping, disorder and functional groups [105]. A typical Raman spectrum of graphene is shown in Figure 4.1, where three most intensive peaks due to in-place vibrations are observed: D, G and G' (or 2D). The present of D peak is used as evidence of defects in graphene. The G peak is due to the doubly degenerate zone center E_{2g} mode and the G' peak is the second order of zone-boundary phonons [39].

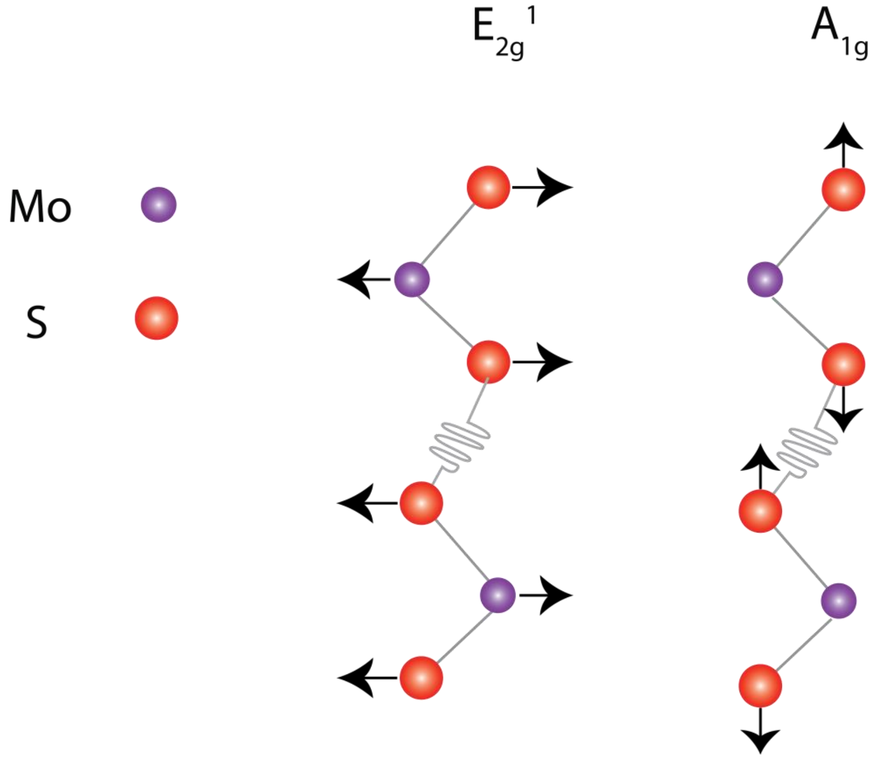

Figure 4.2 Raman-active phonon vibrational modes of MoS_2.

Beyond that, Raman study of thin flakes of TMDs is also attractive [91]. The Raman spectrum of MoS_2 consists of two prominent peaks: in-plane E_{2g}^1 and out-of-plane A_{1g} modes, as shown in Figure 4.2. For the bulk MoS_2, E_{2g}^1 peak locates around 383 cm^{-1} and A_{1g} is around 409 cm^{-1}. With the decreasing layer number, the A_{1g} peak softens due to the reduction of interlayer Van der Waals interactions thus the effective restoring forces [91]. Anomalously, the E_{2g}^1 mode has been found stiffening as thinning of the flakes, which might be caused by a weaker dielectric screening of long-range interactions between the effects charges in thinner samples. Similar behavior is also observed in Raman spectrum of WS_2 for the same reason [106]. As a result, the wave number difference between these two Raman peaks is a reliable indicator of the thickness for the samples thinner than 6 layers.

4.2 Temperature and laser power dependent Raman spectra of monolayer MoS$_2$

Due to anharmonic lattice vibrations, the Raman spectrum of crystals is sensitive to variation of temperature. In the section, we present a detailed temperature and laser power dependent Raman study of *suspended* and supported monolayer MoS$_2$. Such studies are of fundamental importance for a comprehensive understanding of anharmonic lattice vibrations, thermal expansion, and thermal conductivity [107-111]. Our temperature-dependent Raman study potentially provides a powerful, noncontact method to monitor the local temperature rise induced by light, electrical currents, etc.

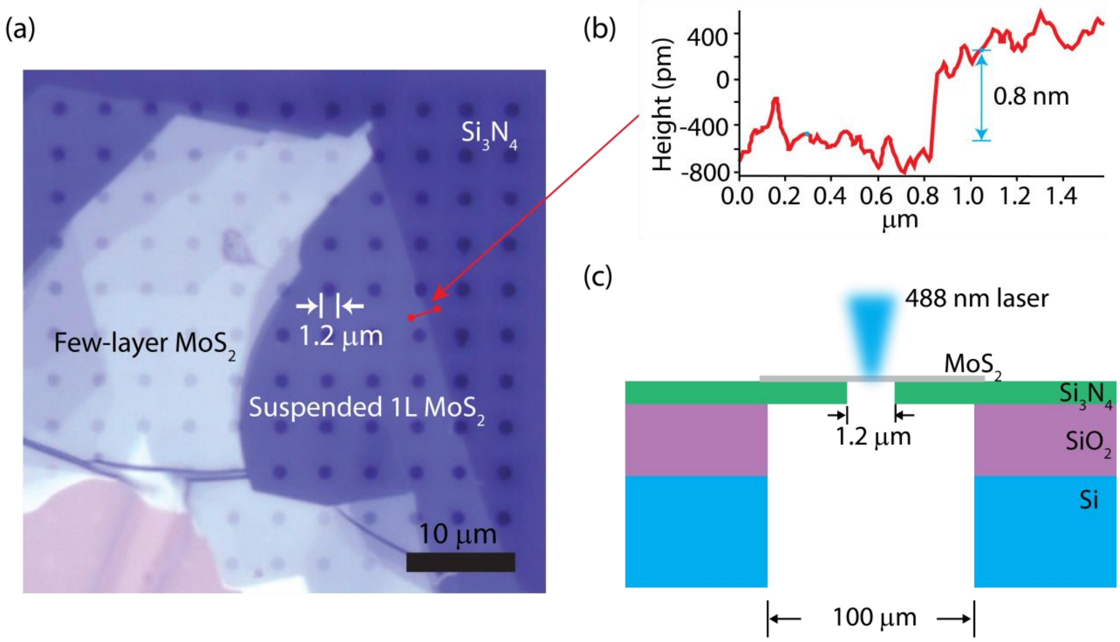

Figure 4.3 (a) Optical micrograph of exfoliated MoS$_2$ flakes placed on Si$_3$N$_4$/SiO$_2$/Si perforated grid. (b) AFM step height across the edge of the monolayer MoS$_2$flake prior to being transferred to the final substrate. (c) Sketch of monolayer MoS$_2$

on $Si_3N_4/SiO_2/Si$ substrate. Here MoS_2 over the holes in the 20
nm thick Si_3N_4 is suspended.

The ultrathin MoS_2 films were prepared by colleagues at Swiss Federal Institute of Technology in Lausanne. The optical micrograph of suspended monolayer MoS_2 over a 20 nm thick, perforated Si_3N_4 grid is shown in Figure 4.3 (a). Flakes of MoS_2 were first deposited onto a SiO_2/Si wafers using mechanical exfoliation from bulk crystals of molybdenite (SPI). Following the identification of the layer number using optical microscopy and atomic force microscope (AFM), the corresponding flakes are transferred onto $Si_3N_4/SiO_2/Si$ substrate. The height profile measured by AFM at the edge of the flake on rough PMMA/PVA surface before the transfer process, presented in Figure 4.3 (b), shows a thickness of ~0.8 nm with a root mean square roughness larger than 0.3 nm, confirming that the region of interest is indeed monolayer MoS_2. The cross-section of the $Si_3N_4/SiO_2/Si$ substrate structure is shown in Figure 4.3 (c), where holes with a diameter of 1.2 μm are defined by e-beam lithography and patterned by an etching process on Si_3N_4. The suspended monolayer MoS_2 flake is obtained on top of the holes in 20 nm-thick Si_3N_4.

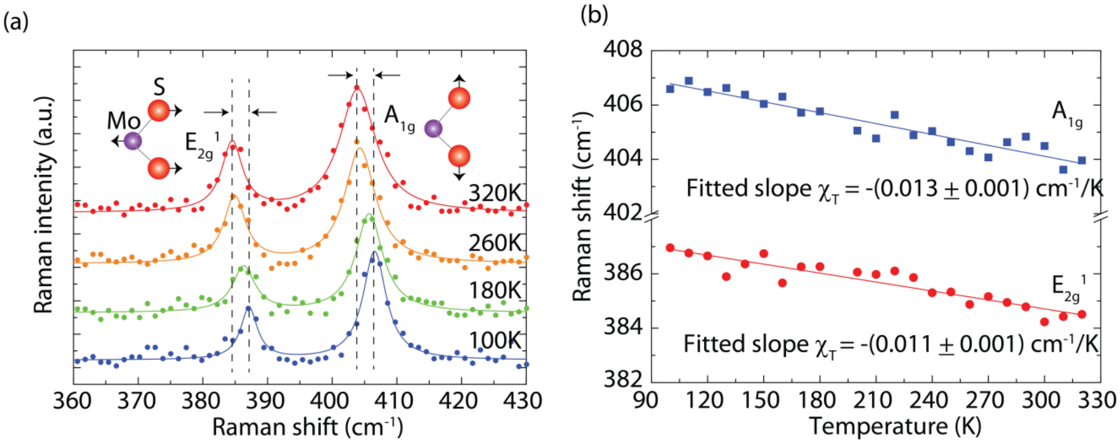

Figure 4.4 (a) Four example Raman spectra of suspended, monolayer MoS$_2$ collected at 100 K, 180 K, 260 K, and 320 K. Spectra offset vertically for clarity. (b) Raman peak frequencies of both A$_{1g}$ (blue squares) and E$_{2g}^1$ (red circles) modes as a function of temperature. Fit lines and resulting linear temperature coefficients χ_T for both modes are shown.

The temperature-dependent Raman measurements were collected using a Renishaw In-Via micro-Raman spectrometer employing an excitation laser with wavelength of 514.5 nm. A long-working distance 50X objective lens (numerical aperture NA=0.55) provides a Gaussian beam width estimated to be $2\lambda_0/\pi NA \approx 0.6\ \mu m$ [102, 103]. The samples were mounted in a cryostat cooled by liquid nitrogen. Throughout all of the temperature-dependent measurements, the laser power is maintained to be less than 0.14 mW.

Figure 4.4 (a) shows four example Raman spectra and their corresponding Lorentzian fits collected from suspended monolayer MoS$_2$ while the cryostat temperature ranges from 100 K to 320 K. As seen in the figure, two prominent peaks around 385 cm-1 and 405 cm-1 are observed, which correspond to the in-plane E$_{2g}^1$ mode and the out-of-plane A$_{1g}$ mode, respectively. As the temperature increases, both of the Raman-active modes soften linearly and the A_{1g} peak clearly broadens. Figure 4.4 (b) shows the temperature dependence of the Lorentzian fitted peak frequencies from 100 K to 320 K for the A_{1g} (blue squares) and E_{2g}^1 (red circles) phonons. The evolution of the Raman peak position ω (in unit of cm-1) as a function of lattice temperature follows a linear dependence

$$\begin{aligned} \Delta\omega = \omega(T_2) - \omega(T_1) &= \chi_T(T_2 - T_1) \\ &= \chi_T \Delta T \end{aligned} \quad 4.1$$

where χ_T , the slope of temperature dependence, is the first-order temperature coefficient for the respective modes, and T is the absolute temperature. Nonlinear coefficients are not considered here given that they can only be observed at higher temperatures. It is worth noting that we observed nonlinear dependence in our laser power measurements at room temperature, which will be discussed later in this paper. The extracted linear temperature coefficients χ_T from the slopes are -(0.011 $\pm$ 0.001) cm-1/K and -(0.013$\pm$0.001) cm-1/K for the E_{2g}^1 and A_{1g} modes, respectively.

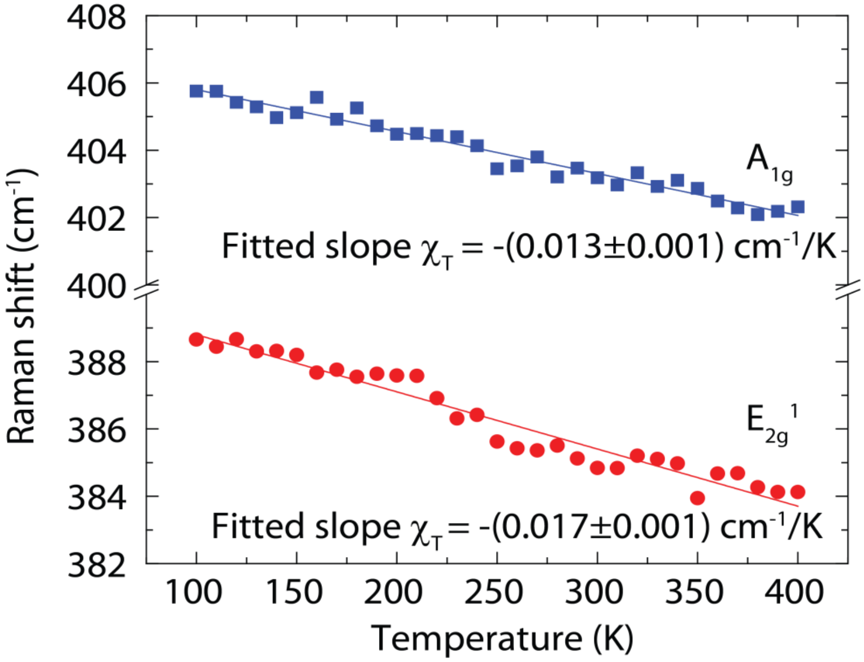

Figure 4.5 Temperature dependent Raman peak positions of E_{2g}^1 and A_{1g} modes in the temperature range of 100-400 K for sapphire-supported single layer MoS_2. Temperature coefficients from linear fits are shown.

The observed linear evolution of phonon frequencies in monolayer MoS_2 can be attributed to the anharmonic vibrations of the lattice [107], which mainly includes contributions from the lattice thermal expansion due to the anharmonicity interatomic interaction. As the lattice expands or contracts due to temperature change, the equilibrium positions of atoms and consequently the interatomic forces change, which induces shifts in the phonon energies [112]. This linear behavior of Raman peak frequencies with temperature is seen in many materials within a certain temperature range [108, 109, 113]. For comparison, we performed similar temperature-dependent Raman measurements on sapphire-supported monolayer MoS_2 as shown in Figure 4.5 and found no significant difference in the first-order temperature coefficients for either mode. The small difference between χ_T coefficients for the E_{2g}^1 mode in suspended versus sapphire-supported likely results from varied in-plane strain applied by the substrate since E_{2g}^1 mode is prone to strain in MoS_2 while A_{1g} is not [114]. Therefore, the temperature-dependent phonon frequency shift determined in this study can be used to monitor local temperature evolution in the MoS_2 nanostructure by recording the change of A_{1g} peak under various external modifications.

In Raman study, the local temperature rise induced by the excitation laser, may lead to an inaccurate determination of Raman peak position. Such effects are extremely critical for material with low thermal conductivity. Therefore, it is necessary to evaluate the effects of laser power on Raman spectrum. For monolayer MoS_2 substrate, strong thermal effects were found [99, 115]. Moreover, it is likely that the substrate plays an important role in heat dissipation; thus the behavior of substrate supported sample might not be intrinsic to MoS_2. To obtain a comprehensive understanding of the intrinsic MoS_2 property, we also studied the laser power-dependent Raman spectra on suspended flake. These Raman spectra are collected in a WITec Raman spectrometer using a 488 nm solid state laser for excitation with the beam focused by a 100X objective lens (NA = 0.9). The estimated Gaussian beam width are approximately 0.34 µm, respectively. Here the Raman system with the high NA is used to ensure the laser beam is much smaller than the hole diameter. Detailed analysis (shown in the later section) confirms that the size of the holes is sufficient to allow for extraction of the monolayer MoS_2 thermal conductivity with high accuracy, though its diameter is about twice larger than the laser beam spot size. This is because of the low thermal conductivity of monolayer

MoS_2. On the other hand, to measure flakes with high thermal conductivity such as graphene or BN, it is necessary to employ much larger holes.

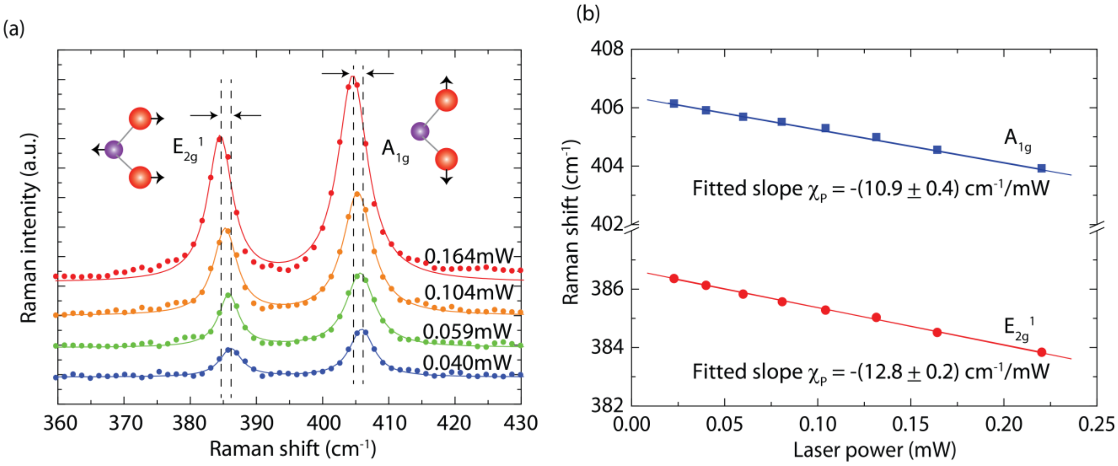

Figure 4.6 (a) Four example Raman spectra of suspended, monolayer MoS_2 at increasing excitation laser power at RT in air environment. Spectra offset vertically for clarity. (b) Raman peak frequencies for A_{1g} (blue squares) and E_{2g}^1 (red circles) modes as a function of laser power. Fit lines and resulting linear power coefficients χ_P are shown.

Four representative room-temperature Raman spectra collected at laser powers spanning form 0.040 mW to 0.164 mW are shown in Figure 4.6 (a). As the laser power increases, both Raman-active modes soften due to local heating of the suspended monolayer MoS_2. To avoid damage to the sample and to stay within the linear dependence range, we kept the excitation laser power below 0.25 mW. The Lorentzian-fit Raman peak frequencies as a function of incident laser power are plotted in Figure 4.6 (b), where both the E_{2g}^1 and A_{1g} modes soften linearly with increasing power. Beyond 0.25 mW of laser power, this thermal behavior saturates as depicted in Figure 4.7. The appearance of non-linear effects results either from the non-linearity of absorption or higher orders of the temperature-dependent coefficients. In Figure 4.6 (b), we show the power-dependent peak positions in the linear, low-power range, which is characterized by

$$\begin{aligned}\Delta\omega = \omega(P_1) - \omega(P_2) &= \chi_P(P_1 - P_2) \\ &= \chi_P \Delta P\end{aligned} \qquad 4.2$$

Here χ_P, the slope of power dependence in the linear region, is the first-order power dependent coefficient and P is the laser power. As with χ_T, the fitted coefficients χ_P for the E_{2g}^1 and A_{1g} modes are very similar, -(12.8±0.2) cm-1/mW and -(10.9±0.4) cm-1/mW, respectively. Note that these P values significantly exceed those for sapphire-supported monolayer MoS_2 (Figure 4.8) and exceed by a factor of two those for suspended few-layer flakes [116].

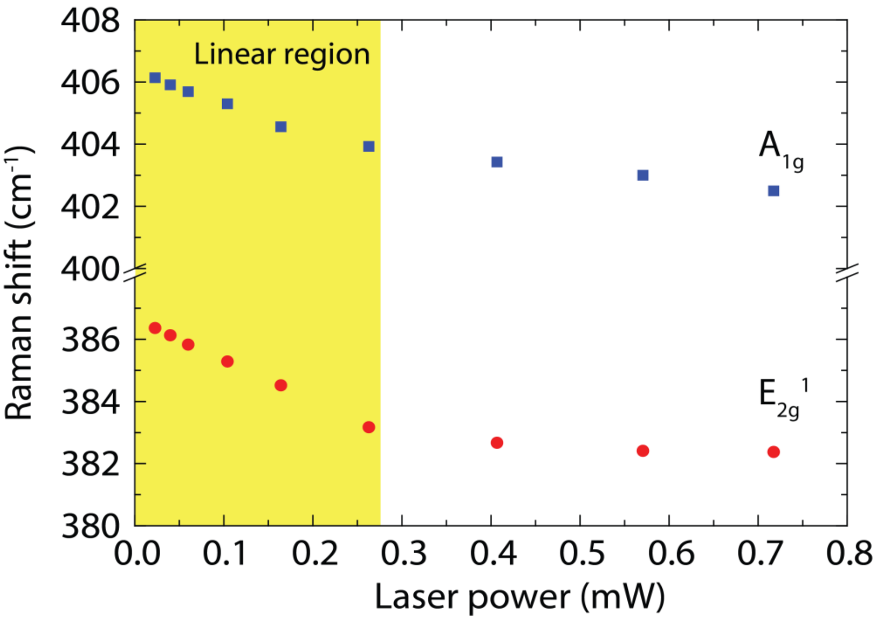

Figure 4.7 The Raman peak frequencies of E_{2g}^1 and A_{1g} modes for laser power up to 0.72 mW for the suspended monolayer MoS_2 flake. Nonlinearity in the Raman peak position occurs above approximately 0.3 mW, beyond the linear region shown in yellow.

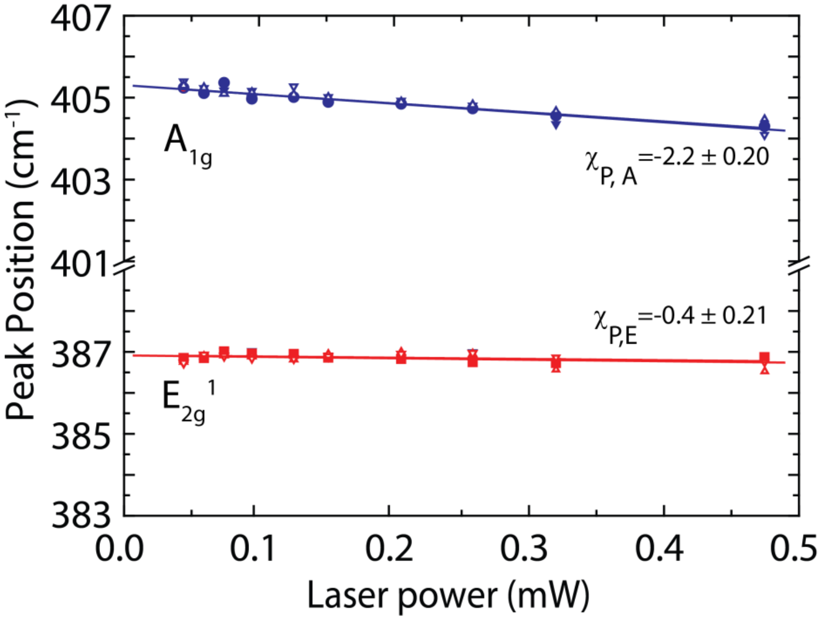

Figure 4.8 Raman peak positions of A_{1g} and E_{2g}^{1} modes at different excitation powers. Different types of markers represent peak positions extracted on different flakes. χ_A and χ_E are respectively the slope of linear fitting for A_{1g} and E_{2g}^{1} peaks (cm^{-1}/mW).

For comparison, Figure 4.8 shows the power dependent Raman peak positions for sample supported on sapphire. Note that, different from suspended flake whose both modes behave very similarly, for the sapphire-supported monolayer flake, the in-plane E_{2g}^{1} mode shows much smaller laser power dependence compared to the out-of-plane A_{1g} mode. This is a strong manifestation of strain in MoS_2. Strain is induced since the expansion of the MoS_2 lattice due to laser heating is hindered by the cooler sapphire substrate (near RT, by assuming negligible absorption of the laser by the substrate). This point is further supported by a recent study on strain-dependent Raman spectra of monolayer MoS_2 where only the E_{2g}^{1} mode is sensitive to the strain variation, but the A_{1g} mode does not respond [114].

4.3 Thermal conductivity of suspended monolayer MoS_2 obtained from Raman spectrum

Taking advantage of the sensitive response of phonon frequency in MoS_2 to local heating by the laser, we are able to estimate the thermal conductivity of this 2D material in a noncontact method. Although the Raman-active optical phonons do not play a significant role in directly conducting heat along the flake, their frequency of vibration is reasonably sensitive to the local temperature fluctuations caused by external effects. The temperature increase of the suspended flake under laser excitation is directly related to the thermal conductivity of the material, assuming that the absorbed heat transfers radially through a small cross-sectional area of the monolayer flake from the center to the edge. The cross section of the substrate and schematic of heat flow is shown in Figure 4.9 (a). Therefore, inside the hole region, we can write the heat dissipation equation ignoring the heat conducted to the air as

$$\kappa \frac{1}{r}\frac{d}{dr}\left[r\frac{dT_1(r)}{dr}\right] + q(r) = 0 \qquad \text{for } r < R \tag{4.3}$$

where $T_1(r)$ is the temperature distribution inside the hole, r is radial position from the center of the hole, R = 1.2 μm is the radius of the hole, and κ is the thermal conductivity of the suspended MoS_2. In the above equation, q(r) is volumetric Gaussian beam heating and given as $q(r) = \frac{I\alpha}{t}\exp(-r^2/r_0^2)$, where α =(9 $\pm$ 1)% is the absorbance of monolayer MoS_2 at 488nm [13], t=0.65 nm is the thickness of the flake, r_0=0.17 μm is the half of the Gaussian beam width, $I = P/(\pi r_0^2)$ is the peak laser power per unit area at the center of the beam spot. Outside the hole, the heat transports not only along the flake but also into the Si_3N_4 substrate, so its heat dissipation can be described as

$$\kappa' \frac{1}{r}\frac{d}{dr}\left[r\frac{dT_2(r)}{dr}\right] - \frac{G}{t}[T_2(r) - T(a)] = 0 \text{ for } r > R \quad 4.4$$

where $T_2(r)$ is the temperature profile outside the hole, G is the interfacial thermal conductance between MoS_2 and Si_3N_4 substrate, T_a is the ambient temperature and κ' is the thermal conductivity of the supported MoS_2. The solutions to Eqs. 4.3 and 4.4 are

$$T_1(r) = c_1 + c_2 \ln(r) + c_3 Ei(-\frac{r^2}{r_0^2}) \quad 4.5$$

$$T_1(\gamma) = c_4 I_0(\gamma) + c_5 K_0(\gamma) + T_a \quad 4.6$$

where I_0 and K_0 are the zero-order modified Bessel function of the first and second kind, respectively, $\gamma = r[G/(\kappa' t)]^{1/2}$, and $Ei(x)$ is exponential integral. Considering that $T_1(r)$ and $T_2(r)$ are finite when $r \to \infty$ and $r \to 0$, we can obtain $c_2 = -2c_3$ and $c_4 = 0$. The boundary conditions used to determine the values of constants c_i are as following:

$$T_1(R) = T_2(\gamma)\,|_{r=R} \quad 4.7$$

$$T_2(r \to \infty) = T_a \quad 4.8$$

$$-\kappa\frac{dT_1(r)}{dr}\,|_{r=R} = -\kappa'\frac{dT_2(\gamma)}{dr}\,|_{r=R} \quad 4.9$$

$$-2\pi Rt\kappa'\frac{T_2(r)}{dr}\,|_{r=R} = \alpha P \quad 4.10$$

With these boundary conditions, the temperature distribution $T_1(r)$ and $T_2(r)$ under various laser power can be described with three unknown parameters κ, κ' and G.

On the other hand, the weighted average temperature measured by Raman spectroscopy inside the beam spot is [102, 117]

$$T_m \approx \frac{\int_0^R T_1(r)q(r)rdr}{\int_0^R q(r)rdr} \qquad 4.11$$

By fitting this model with the T_m vs P determined by the Raman measurements, one can extract the thermal conductivity κ of suspended MoS_2 given the values of κ' and G. Here the parameters extracted on A_{1g} mode are used since it is less affected by strain [114]. If we make the assumptions that the supported and suspended MoS_2 have the same thermal conductivity ($\kappa = \kappa'$) and G= 50 MW/m^2K - a typical value for van der Waals interfaces [116, 118], the thermal conductivity value is extracted to be 34.5 W/mK. In fact, it is found that for the typical value of G ranging from 10 to 300 W/mK, the extracted κ only slightly changes by ± 0.4 W/mK, suggesting that the interface is not the dominant factor for thermal resistance. Also if we set $\kappa' = 0.1\kappa$ taking the reduction of thermal conductivity due to the substrate interaction into consideration, the fittedκ only increased slightly to 35.3 W/mK. That is to say, values of both κ' and G only affect κ by less than 1 W/mK. This could be attributed to the relatively low thermal conductivity of MoS_2. By examining the temperature profile as in Figure 4.9 (b) and (c) when heating the suspended MoS_2 using the laser, we could see that the temperature gradient from the center to the boundary of the hole is large, and the heat is not able to efficiently transfer to the surrounding regions. In this way, the temperature on MoS_2 at the edge of suspended region is close to the ambient temperature even that the temperature at the center of the flake has been increased to about 400 K. Furthermore, in Figure 4.9 (c) we also show the 1D temperature profile along x-axis if the flake under test is graphene (assuming laser power = 5 mW, laser absorption is 2.3%, and κ(graphene)=2000 W/mK). We compared cases with G=10 and 100 MW/m^2K

respectively for both graphene and MoS_2, where it could be clearly seen that the temperature profile for MoS_2 is almost immune to the varied values of G. However, in case of graphene, the overall temperature profile is more significantly changed under two different G values. Therefore, we could safely conclude that interfacial conductance and the thermal conductivity of supported flake are not playing a significant role if heat source is on the suspended region. This provides us a good chance to accurately determine the thermal conductivity of suspended MoS_2.

Including the uncertainty of the Raman shifts from the measurement set up [101], the extracted thermal conductivity is $\kappa = (34.5 \pm 4)$ W/mK at RT. This low thermal conductivity value is very close to that recently reported [119] for few-layer MoS_2 flakes =52 W/mK and two orders of magnitude less than that of monolayer graphene [100]. It is worth noting that the power dissipation through PL excited by 488 nm laser is negligible due to the low PL quantum yield ($\sim 4\text{x}10^{-3}$) of monolayer MoS_2 [13].

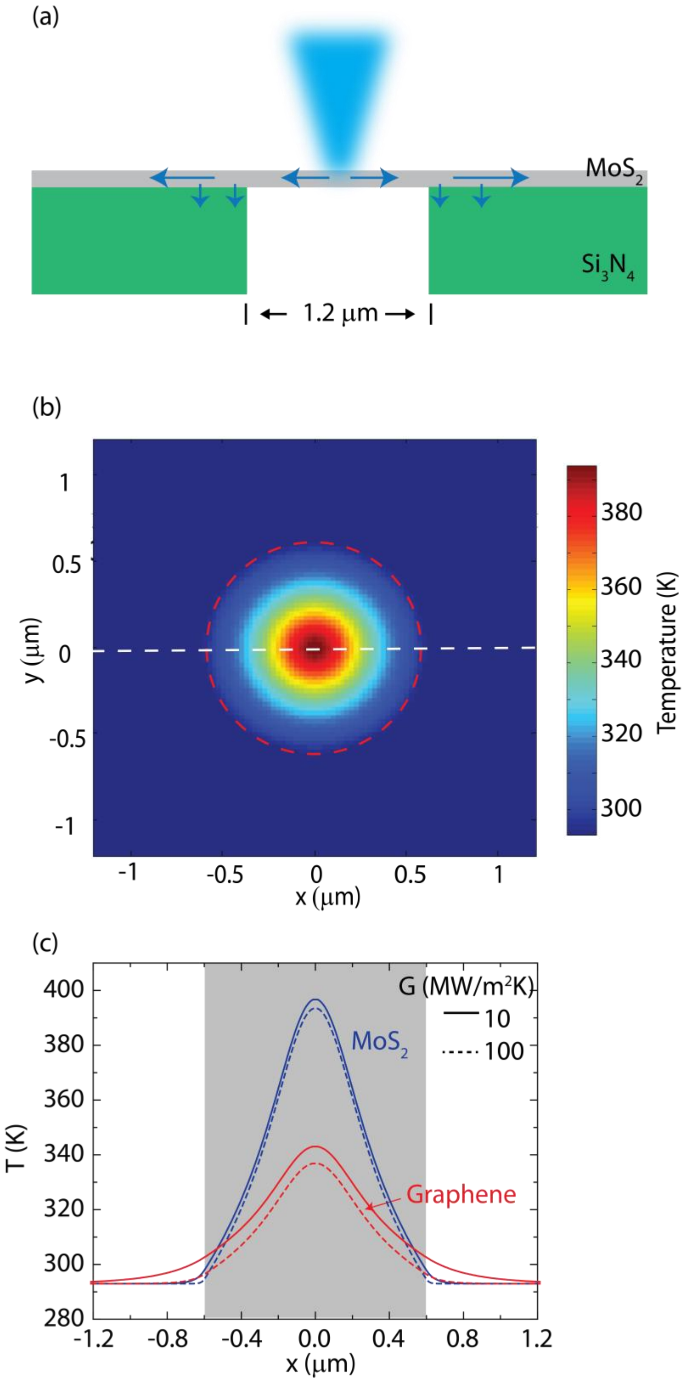

Figure 4.9 (a) The cross section of the sample structure and schematic of heat flow in monolayer MoS$_2$ suspended over a hole in Si$_3$N$_4$ under laser illumination. (b) The calculated temperature profile of the suspended MoS$_2$ under a 0.1 mW laser excitation by assuming G=50MW/m^{2}K, and κ=34.5W/mK. The temperature in the center of the hole reaches

about 390 K but drops to 295 K at the edge of the hole due to the low thermal conductivity of MoS2. The red circle marks the region of suspended monolayer MoS_2. (c) The temperature profile along x-axis at y=0 for both graphene (red) and MoS_2 (blue). The solid and dotted lines are respectively related to cases of G=10 and 100 MW/m^2K.

CHAPTER 5: ESAKI DIODES BASED ON VAN DER WAALS HETEROJUNCTIONS

5.1 Properties of van der Waals heterojunctions

Stacking of different layered materials on top of each other creates unique junctions, which are usually called van der Waals heterojunctions (vdW HJs). In contrast to conventional HJs based on covalently bonded materials, ones made from vertically stacked vdW materials do not suffer from lattice mismatch, which provides us huge freedom of junction and superlattice design [120-124]. The absence of dangling bonds on surfaces of such vdW materials also guarantees their high-quality interface with atomically sharp edge and minimal trap states, provided the adverse effects of oxidation are minimized. Therefore, the research field dealing with these vdW HJs grows rapidly over the past few years.

One of the most promising applications of vdW-HJs is interband tunneling based diodes and transistors with low power consumption and high on/off ratio [125, 126]. Jena/Feenstra first theoretically studied graphene/insulator/graphene HJs in 2011 [127]. Following that proposal, Britnell et al. demonstrated operation of a vertical tunneling transistor based on graphene/hBN/graphene HJs, with an on/off ratio of 50. Unfortunately, the ratios are too low to meet the requirements in logic circuits. Our group later proposed and analyzed an ultimately scaled TFET composed of a vdW-HJs with near broken-gap energy band alignment (Thin-TFET) in 2012-2014, where steep slope transistors with a subthreshold swing (SS) of 14 mV/dec, and more than 5 orders of on/off ratio are predicted.[128, 129] Experimentally, multiple groups have independently confirmed vertical, interband, and interlayer tunneling in vdW-HJs. Among these pioneering results, Roy et. al observed negative differential resistance (NDR) at cryogenic temperatures in MoS_2/WSe_2 junctions[122]. Resonant tunneling diodes exhibiting NDR built from epitaxial transition metal dichalcogenide (TMD) HJs as well as intentionally aligned graphene/hBN/graphene were also realized at room temperature (RT) [130, 131]. At the same time, we reported the first RT Esaki diode using a bP/$SnSe_2$ HJs taking advantage of its broken-gap (or type-III) energy-band alignments [33]. Immediately after these reports, Sarkar et al. achieved a steep slope tunneling transistors with an average SS~30 mV/dec using a 2D-3D geometry [132]. Although the efforts on such vdW based tunneling devices have just begun a few years ago, it already gained vast attentions and achieved tremendous progress. The most critical goal at present is to push this direction forward for the aspects of both device applications and physical understanding.

5.2 Esaki tunneling diode based on bP/$SnSe_2$ heterojunction

Esaki's discovery of NDR in heavily doped semiconducting germanium *p-n* junctions in 1958 was the first experimental evidence of quantum mechanical tunneling transport of electrons in all-condensed-matter systems [133]. This discovery motivated Giaever's tunneling experiments that proved the existence of the superconductive energy gap predicted by the then-newly formulated Bardeen-Cooper Schrieffer (BCS) theory of superconductivity [134]. After these initial breakthroughs, tunneling in various classes of crystalline matter has been observed, and forms the basis for several practical applications. For example, Josephson junctions exploit tunneling in superconductors for exquisitely sensitive magnetic flux detectors in superconducting quantum interference devices (SQUIDs) [135], and are now being investigated as the building blocks of quantum computers. Electron tunneling forms the basis for low-resistance ohmic contacts to heavily doped semiconductors for energy-efficient transistors, as low-loss cascade elements in multi-junction solar cells, and for coherent emission of long-wavelength photons in quantum-cascade lasers [136]. In addition to such practical applications, the extreme sensitivity of tunneling currents to various electronic, vibrational, and photonic excitations of solids makes tunneling spectroscopy one of the most sensitive probes for such phenomena [137].

Here we use two layered materials – bP and $SnSe_2$ - are successfully integrated for the first time, enabling the conclusive achievement of Esaki-diode behavior in 2D crystal semiconductors at room temperature. We use the Esaki diodes to experimentally prove that the heterojunction possesses a type-III (broken) band alignment. The bP/$SnSe_2$ heterojunction is one between *mixed-valence* materials, because black phosphorus is elemental and $SnSe_2$ is a compound semiconductor. Furthermore, the two constituents have different *crystal structures*. Given all these differences, it is rather remarkable that a robust NDR can be observed at room temperature in this heterostructure.

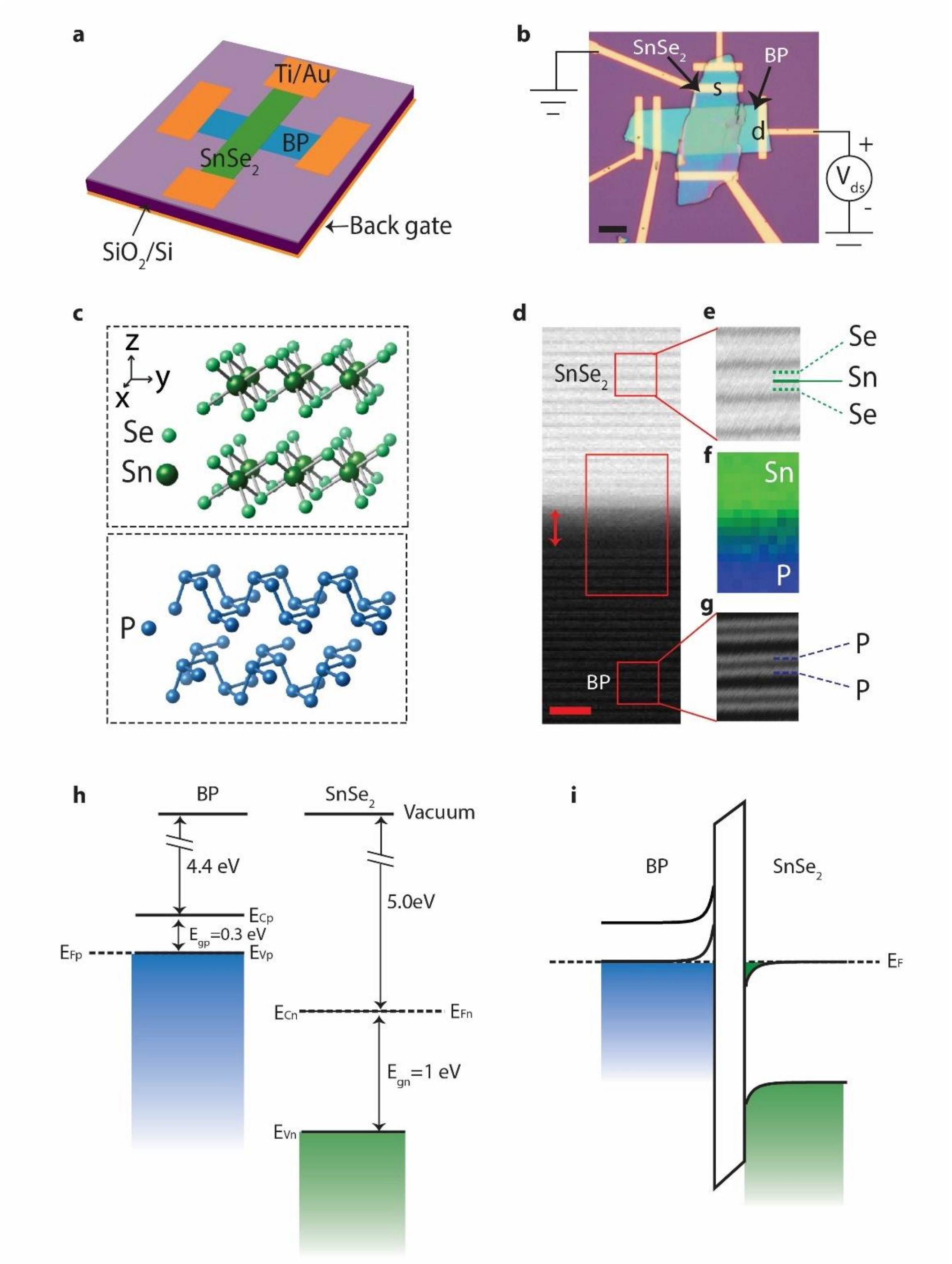

Figure 5.1 (a) and (b), Schematic illustration and optical image of fabricated devices on SiO_2/Si substrates. The scale bar is 5 um. A voltage V_{ds} is applied on the p-type bP with the n-type $SnSe_2$ grounded. (c) Crystal structures of bP and $SnSe_2$. BP is composed of two planes of phosphorus atoms arranged in puckered layers and $SnSe_2$ has a CdI_2 type structure with each plane of Sn atoms sandwiched between two planes of Se atoms.

Layers in bP or $SnSe_2$ are bonded together by vdW force, which allows exfoliation of these crystals into thin flakes. (d), (e), and (g), Cross-sectional STEM images. (d) shows the presence of a thin barrier (~ 1.6 nm) at the interface. The scale bar is 2 nm. (e) shows the tri-atomic-plane layer structure of $SnSe_2$. (g) shows the bi-atomic-plane layer structure of bP. The measured interlayer distance of $SnSe_2$ is 0.65 nm and that of bP is 0.55 nm. f. EELS map: Sn in green and P in blue. (h) Energy band profiles of BP and $SnSe_2$ prior to contacting each other. bP has a low work function compared to that of $SnSe_2$. (i) Band alignment at equilibrium. Accumulations of holes in bP and electrons in $SnSe_2$ result from electron transfer from bP to $SnSe_2$ owing to a lower work function of bP than that of $SnSe_2$.

The Esaki diode device structure is schematically shown in Figure 5.1 (a). The devices are fabricated using a dry transfer process with flake thicknesses of ~50-100 nm for both bP and $SnSe_2$ (the transfer method is described in Appendix B). bP is the p-type semiconductor, and $SnSe_2$ the n-type semiconductor of the vdW Esaki diode. Figure 5.1 (b) shows an optical image of a representative device. The thicknesses of bP and $SnSe_2$ in this device are 79 and 95 nm, determined by atomic force microscopy (AFM). Figure 5.1 (c) shows the crystal structures of bP and $SnSe_2$. bP possesses an orthorhombic crystal structure. Each phosphorus atom is covalently bonded to three adjacent atoms in a puckered layer, thus forming two atomic planes in each layer of bP [138]. In comparison, $SnSe_2$ consists of planes of Sn sandwiched between two planes of Se atoms, forming a hexagonal CdI_2-type structure [139]. Figure 5.1 (d) shows the high-angle annular dark-field scanning transmission electron microscopy (HAADF-STEM) images of the $SnSe_2$-bP interface taken by Yimo Han. Figure 5.1 (e) and (g) are the zoomed-in HAADF-STEM images of $SnSe_2$ and bP, showing the tri-atomic-plane $SnSe_2$ layers with an interlayer distance of 0.65 nm and the bi-atomic-plane bP layers with an interlayer separation of 0.55 nm. The measured layer thicknesses for both materials are very close to the values in the literature. At the interface, an amorphous layer with a thickness ranging from 1.2 nm to 2 nm is observed, which is thicker than a typical vdW gap of 0.4 – 0.6 nm [27]. Electron energy loss spectroscopy (EELS) composition analysis of this layer is shown in Figure 5.1 (f). It reveals carbon and traces of phosphorus and Sn. We speculate that the presence of carbon most likely stems from the flake transfer process, while the presence of P and Sn likely results from the finite interdiffusion, assisted by the degradation of the bP and $SnSe_2$ flake surfaces prior to being stacked together due to their widely known instability in air [140]. We can not completely rule out that bP and $SnSe_2$ near the interface suffered from degradation during the TEM sample preparation and imaging process, as observed by other groups [140]. However, it is worth highlighting that the double atomic planes in a bP layer is resolved by TEM for the first time in this work, to the best of our knowledge. This can be attributed to the aberration correction up to the 5th order and the low electron beam energy used: 100 keV.

High doping densities boost the NDR characteristics in traditional semiconductor Esaki diodes, which applies in these vdW Esaki diodes as well. The bP flake is unintentionally p-type doped, and the $SnSe_2$ flake is unintentionally doped n-type. This is consistent with other groups' observations [141, 142]. We confirm the individual doping types unambiguously by the opposite directions of field-effect conductivity modulation of each layer (supplementary Fig. S1a). That the effective doping densities are high manifests in the relatively weak current modulation in the individual flakes, which is also attributed to the large flake thicknesses. Figure 5.1 (h) shows the energy level alignments of conduction and valence band edges of the *p*-type bP and *n*-type $SnSe_2$ based on the reported electron affinity values in the literature [143, 144]. Based on these alignments, they are expected to form a type-III, broken-gap heterojunction similar to InAs/GaSb tetrahedral 3D semiconductors. The large work function difference leads to an accumulation of holes in BP and electrons in $SnSe_2$ near the junction, and an effective *p*-*i*-*n* junction is formed in our devices owing to the presence of the aforementioned interfacial layer (Figure 5.1 (i)). Away from the junction, it is assumed that the unintentional *p*-type doping is such that it puts the Fermi level of p-bP (E_{fp}) near its valence band edge (E_{vp}), and the doping in *n*-$SnSe_2$ puts its E_{fn} near its conduction band edge (E_{cn}). Both layers are thus effectively ‘degenerately’ doped. Though the tunnel barrier in this work is formed unintentionally, thin BN layers or other suitable barrier materials with improved quality can be used: which is the focus of our future work.

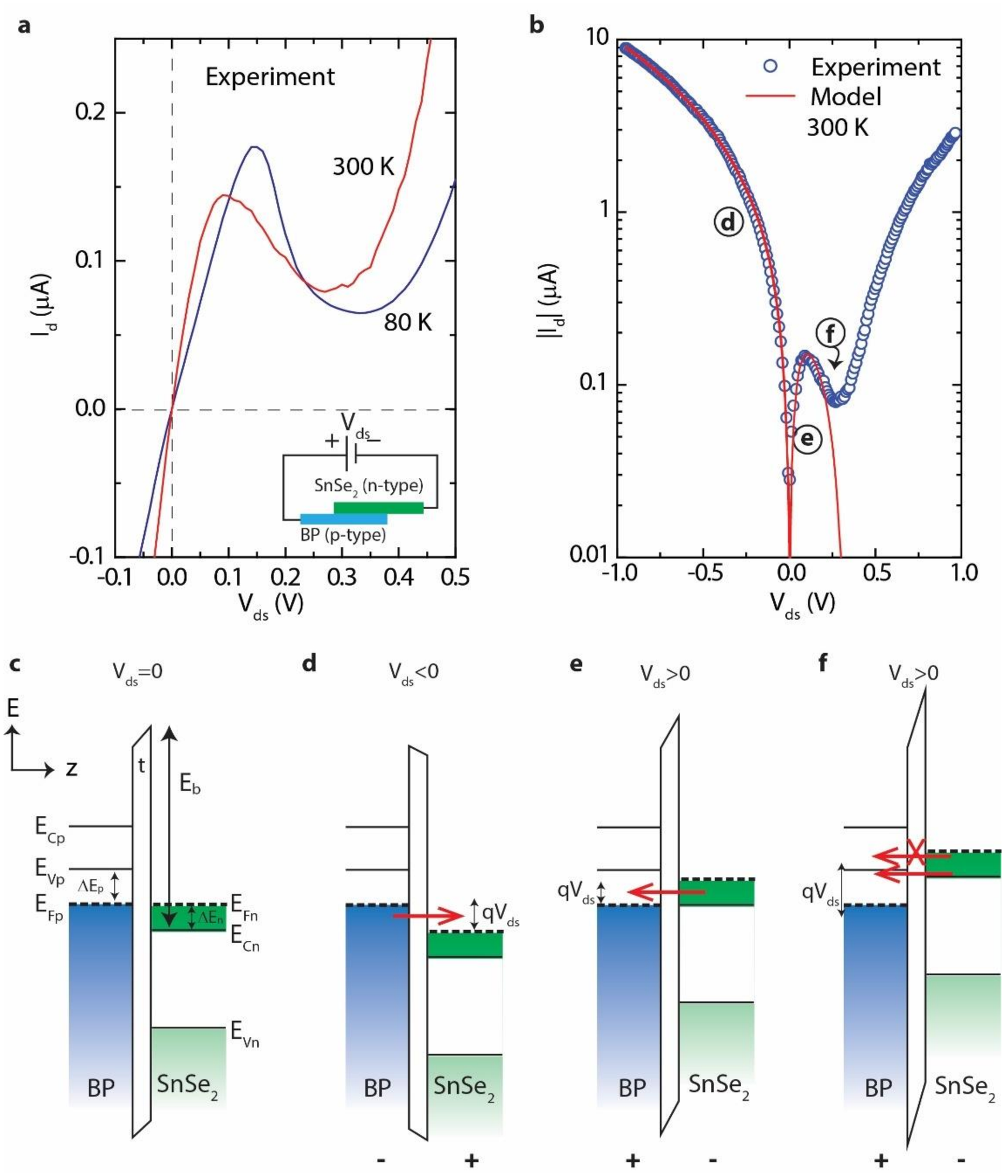

Figure 5.2 (a) I_d-V_{ds} curves at 80 and 300 K in a linear scale. At lower temperatures, the peak current increases and the valley current decreases thus an increase in the peak-to-valley ratio, as expected from the theory (b) Comparison of experimental and theoretical I_d-V_{ds} curves at 300 K in a log scale. Excellent agreement is achieved. (c), (d), (e), (f), Band alignment at V_{ds}=0, V_{ds}<0, and V_{ds}>0. When the conduction band electrons in $SnSe_2$ have a maximal overlap with the valence band holes in BP (V_{ds}>0), the Esaki tunnel diode reaches its peak current. With further increasing V_{ds} (f), part of the conduction band electrons in $SnSe_2$ see the forbidden band gap of BP, thus leading to a reduction in current.

Figure 5.2 (a) presents the measured I_d-V_{ds} curves at 80 and 300 K in a linear scale, where the most notable feature is the appearance of NDR while the junction is positively biased (V_{ds}>0). The same data at RT are plotted in a logarithmic scale in Figure 5.2 (b) (blue circles) to showcase the backward diode behavior: current under reverse bias is higher than that at forward bias, opposite to a typical p-n diode. The simultaneous appearance of NDR and backward-diode behavior is a conclusive fingerprint of interband tunneling transport of electrons. All results presented in this work are obtained by applying a drain voltage V_{ds} on BP (p-type, terminal "d") with the $SnSe_2$ (n-type, terminal "s") being grounded. For example, for V_{ds}>0 electrons drift through the conduction band of n-type $SnSe_2$, tunnel through the barrier into the empty valence band states in p-type BP, and drift through this valence band to emerge at the bP ohmic contact (see Figure 5.2 (e), (f)). The band alignments of the vdW Esaki diode close to the bP/$SnSe_2$ interface under various bias conditions are sketched in Figure 5.2 (c)-(f). At equilibrium, the Fermi level E_f lies between E_{vp} and E_{cn} (also see Figure 5.1 (i)). When a reverse bias voltage V is applied (Figure 5.2 (d)), a finite energy window is created for electrons to tunnel from the filled valence band states of bP into the empty conduction band states in $SnSe_2$: the transport is driven by the difference between the hole quasi Fermi level E_{fp} and electron quasi Fermi level E_{fn} that satisfy: $E_{fp} - E_{fn} = qV$, where q is the elementary charge. Increasing the reverse bias simultaneously widens the energy window for tunneling, and increases the tunneling probability because of a stronger field, leading to a sharp increase in the tunneling current. This is clearly observed in our devices, the region "d" in Figure 5.2 (b), and captured accurately with a tunneling transport model as described later. Under a small forward bias ($0<qV_{ds}< \Delta E_n$, where $\Delta E_n = E_{fn} - E_{cn}$), electrons residing in the conduction band of n-SnSe$_2$ are able to tunnel to the empty states in the valence band of p-BP through the energy window of $E_{fn} - E_{fp}$ (Figure 5.2 (e)). This tunneling current reaches its peak when the occupied conduction band states in SnSe$_2$ have a maximal overlap with the unoccupied valence band states in bP. Further increase of the voltage aligns the occupied conduction band states with the forbidden bandgap of BP. Then the tunneling current decreases in spite of a slight increase in tunneling probability induced by a stronger electric field across the barrier. The diode current reaches its minimum (valley) value, which is typically dominated by a combination of defect and phonon assisted tunneling and thermionic currents [145], followed by an upturn due to the overriding thermionic emission current.

A simple model of interband tunneling using the Wentzel-Kramers-Brillouin (WKB) approximation is able to capture all the essential experimental tunneling features quantitatively in these vdW heterojunction Esaki diodes. While the details of the model appear in the Supplementary Information (SI), its essence is described briefly here. The device tunneling current is calculated by summing the individual single-particle contribution from all electron states in the k-space [146] that are allowed to tunnel:

$$I_t = q\frac{g_s g_v}{L_z}\sum_{k_n}\sum_{k_p} v_z(F_n - F_p) T_{WKB}\,\delta(E_p - E_n)\,\delta(k_{xp} - k_{xn})\,\delta(k_{yp} - k_{yn}) \tag{5.1}$$

where g_s and g_v are the spin and valley degeneracy in the band structure, L_z is the macroscopic device length along the electric field direction z, $v_z = \hbar k_{zn}/m_{zn}$ is the band group velocity in the source side, F_n and F_p are the Fermi-Dirac distribution functions, respectively, in n-SnSe$_2$ and p-bP , and T_{WKB} is the WKB tunneling probability. The three Dirac-δ functions in Eq 5.1 simultaneously ensure energy (E) conservation and in-plane momentum $(k_x$ and $k_y)$ conservation. The numerically evaluated tunneling current is shown in Figure 5.2 (b) as a red solid line, and is seen to explain the entire tunneling portion of the current: both in reverse and forward bias, before the thermionic/diffusive-part takes over at large forward bias. The model incorporates an effective barrier lowering of $\vartriangle \phi_{\mathrm{b}} = \sqrt{q\,\Xi\,/4\pi\epsilon_r\epsilon_0}$ where a relative permittivity $\epsilon = 6$ is used and Ξ is the electric field across the tunnel barrier. At 300 K, the best fit of the model to the experimental tunneling current is obtained by setting $\vartriangle E_p = E_{vp} - E_{fp} = 0.27$ eV, $\vartriangle E_n = E_{fn} - E_{cn} = 0.07$ eV, a barrier height $E_b =$ 4.7 eV, and a tunneling barrier width t =1.3 nm. The effective doping induced degeneracies and energy scales are reasonable, and the tunnel barrier thickness is in agreement with the physical barrier thickness measured by STEM for the vdW p+/*i*/*n*+ heterointerface. Recognizing that the tunneling probability is exponentially dependent on the barrier height and thickness, a peak tunnel current map is generated as a function of these two parameters in Figure 5.3. For example, the experimentally observed peak current at RT can be reproduced using a barrier thickness of 2 nm with a barrier height of 2 eV as well as a barrier thickness of 1.3 nm with a barrier height of 4.7 eV. Considering the effective tunneling area might be smaller than the physical overlap region area (~10x10 μm^2) due to the potential surface contamination during dry transfer, we believe the property of the tunnel barrier between bP and SnSe$_2$ is most likely spatially distributed and largely falls in the parameter window explored in Fig.3.

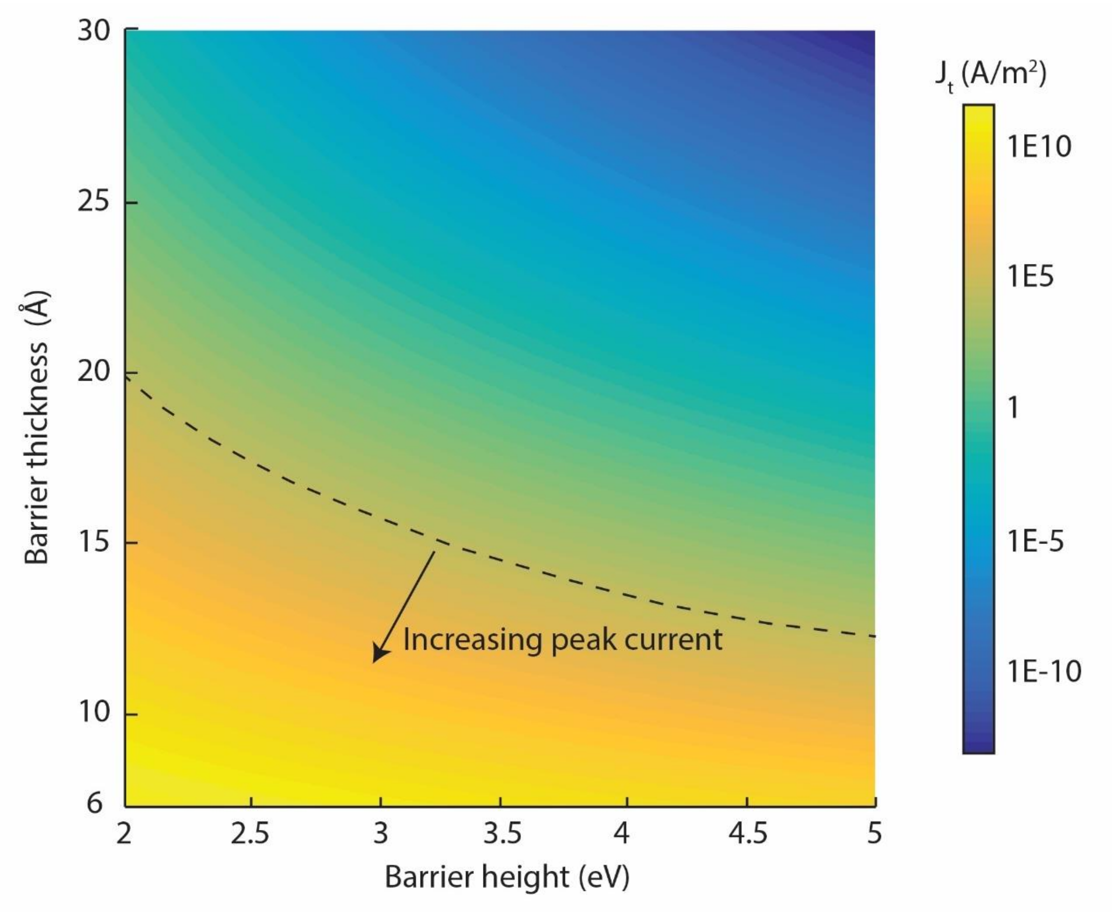

Figure 5.3 Calculated peak current density in the bP/SnSe$_2$ Esaki diode mapped over a range of tunnel barrier heights and thicknesses. The dash line marks the measured peak current density shown in Fig. 5.2, which is around 1.6x10^3 A/m^2. For the modeled I_d-V_{ds} curve shown in Fig. 2, the following parameters: E_b=4.7 eV and t=13 Å, render an excellent match with the measured I_d-V_{ds}.

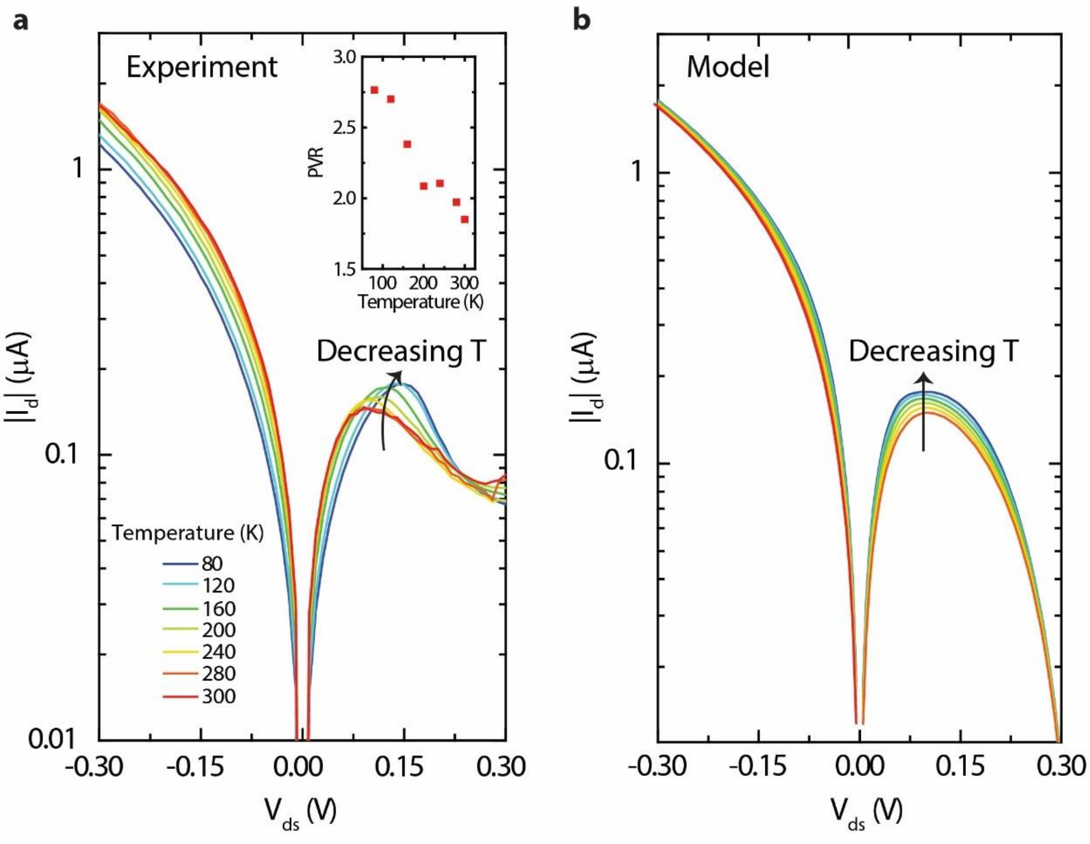

Figure 5.4 (a), (b), Experimental and theoretical I_d-V_{ds} curves in a temperature range of 80 to 300 K. As temperature decreases, the peak current increases as a result of a tighter Fermi-Dirac distribution of the carriers. The devices suffered from poor ohmic contacts at low temperatures, which shifts the peak voltage to a higher value under the forward bias and lowers the apparent tunneling current under the reverse bias. Inset of a shows the measured peak to valley ratio as a function of temperature.

The current contribution from tunneling mechanism is expected to have a weak dependence on temperature to the extent of thermal smearing of the Fermi occupation functions. To verify this, we performed temperature dependence I_d-V_{ds} measurements. Figure 5.4 shows the measured and modeled I_d-V_{ds} curves for temperatures ranging from 80 to 300 K. The measured temperature dependence is in excellent agreement with the model, highlighting its predictive capability in spite of the simplicity. A critical feature in the characteristics is the evolution of the peak current I_p in the NDR region as a function of temperature: I_p increases slightly with decreasing T. The Fermi-Dirac tail shortens with decreasing temperature, making the electron occupation probability difference in the *n*- and *p*- sides $F_n - F_p$ larger, increasing I_p. This temperature dependence is in stark contrast to thermionic emission, or phonon/trap-assisted tunneling, which typically shows an opposite trend of decreasing current with decreasing temperature. The peak voltage is observed to shift to a higher value at lower temperatures because the ohmic contacts confirmed at RT become Schottky-like at lower temperatures. For the same reason, the reverse bias currents are seen to be slightly lower at low T than that at RT. The inset of Figure 5.4 (a) shows that the extracted peak-to-valley ratio (PVR) of NDR varies from 2.8 at 80 K to 1.8 at 300 K. Similar trends are also observed in Esaki diodes made of 3D semiconductors, such as Ge, Si [147, 148].

The broken-gap energy band alignment of the bP/$SnSe_2$ vdW interface is unusual, and of high interest for future applications. The tunneling current model provides the first sign of this band alignment. To conclusively verify the broken-gap energy alignment, we explore the photo response of the heterojunction under illumination from a 488 nm laser, as shown in Figure 5.5. Since the Esaki diode forms a perfect “ohmic” contact near zero voltage, the sign of the photocurrent and photovoltage uniquely correlates with the energy band bending in the heavily doped $p+$ and $n+$ regions near the junction. If the band bending is such that carriers of opposite sign *accumulate* near the junction as shown in the inset of Figure 5.5 (a), the resulting photocurrent will move the Esaki diode I-V curve up into the 2nd quadrant. If the band bending is such that carriers of opposite sign *deplete* near the junction as a typical p-n diode, the photoresponse I-V will move into the 4th quadrant, like a solar cell. Provided that the Fermi level in *p*-bP (*n*-$SnSe_2$) is very close to its valence (conduction) band edge as argued above, the movement of the I-V curve into the 2nd quadrant in Figure 5.5 (a), and the resulting negative open-circuit voltage is a signature of a broken-gap alignment. Though it is impossible to rule out the formation of unintentional charged states at the vdW heterointerface in this study, the energy band alignment in bP/$SnSe_2$ diode is most likely of type-III. The observed Esaki diode behavior and its peculiar photo response, combined with the reported properties of the layered materials point strongly towards this conclusion. With an absorption coefficient of $\sim 5\times10^5$ cm^{-1} of $SnSe_2$ bulk crystals at 488 nm, we estimate the laser power reaching the vdW heterojunction, and the device responsivity at zero bias to be ~0.24 mA/W. This value is comparable to those reported in other layered materials [138].

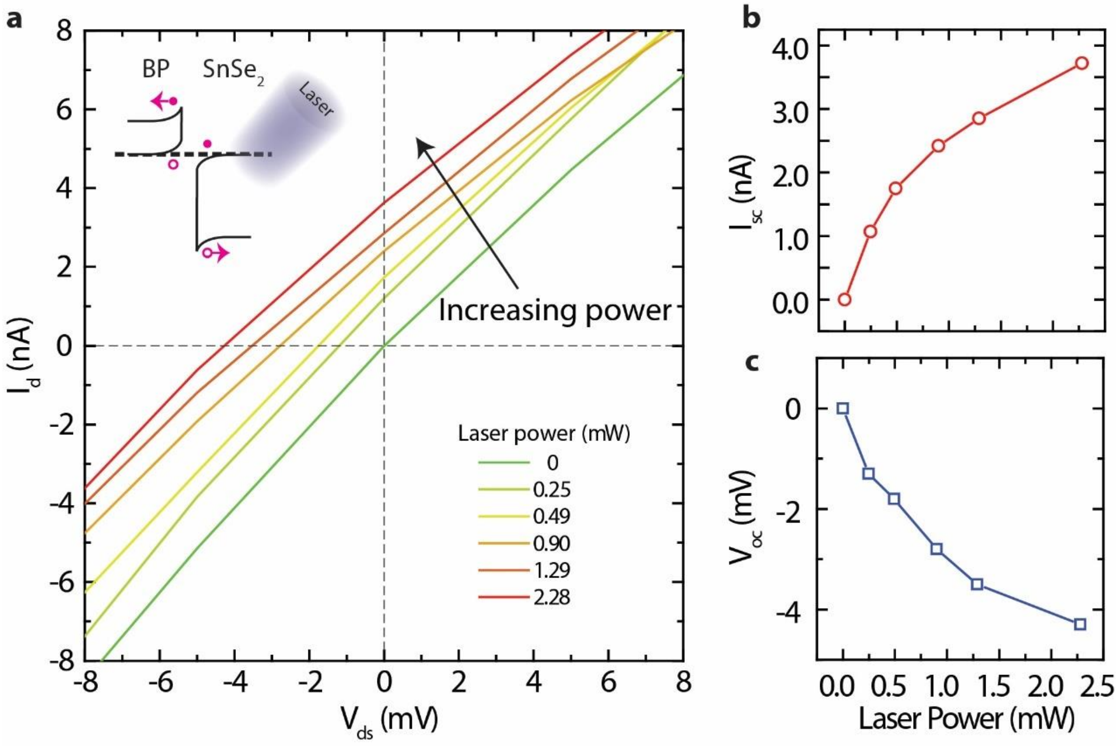

Figure 5.5 Current-voltage behavior of the bP/SnSe$_2$ Esaki diode under illumination of a 488 nm laser. (a), I_d-V_{ds} curves near zero bias. Laser power is varied from 0 to 2.28 mW and the laser beam diameter is about 3 um illuminating the vdW junction only, excluding the metal/2D regions. The sign of the short-circuit current I_{sc} and the open-circuit voltage V_{oc} is opposite to that of a common p-n junction or solar cell, confirming the band bending in bP (accumulation of holes) and SnSe$_2$ (accumulation of electrons) thus the type-III or broken band alignment. The inset shows this confirmed band bending. (b), (c), I_{sc} and V_{oc} as a function of the laser power.

5.3 Electronic oscillators built upon Esaki diodes

It is well known that tunneling-diode based oscillators are favorable in microwave or higher frequency range owing to the extremely fast transit time of carriers inside the device. For example, RTDs consisting of multiple layers of

AlAs/InGaAs/AlAs stacks can work up to 1.92 THz, highest frequency of RT electronic oscillator to date [149]. As a proof-of-concept application and demonstration of robustness of the observed NDR in vdW-HJs, we measured oscillations using the set up shown in Figure 5.6 (a), where an external inductor is connected in series with the diode. A voltage amplifier is connected in parallel in order to provide high impedance before oscillation signals are feed into spectrum analyzer. The capacitance of the resonant LC circuit is mainly provided by BNC cables. The equivalent circuit is depicted in the inset of Figure 5.6 (c). While the diode is biased to the NDR regime, oscillations are clearly observed as shown in Figure 5.6 (b). The oscillation frequency could be tuned by changing the inductors externally. Simple circuit analysis indicates that oscillation frequency $f_0 \sim \frac{1}{2\pi\sqrt{LC}}$, hence, by fitting f_0 with $1/\sqrt{L}$, total capacitance C_t is extracted to be ~185±6 pF, which is close to the capacitance of BNC cables used in this measurement (~190 pF measured by multimeter). Figure 5.7 (a) and (b) show the power spectrum of the oscillation and phase noise measured by spectrum analyzer while a 2.2 mH inductor is connected. Signal to noise ratio is found to be >50 dB, and the phase noise is ~ 100 dBc/Hz at 10 kHz; both metrics are **the best** in comparison with all the reported 2D material based oscillators[150, 151], and the oscillators built from thin film transistors on flexible substrates[152-156]. The measured ~1 MHz frequency is not the intrinsic device performance, but primarily dominated by total capacitance contributed by BNC cables. The rough estimate of the intrinsic device frequency suggested it is around 0.2 GHz. Through more carefully designing contacts pads on insulating substrates, we expect to extract the intrinsic frequency response of oscillations with high accuracy.

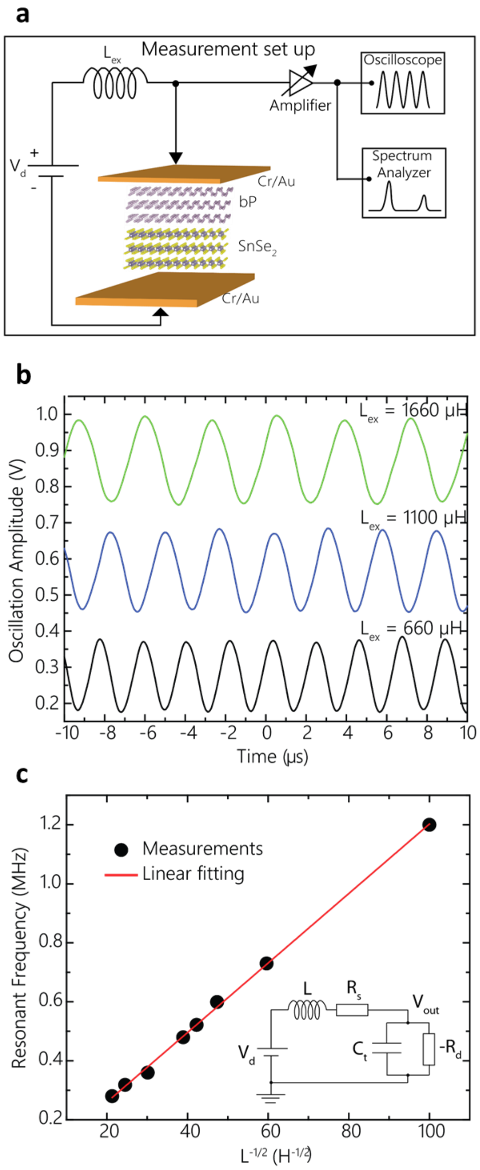

Figure 5.6 (a) Schematic of the measurement setup. (b) Oscillation observed on oscilloscope with various external inductor values. (c) Extraction of the oscillator capacitance, which is found to be indeed approximately equal to that of the cable in the setup. The inset is the equivalent circuit of the overall oscillator.

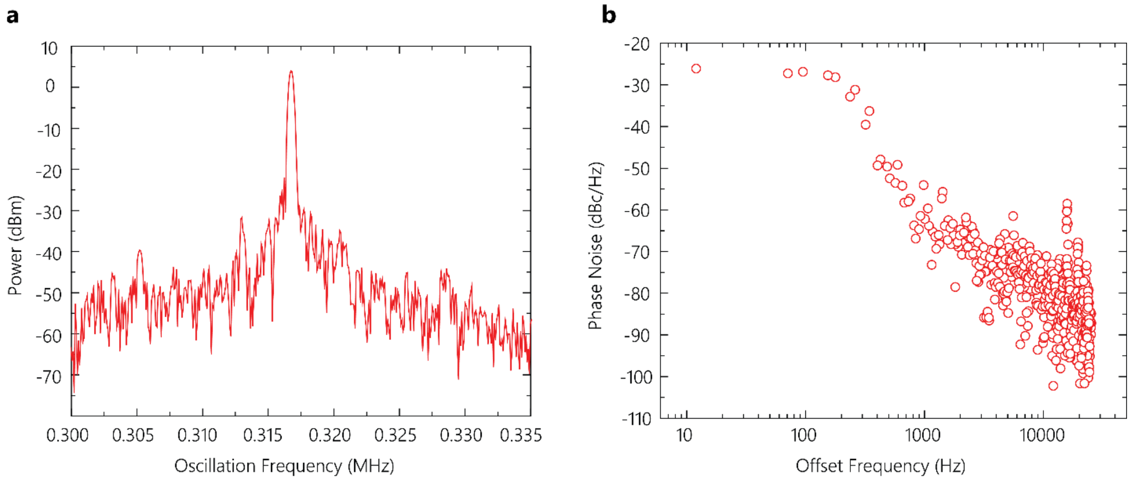

Figure 5.7 (a) Power spectrum, showing a decent output power (~ 10 uW without amplifier; in comparison ~ 1 nW was reported in Ref.[151]), a high sign-to-noise ratio of >50 dB. (b) Phase noise is as low as – 100 dBc/Hz at 10 kHz. These results are the best reported on layered materials though there is clearly room for improvement.

5.4 Summary

In conclusion, we have demonstrated an Esaki tunnel diode using vdW heterojunctions with a type-III energy band alignment composed of bP and $SnSe_2$ for the first time. Our study suggests 2D crystals as promising candidates for future tunneling based devices. In addition to that, an electronic oscillator built upon this layered Esaki diode is further demonstrated with an oscillation frequency of 1.2 MHz. In the layered heterojunction materials, the lack of strong interlayer covalent bonds presents exactly such an electronic void, which helps decouple the band alignment and allows the robust NDR observed here. On a more general note, we mention that the robust Esaki-type NDR reported in this work is not entirely new – and has been seen over the past half century in various group-IV and III-V semiconductor heterostructures.

However, its observation in layered semiconductors that lack out of plane chemical bonds is potentially a starting point for several investigations in the future. Unlike III-V and group-IV semiconductors and their heterostructures, layered semiconductors can be semiconducting, insulating (BN), but also metallic and/or or superconducting ($NbSe_2$). This means one can create seamless heterostructures of semiconductors with superconductors and insulators without interface traps, and investigate the tunneling of particles - be it of single-particle type (in semiconductors), or correlated (in superconductors) between various material families. The fine structures in such tunneling experiments can also serve as the most sensitive tools for the measurement of band alignments, phonon modes, elastic vs inelastic tunneling physics, and a host of potentially unforeseen physics.

CHAPTER 6: FUTURE WORK

6.1 High performance graphene THz modulators

The THz technology has found applications in an increasingly variety of areas such short distance communications, biology and medical science, food quality control, global environment monitoring, etc. The realization of these proposed applications is highly dependent reliable and versatile optical components functional in THz range, such as modulators for active control of the electromagnetic waves [53]. Up to date, the development of high performance THz modulators still cannot satisfy the requirements of practical use.

As has been proposed in Chapter 3, the near-field enhanced graphene based THz modulators promises high performance including superior modulation depth, high operation speed and moderate insertion loss. We have conducted some initial experiments which have demonstrated the validation of our proposed structure and simulations. In those proto-type samples, we modify the graphene conductivity by passive methods including stacking graphene layers as well as chemical doping. The change of transmission as conductivity is observed and closely follows the simulated results. We plan to proceed to fabricate the devices that could be dynamically controlled.

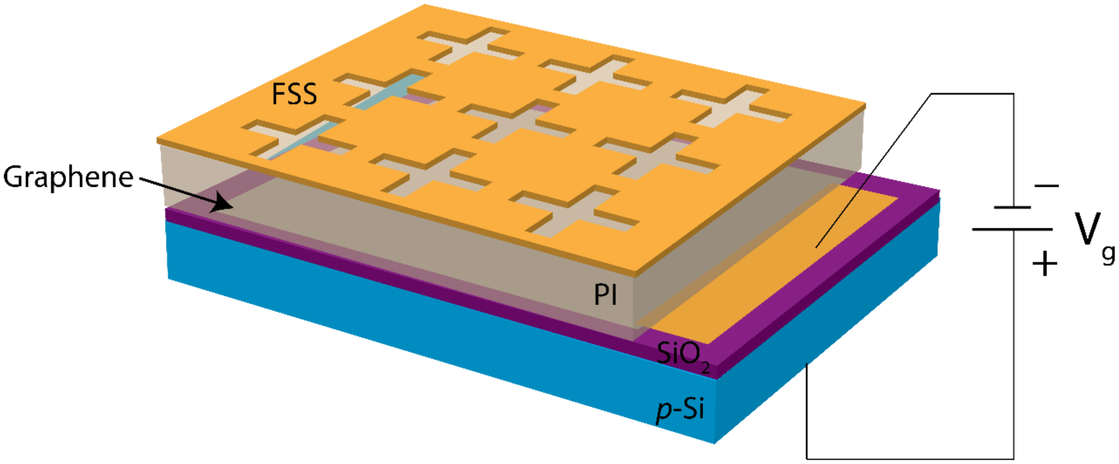

Figure 6.1 Sketch of proposed near-field enhanced THz modulator. It consists of thin membrane of p-Si, 300 nm SiO_2, graphene with metal contact, PI spacer, and metallic FSS.

Active control of THz waves could be realized by electrical tuning of graphene conductivity. One of most convenient and used ways of dynamic modification of graphene conductivity is by a simple Si-SiO_2-graphene structure. However, a few hundred microns thick Si substrate induce Fabry-Perot cavity effects which drastically disturb the characteristics of FSS. Therefore, it is necessary for us to thin down the Si substrate to less than 10 µm. The structure proposed is shown in Figure 6.1. The process of fabricating such a structure includes LPCVD Si_3N_4 deposition, Si etching, Graphene transfer, PI spinning and curing, and the metallic FSS formation. Detailed process flow starting from a 300 nm SiO_2 covered Si substrate is:

1) 30nm Si_3N_4 deposition by LPCVD.
2) Etching region (device region) defining using photolithography.
3) RIE etching of Si_3N_4.
4) Si etching with KOH solutions.

5) Si_3N_4 removal with RIE.

6) Graphene transfer on top of SiO_2.

7) Deposition Ti/Au metal contact to graphene.

8) PI spinning and curing.

9) Al deposition

10) Defining the FSS with photolithography and Al etchant

After device fabrication, bias can be applied between the Ti/Au contact and the Si substrate to tune graphene conductivity. A THz frequency-domain spectroscopy (Emcore PB7200) is employed to measure the transmittance of the whole structure under various gate voltages. We have demonstrated the validity of our simulations in Chapter 3. From Figure 3.17, we could expect that, such modulators could achieve a MD more than 80%.

Beyond that, we could further improve the speed of THz modulators by reducing the active area of graphene. As discussed in Chapter 3, one of most critical issue limiting the modulation speed is the large graphene area in previously designed devices. Here, after spatially localizing the THz waves into specific regions using FSS, we could potentially reduce the graphene area but maintain the similar modulation capability. This is one of most beneficial advantages of our proposed near-field enhanced THz modulators. The proposed device structure is shown in Figure 6.1. The main difference in this device is patterning of graphene layer. Instead of using a whole layer of graphene, we pattern the graphene layers to complementary structure of FSS. The decrease of active area leads to a reduction of capacitance, thus the time constant considering $\tau = RC$. As could be seen from Figure 3.14, the electromagnetic waves are highly confined into the opening of cross slots after FSS. Therefore, such a design could still realize THz modulation as efficiently as ones without patterning of graphene. In fact, cross slot FSS is just one of most simple structure widely used in metamaterial field. By clearly designing the structure of FSS, we could potentially minimize the product of RC to realize highest modulation speed.

6.2 Two-dimensional tunneling junctions

Following our pioneering work in vdW tunneling junctions composing of semiconductor/semiconductor stacking, we propose to investigate Josephson junctions all made of 2DLM, as proposed in Figure 6.2. As the basic building block of superconducting qubits, Josephson junctions are of great interests over the years [157]. The proposed structure could be realized by stacking exfoliated superconducting $NbSe_2$ [158] and gapped layered materials such as WSe_2 or h-BN as tunneling barrier. These vdW heterojunction based Josephson junctions are expected to preserve high quality interface and prominent tunneling currents with careful handling and preparations. Moving all the dry transfer setup (see Appendix B) we are using now in air into glove box would be a critical step of constructing such vdW heterojunctions, especially while dealing with air-sensitive materials like bP, $SnSe_2$, $NbSe_2$ etc. It is advantages to demonstrate the operation of proposed Josephson junctions over vdW interface because of their facile integration into complicated system for quantum computing in comparison with epitaxially grown 3D counterpart that is limited by lattice mismatch.

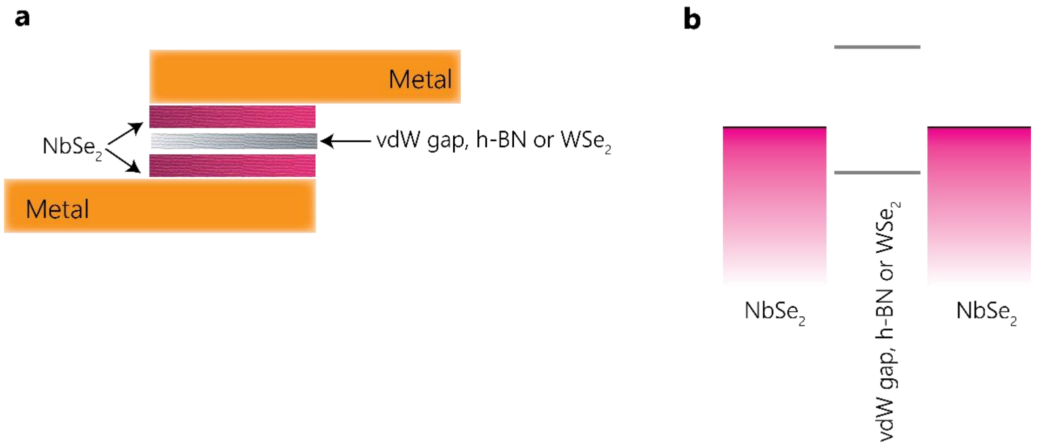

Figure 6.2 Proposed vdW tunnling junctions. (a) Josephson junctions (b) Band alignment of proposed heterojunctions

6.3 Bandgap engineering in bilayer TMDs

One of the most promising applications of TMDs family lies in optoelectronics due to the present of band gap. While the inherent band gap of monolayer MoS_2 is advantageous in comparison with graphene, the ability to manipulate the band gap of TMDs is even more fascinating. Significant efforts of band gap engineering have been devoted in graphene. One of most interesting strategies is tuning its band gap by external electric field in bilayer graphene.[5] An electric field applied normal to the graphene sheets breaks the inversion symmetry of the bilayer structure and opens up a band gap. Remarkably, this band gap is continuously tunable up to around 250 meV.[5] Recent theoretical efforts have shown possibility of such band gap engineering in TMDs. With a moderate strength (2-3 V/nm) perpendicular electric field through the bilayer TMDs, the band gap is possibly closed to zero. As shown in Figure 6.3, the band gaps of TMDs including MoS_2, $MoSe_2$, $MoTe_2$, and WS_2 are calculated using density functional theory. It could be seen that, when increasing the external electric field, the band gap is linearly and continuously decreasing. In Figure 5.4, we compared the tunability of the band gap for both MoS_2 and graphene as a function of external electric field, where it could be seen that, under similar strength of the field, the change of band gap in MoS_2 is much larger than that of graphene. This motivates us to pursue the experimental demonstration of this band gap tuning capability.

Up to now, all of these conclusions are obtained based on calculations. To demonstrate this exceptional function experimentally, we are going to fabricate a dual-gate bilayer MoS_2 field effect transistor. The proposed device is shown in Figure 6.5. Following the bilayer MoS_2 exfoliation onto a 300 nm SiO_2 covered Si substrate, e-beam lithography and e-beam Ti/Au evaporation are used to define the source/drain contacts. After that, 10 nm HfO_2 is deposited using ALD method. Finally, a 20 nm semi-transparent Pt is used as top gate. In this way, an external electric field is applied through the MoS_2 plane. If we donate $E_{tg}=V_{tg}/t_{tg}$ and $E_{bg}=V_{bg}/t_{bg}$, we could obtain $E_{total}=E_{tg}-E_{bg}$. Considering the quality of dielectrics our setup could achieve, it is possible to achieve 0.8 V/nm if 300 nm SiO_2 and 10 nm HfO_2 respectively have breakdown voltages larger than 120 V and 4 V. Based on Figure 6.4, a lowering of 400 meV is possibly observed. Such studies will open up a new way for TMD materials and potentially motivate new optoelectronic applications in future.

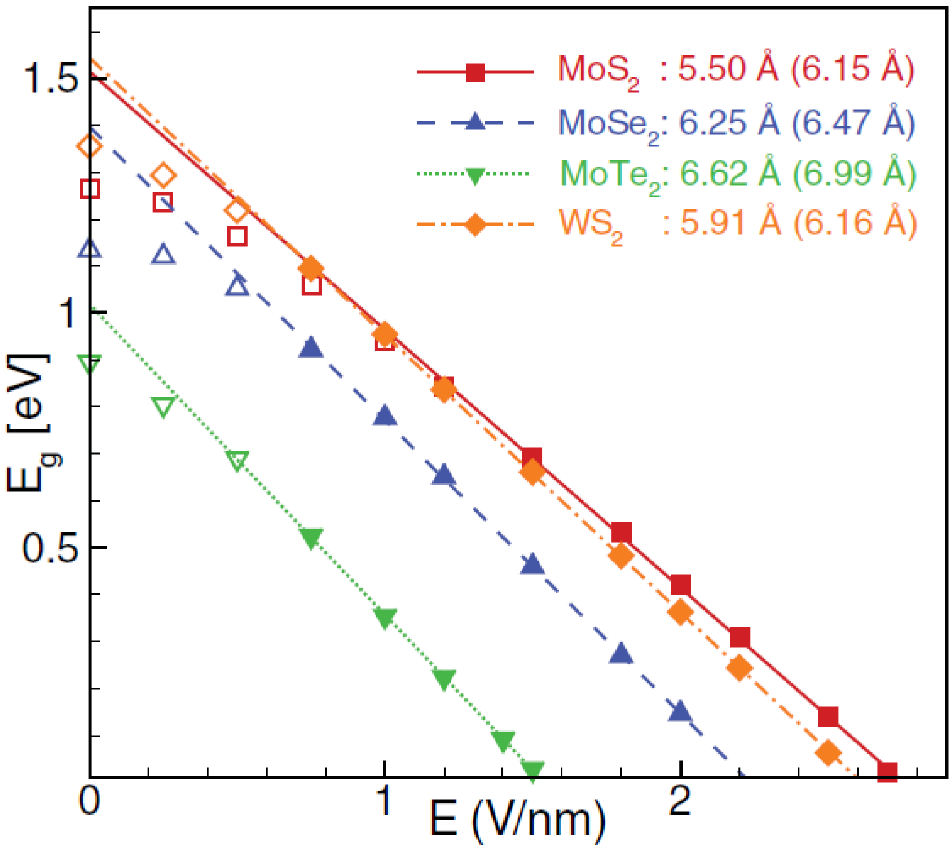

Figure 6.3 Band gap E_g versus electric field for different TMDs including MoS_2, $MoSe_2$, $MoTe_2$, and WS_2. The figure is from Ref. [159].

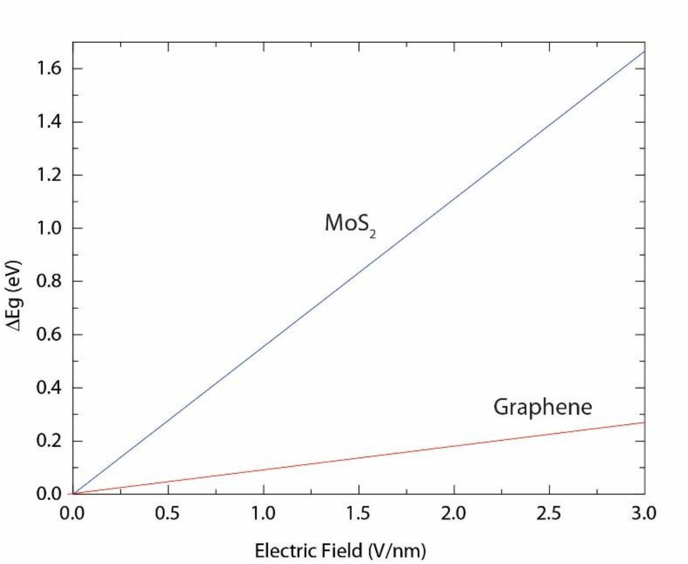

Figure 6.4 The comparison of band gap tunability as a function of electric field for graphene (experiments) [160] and MoS_2 (calculations) [159].

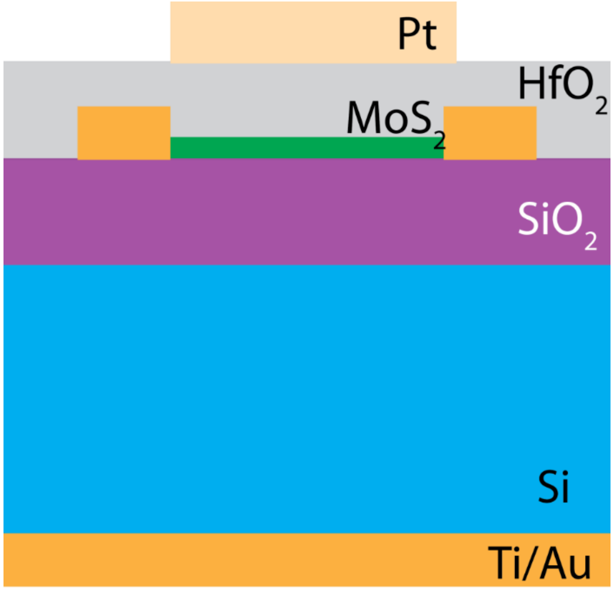

Figure 6.5 Proposed dual-gate bilayer MoS_2 field effect transistor.

APPENDIX A: GRAPHENE TRANSFER STEPS

To fully utilize strength of graphene, it is critical to acquire reliable technique to transfer large-area graphene grown by CVD. In the section we will explain details of our transfer process. The transfer steps are depicted in the following:

1) Start with graphene on Cu and tape it to a dummy Si wafer;
2) PMMA coating on graphene. Spin speed: 500rpm, 60s. Baking at 120 ℃, 10 min.
3) Backside graphene removal by RIE. O_2 25 sccm, power 80 W, pressure 150 mTorr.
4) Cu etching with APS-100 for 3 hours.
5) Modified RCA clean.
    a) RCA2: H2O:H2O2:HCl=30:1:1, for 10 min.
    b) RCA1: H20:H2O2:NH4OH=30:1:1, for 10 min.
6) Move film into water, leave for 2 hours.
7) Fish out the film using target substrate.
8) Dry for 30 min.
9) Bake at 150 ℃ for 15 min.
10) Remove PMMA. Soak film on substrate in ACE for 3 hours, then clean with IPA. Blow to dry using N2 gun.

APPENDIX B: DRY TRANSFER STEPS OF LAYERED MATERIALS

The setup we used to dry-transfer our flakes are shown in the Figure B.1.

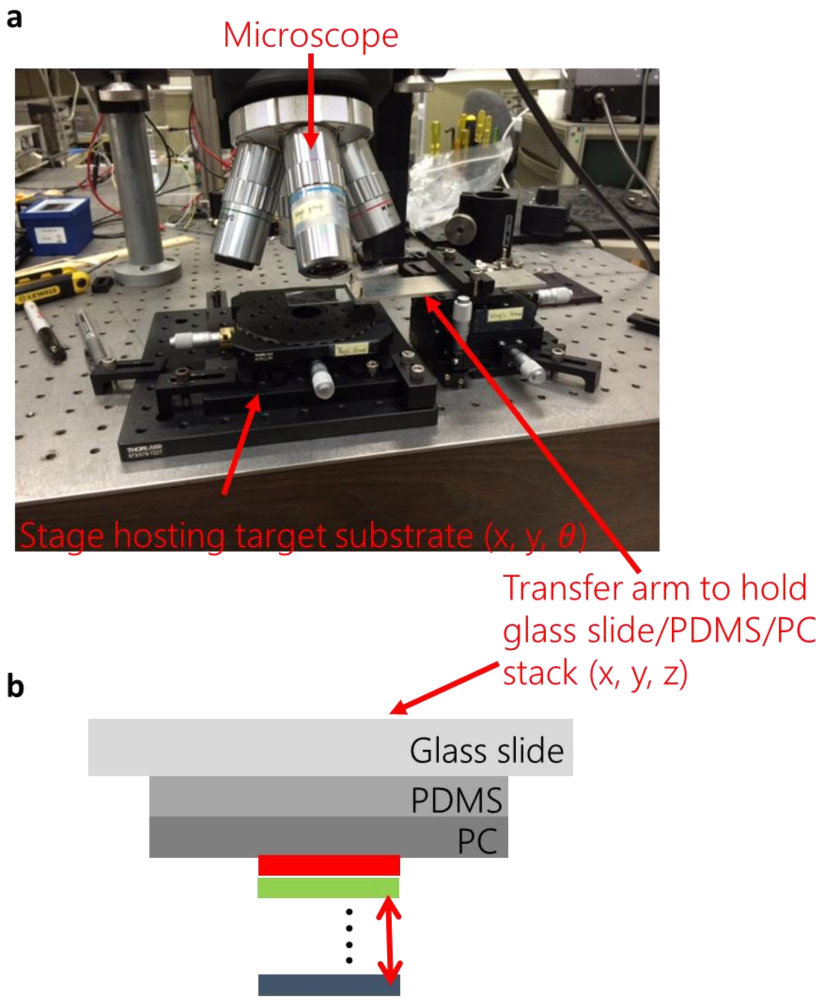

Figure B.1 (a) Optical image of transfer set up. (b) The polymer stacking of transfer arm.

Our fabrications using this setup is described as below:

1) Make polycarbonate (PC, Sigma Aldrich, 6% dissolved in chloroform solvents)

2) Drop-cast or spin PC solutions on a bare glass slide, and leave it dry for 30 min. When it's try, PC will form a thin layer on top of the glass slide.
3) Cut PDMS film (Gel Pak, X4) square on another glass slide, and cut a small piece of PC (larger than PDMS square). Place the PC on top of PDMS as shown in Figure B.1.
4) Use standard scotch tape method to exfoliate layered materials onto a SiO_2/Si wafer.
5) Look for desired flakes on the substrate and 'pick up' the ideal one with PC/PDMS stacking while heating the substrate at 90 ℃.
6) Repeat exfoliation steps on SiO_2/Si substrate and continue picking up using the polymer stacking.
7) Once the desired stack is achieved on PC/PDMS/glass slide, and place the entire stacking on the target substrate. Heat up the stage to 150 ℃, then the stack and PC will stay on the substrate.
8) Place the sample into chloroform for 10 mins to dissolve PC film. Clean with ACE and IPA, then dry with N_2 gun.

APPENDIX C: FABRICATION OF LAYERED MATERIALS BASED TRANSISTORS

Throughout this work, the fabrication of transistors using layered materials are realized by electron-beam lithography (EBL) and evaporation. The detailed steps are described as below:

1) Exfoliation of materials on to substrate with markers (usually markers are made by optical lithography)
2) Take pictures of the sample (with at least two markers in the same view)
3) Draw the EBL mask (using L-Edit or KLayout).
4) Spin MMA (8.5), 4000 rpm, 30s, 170℃, 2 min.
5) Spin PMMA 950 (A4), 4000 rpm, 30s, 170℃, 3 min.
6) EBL: 10 nA. pitch size: 22 nm.
7) Develop: MIBK: IPA = 1:3, 60s.
8) Clean with IPA.
9) Dry with N_2 gun.

APPENDIX D: MODELING OF THIN-FILM FIELD EFFECT TRANSISTORS

Part 1:

Calculate the drain current with saturation as a function of gate and drain voltages.

Assume E_i as reference energy level.

$V_g - V_{th} - V_c(x) = V_q(x) + V_{ox}$ -- D. 1

Here V_{th} is determined by the unintentional doping:

$V_{th} \approx \left(C_{ox}^{-1} + C_{dp}^{-1}\right) q N_D$, which is related to the case that transfer curve shifts to the left. In the following just use V_g to sub $V_g - V_{th}$, later on, sub it back. $V_c(x)$ is the voltage at the position x along the channel. At drain side, $V_c(x = L) = V_d - I_d R_c$, and at source side, $V_c(x = 0) = V_s + I_d R_c$.

In a 2D channel, the carrier concentration n or p could be calculated using 2D density of states ($D_0 = g_s g_v m^* / 2\pi\hbar^2$), so:

$n = \int_{E_0}^{\infty} D_0 f(E) dE = D_0 KT ln\left(1 + \exp\left(\frac{qV_q - E_0}{KT}\right)\right)$ -- D. 2

$p = \int_{-\infty}^{-E_0} D_0 \left(1 - f(E)\right) dE = D_0 KT ln\left(1 + \exp\left(-\frac{qV_q + E_0}{KT}\right)\right)$ -- D. 3

$$C_q = -\frac{dQ}{dV_q} = \frac{q^2 D_0}{1 + \exp\frac{E_0 - qV_q}{KT}} + \frac{q^2 D_0}{1 + \exp\frac{E_0 + qV_q}{KT}}$$

-- D. 4

V_q is channel voltage drop over ‘quantum capacitance’ or we say, the change of Fermi level since E_i. $V_q > 0$ when electrons populate the channel and $V_q < 0$ when holes dominate. The relation between V_q and n (or p) are shown above. They can be used to correlate V_q, V_c and V_g. From Eqs D. 1 – 3 we could get:

$$V_q(x) = (\left|V_g - V_c(x)\right| - V_{ox})sgn(V_g - V_c(x)) \quad \text{-- D. 5}$$

This ensures that, $V_q > 0$ for electrons and $V_q < 0$ for holes. We keep V_{ox} always as positive values.

$$V_{ox} = \frac{q(n(x)+p(x))}{C_{ox}} = \frac{qD_0KT}{C_{ox}} * [ln\left(1 + \exp\left(\frac{qV_q - E_0}{KT}\right)\right) + ln\left(1 + \exp\left(-\frac{qV_q + E_0}{KT}\right)\right)] \quad \text{-- D. 6}$$

Bring Eq D. 6 into D. 5 to iteratively calculate $V_q(x) = f(V_g, V_c(x))$.

Or from simple circuit model as in Fig 1 (b), V_q could be expressed as:

$$V_q(x) = \frac{\left(V_g - V_c(x)\right)}{\left(1 + \frac{C_t}{C_{ox}}\right)} \text{ where } C_t = C_q + C_{it} \quad \text{-- D. 7}$$

Now we could write the current equation along the channel as:

$$I_d = qWn(x)v(x) \quad \text{-- D. 8}$$

The current is constant all along the channel so Eq D. 8 could be further written (if assuming linear relation between μ and velocity) as:

$$I_d = qWn(x)v(x) = \frac{qW\int_0^L n(x)v(x)dx}{\int_0^L dx} = \frac{qW}{L}\int_0^L n(x)\,\mu\,\frac{dV_c(x)}{dx}dx = \frac{qW}{L}\int_{V_{cs}}^{V_{cd}} n(V_c)\,\mu\, dV_c = \frac{qW}{L}\int_{V_{qd}}^{V_{qs}} n\left(V_q\right)\mu\frac{dV_c}{dV_q}dV_q$$

From Eq. D. 7, $\frac{dV_c}{dV_q} = -\left(1 + \frac{C_t}{C_{ox}}\right)$, bring this into above equation, we have:

$$I_d = \frac{qW\mu}{L}\int_{V_{qd}}^{V_{qs}} n\left(V_q\right)\mu(1 + \frac{C_t}{C_{ox}})dV_q$$

where V_{qs} and V_{qd} are the quantum capacitance related voltage drop at source and drain (after removing the contact resistance). The upper and lower limits are determined by Eqs D. 6 and 6, or 7.

Summary of equations:

1) $V_g - V_{th} - V_x = V_{ox} + V_q$

2) $V_{th} \approx \left(\frac{1}{C_{ox}} + \frac{1}{C_{dep}}\right) qN_D$

3) $D_0 = \frac{g_s g_v m^*}{2\pi\hbar^2}$

4) $n = \int_{E_0}^{\infty} D_0 f(E)dE = D_0 KTln\left(1 + \exp\left(\frac{qV_q - E_0}{KT}\right)\right)$

5) $p = \int_{-\infty}^{-E_0} D_0\big(1 - f(E)\big)dE = D_0 KTln\left(1 + \exp\left(-\frac{qV_q + E_0}{KT}\right)\right)$

6) $C_q = -\frac{dQ}{dV_q} = \frac{q^2 D_0}{1+\exp\left(\frac{E_0 - qV_q}{KT}\right)} + \frac{q^2 D_0}{1+\exp\left(\frac{E_0 + qV_q}{KT}\right)}$

7) $C_t = C_q + C_{it}$

8) $V_{ox} = \frac{Q}{C_{ox}} = \frac{q(n+p)}{C_{ox}}$

9) $V_g - V_{th} - V_x = \frac{q(n+p)}{C_{ox}} + V_q$ <== use this to determine V_q at different locations.

10) $\frac{KT}{q}\ln\left(\exp\frac{n_x}{D_0 KT} - 1\right) + \frac{E_0}{q} + \frac{n_x}{C_{ox}} = V_g - V_{th} - V_x$

11) $I_d = qWn_x v_x$

12) $I_d = \frac{qW}{L}\int_0^L n_x \mu \frac{dV_x}{dx} dx$

$$= \frac{qW}{L}\int_{V_{xs}}^{V_{xd}} n(V_c)\mu dV_x$$

$$= \frac{qW}{L} \int_{V_{qd}}^{V_{qs}} n(V_q) \mu \frac{dV_x}{dV_q} dV_q$$

$$= \frac{qW\mu}{L} \int_{V_{qd}}^{V_{qs}} n(V_q)\, (1 + C_t/C_{ox}) dV_q$$

$$\sim \frac{qW\mu}{L} \left\{ \left[D_0 (KT)^2 \exp(\frac{qV_q - E_0}{KT}) \left(1 + \frac{C_{it}}{C_{ox}}\right) \right] + \left[\frac{(qD_0 KT)^2}{2C_{ox}} \ln^2(1 + \exp\left(\frac{qV_q - E_0}{KT}\right)) \right] \right\} \text{ from } V_{qs} \text{ to } V_{qd}$$

APPENDIX E: MODELING ABSORPTION IN THIN FILM STRUCTURE

Let us consider the case of light normal incidence in air with a refractive index n0 = 1 into a three-layer stack consisting of semitransparent electrode (metal or graphene), Al2O3, and Si with a complex and wavelength-dependent refractive index of n1, n2 and n3, respectively.21 The thickness of the metal or graphene, and the oxide are d1 and d2. Also assumed is the Si substrate being semi-infinite and Al2O3 being transparent with a zero imaginary refractive index in the entire optical range. For a single-layer graphene, n1 was measured by spectroscopic ellipsometry22 and the thickness is taken to be 0.34 nm. With the described geometry, it is straightforward to show the reflection by the entire stack is given by:

$$R = |E_0^- / E_0^+|^2 = \left|\frac{r_1 + r_2 \exp(2\delta_1) + r_3 \exp 2(\delta_1 + \delta_2) + r_1 r_2 r_3 \exp(2\delta_2)}{1 + r_1 r_2 \exp(2\delta_1) + r_1 r_3 \exp 2(\delta_1 + \delta_2) + r_2 r_3 \exp(2\delta_2)}\right|^2 \qquad \text{-- E. 1}$$

$$r_1 = \frac{n_0 - n_1}{n_0 + n_1}\ , \quad r_2 = \frac{n_1 - n_2}{n_1 + n_2}\ , \quad r_3 = \frac{n_2 - n_3}{n_2 + n_3} \qquad \text{-- E. 2}$$

and the phase factor δ_i relates to the film thickness as:

$$\delta_1 = -i\left(\frac{2\pi}{\lambda}\right) n_1 d_1\ , \ \ \delta_2 = -i\left(\frac{2\pi}{\lambda}\right) n_2 d_2 \qquad \text{-- E. 3}$$

The power transmission into Si is given by:

$$T = Re(n_3) |E_3^+ / E_0^+|^2$$

$$= Re(n_3) \left|\frac{(1 + r_1)(1 + r_2)(1 + r_3)\exp(\delta_1 + \delta_2)}{1 + r_1 r_2 \exp(2\delta_1) + r_1 r_3 \exp 2(\delta_1 + \delta_2) + r_2 r_3 \exp(2\delta_2)}\right|^2 \qquad \text{-- E. 4}$$

where E_0^+, E_3^+, and E_0^- are the amplitudes of the light waves incident, transmitted into the substrate, and reflected, respectively. Since we have assumed no absorption by

Al_2O_3, the optical absorption (A) by the metal or graphene electrode becomes $A = 1 - T - R$.

APPENDIX F: MODELING OF VDW CAPACITANCE

The goal of this part is to model the carrier concentration, Fermi levels, in vdW heterojunctions as a function of V_g, V_d, and C_V.

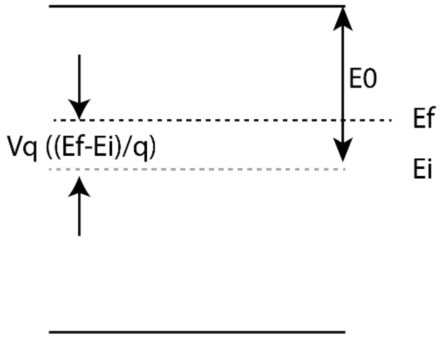

Figure F.2 Fermi level and band alignment

The density of states D_0 in 2D crystals is constant, $D_0 = g_s g_v m^*/2\pi\hbar^2$, so:

$$n = \int_{E_0}^{\infty} D_0 f(E)dE = D_0 KTln\left(1 + \exp\left(\frac{qV_q - E_0}{KT}\right)\right) \qquad \text{– F .1}$$

$$p = \int_{-\infty}^{-E_0} D_0\big(1 - f(E)\big)dE = D_0 KTln\left(1 + \exp\left(-\frac{qV_q + E_0}{KT}\right)\right) \qquad \text{– F.2}$$

$$Q = q\big(p - n + N_{imp}\big) = qD_0 KTln\left(1 + \exp\left(-\frac{qV_q + E_0}{KT}\right)\right) - qD_0 KTln\left(1 + \exp\left(\frac{qV_q - E_0}{KT}\right)\right) + qN_{imp} \qquad \text{– F. 3}$$

Note that $N_{imp} = N(dopor) - N(acceptor)$ It is important that external doping changes the initial carrier concentration of the materials, BUT this part of carrier concentration would be contributed to the initial net charges. This means, Q=0 when no voltages are applied – CHARGE NEUTRALITY inside each material.

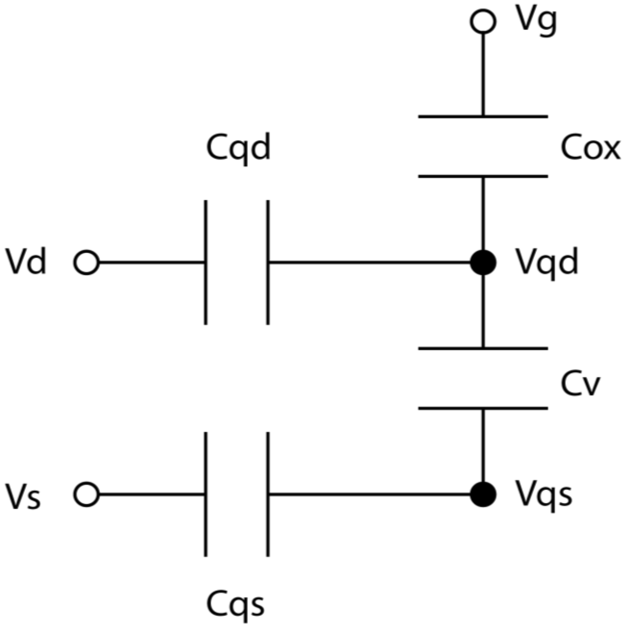

Figure F. 2 Quantum capacitance *vs* vdW capacitance.

$$C_q = -\frac{dQ}{dV_q} = \frac{q^2 D_0}{1 + \exp\frac{E_0 - qV_q}{KT}} + \frac{q^2 D_0}{1 + \exp\frac{E_0 + qV_q}{KT}}$$

-- F. 4

V_q is channel voltage drop over 'quantum capacitance' or we say, the change of Fermi level since E_i. $V_q > 0$ when electrons populate the channel and $V_q < 0$ when holes dominate. The relation between V_q and n (or p) are shown above. They can be used to correlate V_q, and V_g.

$V_{gd} = \Delta V_{qd} + V_{ox}$ -- F. 5

This means that the gate voltage applied externally is divided into two parts, one is part dropped over oxide, $V_{ox} = -q(Q_d + Q_s)/C_{ox}$ (from Gauss's law), ((a) in the figure) and the other is the change of Fermi levels, that is dropped on ‘quantum capacitance’.

When Fermi level is close to E_i, the quantum capacitance is very small (no density of states inside the gap), so the applied gate voltages would largely dropped on quantum capacitance (the small one dominates), $V_{ox} \ll V_q$. This is valid for low carrier concentration region. When Fermi level is close to conduction or valence band, C_q is large, so most of the V_g is over oxide, that is, V_{ox} dominates. To achieve an accurate result, especially in subthreshold region, it is critical to consider both of the voltages.

In cases with vdW gap, the gap can be regarded as a capacitance, C_v. The equations we could write are:

$V_{gd} = V_{gd} = V_{ox} + V_{qd} = -(Q_s + Q_d)/C_{ox} + \Delta V_{qd}$ -- F. 6a

$V_{sd} = \Delta V_{qd} + Q_s/C_v - \Delta V_{qs}$ -- F. 5b

where $\Delta V_{qs} = V_{qs} - V_{qs0}$ and $\Delta V_{qs} = V_{qd} - V_{qd0}$. Q_s/C_v is the term that linked top and bottom layer carrier concentrations.

V_{qd0} and V_{qs0} are respectively determined by impurity doping in either layer. These would be all the equations needed to solve Q, Vq in top and bottom layers.

Part 2

To make the problem more simple and specific, we consider the following cases:

Top layer (drain) is p-doping (p_{d0}), and the bottom (source) is n-doping (n_{s0}). In this case, $V_{qd0} < 0$ and $V_{qs0} > 0$.

$$qV_{qs0} = qKTln\left(\exp\left(\frac{n_{s0}}{D_{s0}KT}\right) - 1\right) + E_{d0}$$

$$qV_{qd0} = -qKTln\left(\exp\left(\frac{p_{do}}{D_{d0}KT}\right) - 1\right) - E_{d0}$$

$$Q_s = q(p_s - n_s + N_s) \approx -qD_0KTln\left(1 + \exp\left(\frac{qV_{qs} - E_0}{KT}\right)\right) + qN_s$$

$$Q_d = q(p_d - n_d - N_d) \approx qD_0KTln\left(1 + \exp\left(-\frac{qV_{qd} + E_0}{KT}\right)\right) - qN_d$$

From Eq. F. 6b, we get:

$V_{qd} = V_s + V_{qd0} - \frac{Q_s(V_{qs})}{C_v} + V_{qs} - V_{qs0}$

Bring this into Eq F. 6a:

$$V_{gd} = -\frac{Q_s(V_{qs}) + Q_d(V_{qd})}{C_{ox}} + V_{qd} - V_{qd0}$$

Substract the V_{qd} with the function of V_{qs} and solve the above equations iteratively, then V_{qs} would be obtained, and so to the rest.

V_{qs} can start from $V_{qs0} \pm n * \Delta$, depending on the sign of applied voltages

V_{qd} can start from $V_{qs0} \pm n * \Delta$, depending on the sign of applied voltages

The change of band offsets between the two would be $qV_v = Q_s/C_v$

REFERENCES

1. Castro Neto, A.H., et al., *The electronic properties of graphene.* Reviews of Modern Physics, 2009. **81**: p. 109-162.
2. Novoselov, K.S., et al., *Electric field effect in atomically thin carbon films.* Science 2004. **306**: p. 666-9.
3. Novoselov, K.S., et al., *Two-dimensional gas of massless Dirac fermions in graphene.* Nature, 2005. **438**: p. 197-200.
4. Geim, A.K. and K.S. Novoselov, *The rise of graphene.* Nature Materials, 2007. **6**: p. 183-191.
5. Bolotin, K.I., et al., *Ultrahigh electron mobility in suspended graphene.* Solid State Communications, 2008. **146**: p. 351-355.
6. Wang, L., et al., *One-dimensional electrical contact to a two-dimensional material.* Science, 2013. **342**: p. 614-7.
7. Nair, R.R., et al., *Fine Structure Constant Defines Visual Transparency of Graphene.* Science, 2008. **320** p. 1308.
8. Stauber, T., N. Peres, and a. Geim, *Optical conductivity of graphene in the visible region of the spectrum.* Physical Review B, 2008. **78**: p. 085432.
9. Wang, Q.H., et al., *Electronics and optoelectronics of two-dimensional transition metal dichalcogenides.* Nature Nanotechnology, 2012. **7**: p. 699-712.
10. Dean, C.R., et al., *Boron nitride substrates for high-quality graphene electronics.* Nat Nano, 2010. **5**(10): p. 722-726.
11. Li, L., et al., *Black phosphorus field-effect transistors.* Nature Nanotechnology, 2014. **9**(5): p. 372-377.
12. Radisavljevic, B., et al., *Single-layer MoS_2 transistors.* Nature Nanotechnology, 2011. **6**: p. 147-150.
13. Mak, K.F., et al., *Atomically Thin MoS_2: A New Direct-Gap Semiconductor.* Phys. Rev. Lett., 2010. **105**: p. 136805.
14. Splendiani, A., et al., *Emerging Photoluminescence in Monolayer MoS2.* Nano Letters, 2010. **10**: p. 1271-1275.
15. Gutierrez, H.R., *Extraordinary room-temperature photoluminescence in WS_2 monolayers.* Nano Letters, 2012: p. nl3026357.
16. Amani, M., et al., *Near-unity photoluminescence quantum yield in MoS_2.* Science, 2015. **350** (6264): p. 1065-1068.
17. Shi, H., et al., *Exciton Dynamics in Suspended 2D Crystals.* ACS Nano, 2013. **7**: p. 1072-1080.
18. Ramasubramaniam, A., *Large excitonic effects in monolayers of molybdenum and tungsten dichalcogenides.* Physical Review B, 2012. **115409**: p. 1-6.
19. Lee, C.-H., et al., *Atomically thin p–n junctions with van der Waals heterointerfaces.* Nature Nanotechnology, 2014. **9**: p. 676-681.
20. Roy, T., et al., *Dual-Gated MoS_2/WSe_2 van der Waals Tunnel Diodes and Transistors.* ACS nano, 2015.

21. Furchi, M.M., et al., *Photovoltaic Effect in an Electrically Tunable van der Waals Heterojunction.* Nano Letters, 2014. **14**: p. 4785-4791.
22. Dean, C.R., et al., *Hofstadter's butterfly and the fractal quantum Hall effect in moire superlattices.* Nature, 2013. **497**(7451): p. 598-602.
23. Hunt, B., et al., *Massive Dirac Fermions and Hofstadter Butterfly in a van der Waals Heterostructure.* Science, 2013. **340**(6139): p. 1427-1430.
24. Dai, S., et al., *Tunable Phonon Polaritons in Atomically Thin van der Waals Crystals of Boron Nitride.* Science, 2014. **343**(6175): p. 1125-1129.
25. Rivera, P., et al., *Observation of long-lived interlayer excitons in monolayer MoSe2–WSe2 heterostructures.* Nature Communications, 2015. **6**: p. 6242.
26. Hong, X., *Ultrafast Charge Transfer in Atomically Thin MoS2/WS2 Heterostructures.* Nature Nanotechnology, 2014.
27. Britnell, L., et al., *Strong light-matter interactions in heterostructures of atomically thin films.* Science, 2013. **340**: p. 1311-4.
28. Withers, F., et al., *Light-emitting diodes by band-structure engineering in van der Waals heterostructures.* Nature Materials, 2015. **14**: p. 301-306.
29. Sensale-Rodriguez, B., et al., *Broadband graphene terahertz modulators enabled by intraband transitions.* Nature Communications, 2012. **3**: p. 780.
30. Yan, R., et al., *A new class of electrically tunable metamaterial terahertz modulators.* Optics express, 2012. **20**: p. 28664-71.
31. Yan, R., et al., *Exceptional Terahertz Wave Modulation in Graphene Enhanced by Frequency Selective Surfaces.* ACS Photonics, 2016. **3**(3): p. 315-323.
32. Yan, R., et al., *Raman and Photoluminescence Study of Dielectric and Thermal Effects on Atomically Thin* MoS_2. arXiv:1211.4136
33. Yan, R., et al., *Esaki Diodes in van der Waals Heterojunctions with Broken-Gap Energy Band Alignment.* Nano Letters, 2015: **15** p. 5791-5798.
34. Nguyen, N.V., O.A. Kirillov, and J.S. Suehle, *Band alignment of metal-oxide-semiconductor structure by internal photoemission spectroscopy and spectroscopic ellipsometry.* Thin Solid Films, 2011. **519**: p. 2811-2816.
35. Afanas' ev, V.V., *Internal Photoemission Spectroscopy: Principles and Applications.* 2010.
36. Adamchuk, V.K. and V.V. Afanas'ev, *Internal photoemission spectroscopy of semiconductor-insulator interfaces.* Progress in Surface Science, 1992. **41**: p. 111-211.
37. Sze, S.M. and K.K. Ng, *Physics of semiconductor devices.* 2006.
38. Yan, R., et al., *Determination of graphene work function and graphene-insulator-semiconductor band alignment by internal photoemission spectroscopy.* Applied Physics Letters, 2012. **101**: p. 022105.
39. Ferrari, A.C., et al., *Raman Spectrum of Graphene and Graphene Layers.* Phys. Rev. Lett., 2006. **97**: p. 187401.
40. Blake, P., et al., *Making graphene visible.* Applied Physics Letters, 2007. **91**: p. 063124.
41. Nguyen, N.V., et al., *Optical band gaps and composition dependence of hafnium–aluminate thin films grown by atomic layer chemical vapor deposition.* Journal of Vacuum Science & Technology A, 2005. **23**.

42. Das A, et al., *Monitoring dopants by Raman scattering in an electrochemically top-gated graphene transistor.* Nature Nanotechnology, 2008. **3**(4): p. 210-215.
43. Williams, R., *Photoemission of Electrons from Silicon into Silicon Dioxide.* Physical Review, 1965. **140**: p. A569-A575.
44. Filleter, T., et al., *Local work function measurements of epitaxial graphene.* Applied Physics Letters, 2008. **93**: p. 133117.
45. Yu, Y.-J., et al., *Tuning the Graphene Work Function by Electric Field Effect.* Nano Letters, 2009. **9**: p. 3430-3434.
46. Afanas'ev, V.V. and A. Stesmans, *Internal photoemission at interfaces of high-κ insulators with semiconductors and metals.* Journal of Applied Physics, 2007. **102**: p. 081301.
47. Ramaiah, K.S., et al., *Optical, structural and electrical properties of tin doped indium oxide thin films prepared by spray-pyrolysis technique.* Semiconductor science and technology, 2000. **15**(7): p. 676.
48. Goodman, A.M., *Photoemission of Holes from Silicon into Silicon Dioxide.* Physical Review, 1966. **152**: p. 780-784.
49. Nelson, F., et al., *Spectroscopic Ellipsometry of CVD Graphene.* ECS Transactions, 2011. **35** p. 173-183.
50. Xu, K., et al., *Direct measurement of Dirac point energy at the graphene/oxide interface.* Nano letters, 2013. **13**: p. 131-6.
51. Tonouchi, M., *Cutting-edge terahertz technology.* Nature Photonics, 2002: p. 97-105.
52. Siegel, Peter H., *Terahertz technology*, IEEE Transactions on microwave theory and techniques 2002, **50** (3): p. 910-928.
53. Rahm, M., J.-S. Li, and W. Padilla, *THz Wave Modulators: A Brief Review on Different Modulation Techniques.* Journal of Infrared, Millimeter, and Terahertz Waves, 2013. **34**: p. 1-27.
54. Kleine-Ostmann, T., et al., *Room-temperature operation of an electrically driven terahertz modulator.* Applied Physics Letters, 2004. **84**: p. 3555-3557.
55. Chen, H.-T., et al., *Active terahertz metamaterial devices.* Nature, 2006. **444**: p. 597-600.
56. Chen, H.-T., et al., *A metamaterial solid-state terahertz phase modulator.* Nature Photonics, 2009. **3**: p. 148-151.
57. Paul, O., et al., *Polarization-independent active metamaterial for high-frequency terahertz modulation.* Optics express, 2009. **17**(2): p. 819-827.
58. Chen, H.-T., et al., *Electronic control of extraordinary terahertz transmission through subwavelength metal hole arrays.* arXiv preprint arXiv:0804.2942, 2008.
59. Padilla, W.J., et al., *Dynamical Electric and Magnetic Metamaterial Response at Terahertz Frequencies.* Physical Review Letters, 2006. **96**: p. 107401.
60. Lee, S.H., et al., *Ultrafast refractive index control of a terahertz graphene metamaterial.* Sci. Rep., 2013. **3**.
61. Berry, C.W., J. Moore, and M. Jarrahi, *Design of reconfigurable metallic slits for terahertz beam modulation.* Opt. Express, 2011. **19**: p. 1236-1245.

62. Unlu, M., et al., *Broadband Terahertz Modulators based on MEMS-Reconfigurable Mesh Filters.* arXiv, 2012: p. 1212.6562.
63. Bonaccorso, F., et al., *Graphene photonics and optoelectronics.* Nature Photonics, 2010. **4**: p. 611-622.
64. Stauber, T., N. Peres, and A. Geim, *Optical conductivity of graphene in the visible region of the spectrum.* Physical Review B, 2008. **78**(8): p. 085432.
65. Falkovsky, L.a., *Optical properties of graphene.* Journal of Physics: Conference Series, 2008. **129**: p. 012004.
66. Dawlaty, J.M., et al., *Measurement of the optical absorption spectra of epitaxial graphene from terahertz to visible.* Applied Physics Letters, 2008. **93**: p. 131905.
67. Falkovsky, L. and S. Pershoguba, *Optical far-infrared properties of a graphene monolayer and multilayer.* Physical Review B, 2007. **76**: p. 153410.
68. Mak, K.F., et al., *Optical spectroscopy of graphene: From the far infrared to the ultraviolet.* Solid State Communications, 2012. **152**: p. 1341-1349.
69. Nomura, K. and a.H. MacDonald, *Quantum Transport of Massless Dirac Fermions.* Physical Review Letters, 2007. **98**: p. 076602.
70. Hwang, E., S. Adam, and S. Sarma, *Carrier Transport in Two-Dimensional Graphene Layers.* Physical Review Letters, 2007. **98**: p. 186806.
71. Horng, J., et al., *Drude conductivity of Dirac fermions in graphene.* Physical Review B, 2011. **83**: p. 165113.
72. Maeng, I., et al., *Gate-Controlled Nonlinear Conductivity of Dirac Fermion in Graphene Field-Effect Transistors Measured by Terahertz Time- Domain Spectroscopy.* Nano Letters, 2012. **12** (2):p. 551-555.
73. Weis, P., et al., *Spectrally wide-band terahertz wave modulator based on optically tuned graphene.* ACS nano, 2012. **6**: p. 9118-24.
74. Kasry, A., et al., *Chemical doping of large-area stacked graphene films for use as transparent, conducting electrodes.* ACS nano, 2010. **4**: p. 3839-44.
75. Bae, S., et al., *Roll-to-roll production of 30-inch graphene films for transparent electrodes.* Nature Nanotechnology, 2010. **5**: p. 574-8.
76. Sensale-Rodriguez, B., et al., *Unique prospects for graphene-based terahertz modulators.* Applied Physics Letters, 2011. **99**: p. 113104.
77. Liu, L., et al., *A Broadband Quasi-Optical Terahertz Detector Utilizing a Zero Bias Schottky Diode.* 2010. **20**: p. 504-506.
78. Sensale-Rodriguez, B., et al., *Extraordinary control of terahertz beam reflectance in graphene electro-absorption modulators.* Nano letters, 2012. **12**: p. 4518-22.
79. Chen, H.-T., et al., *Experimental demonstration of frequency-agile terahertz metamaterials.* Nature Photonics, 2008. **2**: p. 295-298.
80. Kim, Y.S., et al., *A tunable terahertz filter and its switching properties in terahertz region based on a defect mode of a metallic photonic crystal.* Journal of Applied Physics, 2011. **109**: p. 123111-123114.
81. Kleine-Ostmann, T., et al., *Spatially resolved measurements of depletion properties of large gate two-dimensional electron gas semiconductor terahertz modulators.* Journal of Applied Physics, 2009. **105**: p. 93706-93707.

82. Ju, L., et al., *Graphene plasmonics for tunable terahertz metamaterials.* Nature Nanotechnology, 2011. **6**: p. 630-4.
83. Porterfield, D.W., et al., *Resonant metal-mesh bandpass filters for the far infrared.* Applied Optics, 1994. **33**: p. 6046-52.
84. Details, P., A.A. Promoter, and A.P. Precursor, *PI-2600 Series – Low Stress Applications.* 2009: p. 1-4.
85. Sensale-Rodriguez, B., et al., *Graphene for Reconfigurable Terahertz Optoelectronics.* Proceedings of the IEEE, 2013. **101**: p. 1705-1716.
86. Shin, D.-W., et al., *A role of HNO_3 on transparent conducting film with single-walled carbon nanotubes.* Nanotechnology, 2009. **20**: p. 475703.
87. Valmorra, F., et al., *Low-Bias Active Control of Terahertz Waves by Coupling Large-Area CVD Graphene to a Terahertz Metamaterial.* Nano Letters, 2013. **13**: p. 3193-3198.
88. Degl'innocenti, R., et al., *Low-Bias Terahertz Amplitude Modulator Based on Split-Ring Resonators and Graphene.* ACS Nano. 2014. **8** (3): p. 2548-2554.
89. Gao, W., et al., *High-Contrast Terahertz Wave Modulation by Gated Graphene Enhanced by Extraordinary Transmission through Ring Apertures.* Nano letters, 2014.
90. Lee, S.H., et al., *Broadband Modulation of Terahertz Waves With Non-resonant Graphene Meta-devices.* IEEE Transactions on microwave theory and techniques, 2013. **3**: p. 764-771.
91. Lee, C., et al., *Anomalous Lattice Vibrations of Single- and Few-Layer MoS2.* ACS Nano, 2010. **4**: p. 2695-2700.
92. Chang, C.-s., et al., *Growth of Large-Area and Highly Crystalline MoS_2 Thin Layers on Insulating Substrates.* Nano letters. 2012. **12** (3): p. 1538-1544.
93. Li, H., *From Bulk to Monolayer MoS_2: Evolution of Raman Scattering.* Advanced Functional Materials, 2012. **22**: p. 1385-1390.
94. Lee, Y.-H., et al., *Synthesis of large-area MoS2 atomic layers with chemical vapor deposition.* Advanced materials (Deerfield Beach, Fla.), 2012. **24**: p. 2320-5.
95. Gupta, A., et al., *Raman scattering from high-frequency phonons in supported n-graphene layer films.* Nano Letters, 2006. **6**: p. 2667-2673.
96. Yoon, D., *Variations in the Raman Spectrum as a Function of the Number of Graphene Layers.* Journal of the Korean Physical Society, 2009. **55**: p. 1299-1303.
97. Molina-Sanchez, A. and L. Wirtz, *Phonons in single-layer and few-layer MoS2 and WS2.* Physical Review B, 2011. **84**: p. 155413.
98. Berkdemir, A., et al., *Identification of individual and few layers of WS2 using Raman spectroscopy.* Scientific reports, 2013. **3**: p. 1755.
99. Yan, R., et al., *Raman and Photoluminescence Study of Dielectric and Thermal Effects on Atomically Thin MoS_2.* arXiv preprint arXiv:1211.4136, 2012.
100. Balandin, A.A., et al., *Superior thermal conductivity of single-layer graphene.* Nano Lett., 2008. **8**: p. 902-907.
101. Balandin, A.a., *Thermal properties of graphene and nanostructured carbon materials.* Nature materials, 2011. **10**: p. 569-81.

102. Cai, W., et al., *Thermal Transport in Suspended and Supported Monolayer Graphene Grown by Chemical Vapor Deposition.* Nano Letters, 2010. **10**: p. 1645-1651.
103. Chen, S., et al., *Raman Measurements of Thermal Transport in Suspended Monolayer Graphene of Variable Sizes in Vacuum and Gaseous Environments.* ACS Nano, 2011. **5**: p. 321-328.
104. Ferraro, J.R., *Introductory Raman Spectroscopy.* 2002.
105. Ferrari, A.C. and D.M. Basko, *Raman spectroscopy as a versatile tool for studying the properties of graphene.* Nature nanotechnology, 2013. **8**: p. 235-46.
106. Berkdemir, A., et al., *Identification of individual and few layers of WS2 using Raman Spectroscopy.* Sci. Rep., 2013. **3**: p. 1755.
107. Cowley, R.A., *The lattice dynamics of an anharmonic crystal.* Adv. Phys., 1963. **12**: p. 421-480.
108. Postmus, C., J.R. Ferraro, and S.S. Mitra, *Pressure dependence of infrared eigenfrequencies of KCl and KBr.* Phys. Rev., 1968. **174**: p. 983-987.
109. Freeman, D.E. and I. Introduction, *Temperature Dependent Raman Intensity.* JAP, 1962.
110. Hart, T.R., R.L. Aggarwal, and B. Lax, *Temperature dependence of Raman scattering in silicon.* Phys. Rev. B, 1970. **1**: p. 638-642.
111. Calizo, I., et al., *Variable temperature Raman microscopy as a nanometrology tool for graphene layers and graphene-based devices.* Appl. Phys. Lett., 2007. **91**: p. 71913.
112. Beechem, T., et al., *Invited Article: Simultaneous mapping of temperature and stress in microdevices using micro-Raman spectroscopy.* The Review of scientific instruments, 2007. **78**: p. 061301.
113. Liu, M.S., et al., *Temperature dependence of Raman scattering in single crystal GaN films.* Applied Physics Letters, 1999. **74**: p. 3125.
114. Wang, Y., et al., *Raman Spectroscopy Study of Lattice Vibration and Crystallographic Orientation of Monolayer MoS2 under Uniaxial Strain.* Small, 2013.
115. Najmaei, S., et al., *Thermal effects on the characteristic Raman spectrum of molybdenum disulfide (MoS_2) of varying thicknesses.* Appl. Phys. Lett., 2012. **100**: p. 13106.
116. Luo, T., et al., *Gallium arsenide thermal conductivity and optical phonon relaxation times from first-principles calculations.* Europhysics Letters, 2013. **101**: p. 16001.
117. Lee, J.-U., et al., *Thermal conductivity of suspended pristine graphene measured by Raman spectroscopy.* Physical Review B, 2011. **83**: p. 81419.
118. Luo, T. and G. Chen, *Nanoscale heat transfer - from computation to experiment.* Phys. Chem. Chem. Phys., 2013. **15**: p. 3389-3412.
119. Sahoo, S., et al., *Temperature-Dependent Raman Studies and Thermal Conductivity of Few-Layer MoS2.* J. Phys. Chem. C, 2013. **117**: p. 9042-9047.

120. Cheng. R. et al., *Electroluminescence and photocurrent generation from atomically sharp WSe_2/MoS_2 heterojunction p–n diodes.* Nano letters. 2014. **14** (10):p. 5590-5597.
121. Geim, A.K. and I.V. Grigorieva, *Van der Waals heterostructures.* Nature, 2013. **499**(7459): p. 419-25.
122. Roy, T., et al., *Dual-Gated MoS_2/WSe_2 van der Waals Tunnel Diodes and Transistors.* ACS Nano, 2015. **9**(2): p. 2071-2079.
123. Furchi, M.M., et al., *Photovoltaic effect in an electrically tunable van der Waals heterojunction.* Nano Lett, 2014. **14**(8): p. 4785-91.
124. Kim, K., et al., *van der Waals Heterostructures with High Accuracy Rotational Alignment.* Nano Lett, 2016. **16**(3): p. 1989-95.
125. Zhou, G., et al., *InGaAs/InP Tunnel FETs With a Subthreshold Swing of 93 mV/dec and I_{ON}/I_{OFF} Ratio Near 10^6* IEEE Electron Device Letters, 2012. **33**(6): p. 782-784.
126. Seabaugh, A.C. and Q. Zhang, *Low-Voltage Tunnel Transistors for Beyond CMOS Logic.* Proceedings of the IEEE, 2010. **98**(12): p. 2095-2110.
127. Feenstra, R.M., D. Jena, and G. Gu, *Single-particle tunneling in doped graphene-insulator-graphene junctions.* Journal of Applied Physics, 2012. **111**(4): p. 043711.
128. Li, M.O., et al., *Single particle transport in two-dimensional heterojunction interlayer tunneling field effect transistor.* Journal of Applied Physics, 2014. **115**(7): p. 074508.
129. Li, M.O., et al., *Two-dimensional heterojunction interlayer tunneling field effect transistors (thin-tfets).* IEEE Journal of the Electron Devices Society, 2015. **3**(3): p. 200-207.
130. Britnell, L., et al., *Resonant tunnelling and negative differential conductance in graphene transistors.* Nature Communications, 2013. **4**: p. 1794.
131. Lin, Y.C., et al., *Atomically thin resonant tunnel diodes built from synthetic van der Waals heterostructures.* Nature Communications, 2015. **6**: p. 7311.
132. Sarkar, D., et al., *A subthermionic tunnel field-effect transistor with an atomically thin channel.* Nature, 2015. **526**(7571): p. 91-95.
133. Giaever, I., *Electron tunneling and superconductivity.* Reviews of Modern Physics, 1974. **46**: p. 245-250.
134. Bardeen, J., L.N. Cooper, and J.R. Schrieffer, *Theory of superconductivity.* Physical Review, 1957. **108**: p. 1175-1204.
135. Devoret, V.B.a.D.V.a.P.J.a.D.E.a.M.H., *Quantum coherence with a single Cooper pair.* Physica Scripta, 1998. **1998**: p. 165.
136. Sirtori, C., et al., *Resonant tunneling in quantum cascade lasers,* in *Quantum Electronics, IEEE Journal of.* 1998. p. 1722-1729.
137. Chen, C.J., *Theory of scanning tunneling spectroscopy.* Journal of Vacuum Science & Technology A, 1988. **6**.
138. Deng, Y., et al., *Black Phosphorus?MonolayerMoS2 van der Waals Heterojunction p?n Diode.* ACS Nano, 2014. **8**: p. 8292-8299.

139. Williams, R.H., et al., *Band structure and photoemission studies of* SnS_2 *and SnSe2. I. Experimental.* Journal of Physics C: Solid State Physics, 1973. **6**: p. 3631.
140. Castellanos-Gomez, A., et al., *Isolation and characterization of few-layer black phosphorus.* 2D Materials, 2014. **1**: p. 025001.
141. Su, Y., et al., $SnSe_2$ *field-effect transistors with high drive current.* Applied Physics Letters, 2013. **103**: p. 263104.
142. Li, L., et al., *Black phosphorus field-effect transistors.* Nature nanotechnology, 2014. **9**: p. 372-7.
143. Jamieson, J.C., *Crystal structures adopted by black phosphorus at high pressures.* Science, 1963. **139**: p. 1291-1292.
144. Robertson, J., *Electronic structure of* SnS_2*,* $SnSe_2$*,* CdI_2 *and* PbI_2*.* Journal of Physics C: Solid State Physics, 1979. **12**: p. 4753.
145. Kane, E.O., *Theory of tunneling.* Journal of Applied Physics, 1961. **32**: p. 83-91.
146. Britnell, L., et al., *Resonant tunnelling and negative differential conductance in graphene transistors.* Nature communications, 2013. **4**: p. 1794.
147. Esaki, L., *New Phenomenon in Narrow Germanium p-n Junctions.* Physical Review, 1958. **109**: p. 603-604.
148. Esaki, L., *Long journey into tunnelling.* Reviews of Modern Physics, 1974. **46**: p. 237-244.
149. Maekawa, T., et al., *Oscillation up to 1.92 THz in resonant tunneling diode by reduced conduction loss.* Applied Physics Express, 2016. **9**(2): p. 024101.
150. Wang, H., et al., *Integrated circuits based on bilayer MoS(2) transistors.* Nano Lett, 2012. **12**(9): p. 4674-80.
151. Chen, C., et al., *Graphene mechanical oscillators with tunable frequency.* Nat Nanotechnol, 2013. **8**(12): p. 923-7.
152. Klauk, H., et al., *Pentacene organic transistors and ring oscillators on glass and on flexible polymeric substrates.* Applied Physics Letters, 2003. **82**(23): p. 4175-4177.
153. Huebler, A.C., et al., *Ring oscillator fabricated completely by means of mass-printing technologies.* Organic Electronics, 2007. **8**(5): p. 480-486.
154. Kim, D.-H., et al., *Complementary Logic Gates and Ring Oscillators on Plastic Substrates by Use of Printed Ribbons of Single-Crystalline Silicon.* IEEE Electron Device Letters, 2008. **29**(1): p. 73-76.
155. Kim, Y.H., et al., *Flexible metal-oxide devices made by room-temperature photochemical activation of sol-gel films.* Nature, 2012. **489**(7414): p. 128-32.
156. Afsar, Y., et al., *Impact of bending on flexible metal oxide TFTs and oscillator circuits.* Journal of the Society for Information Display, 2016. **24**(6): p. 371-380.
157. Josephson, B.D., *The discovery of tunnelling supercurrents.* Reviews of Modern Physics, 1974. **46**(2): p. 251-254.
158. Foner, S. and E.J. McNiff, *Upper critical fields of layered superconducting* $NbSe_2$ *at low temperature.* Physics Letters A, 1973. **45**(6): p. 429-430.
159. Ramasubramaniam, A., D. Naveh, and E. Towe, *Tunable band gaps in bilayer transition-metal dichalcogenides.* Physical Review B, 2011. **84**: p. 205325.

160. Zhang, Y., et al., *Direct observation of a widely tunable bandgap in bilayer graphene*. Nature, 2009. **459**: p. 820-823.